Magnetooptical Materials and Device Architectures for Ultrafast Light Modulation

by

Soheila Kharratian

A Dissertation Submitted to the
Graduate School of Sciences and Engineering
in Partial Fulfillment of the Requirements for
the Degree of

Doctor of Philosophy

in

Materials Science and Engineering

KOÇ ÜNİVERSİTESİ

December 2020

Magnetooptical Materials and Device Architectures for Ultrafast Light Modulation

Koç University

Graduate School of Sciences and Engineering

This is to certify that I have examined this copy of a doctoral dissertation by

Soheila Kharratian

and have found that it is complete and satisfactory in all respects,
and that any and all revisions required by the final
examining committee have been made.

Committee Members:

_____

Prof. Hakan Ürey

_____

Asst. Prof. Mehmet Cengiz Onbaşlı

_____

Asst. Prof. Muhammed Fatih Toy

_____

Prof. Ahmet Oral

_____

Asst. Prof. Emir Salih Mağden

Date: 23.12.2020

To my parents

ABSTRACT

Magnetooptical Materials and Device Architectures for Ultrafast Light Modulation

Doctor of Philosophy in Materials Science and Engineering

December 23, 2020

Magnetooptical (MO) Faraday and Kerr effects lead to rotation of the polarization plane of light in interaction with a magnetized matter. In combination with the intrinsic high speed of magnetization reversal which can go down to femtosecond time scales, MO effects enable magnetooptical spatial light modulators (MOSLMs), promising for nonvolatile, ultrafast, and high-resolution spatial modulation of light. The recent developments in low-power magnetization switching bring about major breakthroughs in MOSLMs benefiting beyond state-of-the-art holography, heads-up displays, virtual and augmented reality systems, data storage, optical communications, solid-state light detection and ranging (LIDAR), and emerging optical devices. The inherent weakness of the MO effects and difficulty in producing high-quality MO materials are the main obstacles on the way of the practicality and industrial development of the MOSLMs. This thesis addresses the challenges associated with MOSLMs and introduces novel solutions for realizing practical MO devices. The advancement of MOSLMs in different aspects including materials engineering, driving system, and device architecture is reviewed in the thesis to locate the present state in this research field. The MO figure of merit for various MO materials reported in the literature is calculated and compared using finite-difference time-domain (FDTD) simulations, suggesting bismuth-substituted yttrium iron garnets (Bi:YIG) with $Bi_1Y_2Fe_5O_{12}$ composition as the superior MO component for MOSLMs. Growth of Bi:YIG thin films on different substrates, by pulsed laser deposition using different growth parameters, is studied in order to optimize the growth conditions. The structural and optical characterization of the Bi:YIG films reveal the accomplishment of epitaxial growth on the garnet substrates and growth of poly-crystalline single-phase films on quartz substrates. In addition to the study of the materials prospect, photonic devices for the enhancement of MO effects are designed. Various magnetophotonic crystal (MPC) structures are investigated for high-contrast

MOSLMs. By optimization of the MPC configuration and layer thicknesses, a three-defect MPC is demonstrated capable of simultaneous enhancement of Faraday rotation at three fundamental wavelengths of red, green, and blue (RGB) within a pixel. Rotation values of 20-55° are achieved in an overall thickness smaller than 1.5 μm including submicron garnet layers, whereas the optical loss is retained below 20 dB. The resonant approaches for enhancing the MO effects generally result in a narrow operation band and limit the applications. In this study, a magnetoplasmonic metasurface is designed for the broadband enhancement of the Faraday effect. While Faraday rotation in a bare Bi:YIG film is below 0.02° in the studied range of 600-1600 nm, the proposed metasurface yields few degrees of rotation in a broad spectral range, with a maximum exceeding 6.5°. It is shown that the MO response of the metasurface and the operation band can be further improved by optimizing the geometry and excitation parameters, leading to rotation values higher than 20° for a total thickness of 15 nm. Finally, the guidelines for designing a desired magnetoplasmonic metasurface are presented and the application of plasmonic metasurfaces in sensing systems is discussed. Different metasurface designs are modeled, fabricated, and tested for surface-enhanced Raman spectroscopy (SERS) and enhancement of the Raman signal by over three orders of magnitude is experimentally demonstrated.

ÖZET

Ultra Hızlı Işık Modülasyonu için Manyetooptik Malzemeler ve Cihaz Mimarileri

Soheila Kharratian

Malzeme Bilimi ve Mühendisliği, Doktora

23 Aralık 2020

Manyetooptik (MO) Faraday ve Kerr etkileri, ışığın manyetize bir madde ile etkileşimi halinde polarizasyon düzleminin dönmesine yol açar. Doğası gereği femtosaniye zaman ölçeklerine inebilen, yüksek hızlı mıknatıslanma ters çevrilme özelliği sayesindeMO etkileri manyetooptik uzaysal ışık modülatörlerinin (MOSLM)ışığın kalıcı, ultra hızlı ve yüksek çözünürlüklü uzaysal modülasyonunu mümkün kılar. Düşük güçlü mıknatıslanma anahtarlaması alanındaki son gelişmeler, MOSLM'lerde büyük atılımlar yapılmasını sağlamış olup, en son teknoloji ötesine geçen holografi, baş üstü ekranları, sanal ve artırılmış gerçeklik sistemleri, veri depolama, optik iletişim, LIDAR, ve yeni çıkan optik cihazların geliştirilmesinde önemli rol oynamaktadır. MO etkilerinin zayıf olması ve yüksek kaliteli MO malzeme üretimindeki zorluklar, MOSLM'lerin pratikliği ve endüstriyel gelişiminin önündeki ana engellerdir. Bu tezde MOSLM'ler ile ilgili zorluklar ele alınmış olup, pratik MO cihazlarını gerçekleştirmek için yeni çözümler sunulmuştur. MOSLM'lerin malzeme mühendisliği, çalışma sistemi ve cihaz mimarisi gibi farklı yönlerden ilerlemesi, bu araştırma alanındaki mevcut durumu belirlemek için tezde üzerinden geçirilmiştir. Literatürde bildirilen çeşitli MO malzemeleri için MO başarım ölçüsü, zamanda sonlu farklar yöntemi (FDTD) simülasyonları kullanılarak hesaplanır ve karşılaştırılır. Buna göre $Bi_1Y_2Fe_5O_{12}$ kompozisyonlu bizmut katkılı itriyum demir garnetleri (Bi:YIG), MOSLM'ler için üstün MO bileşeni olarak önerilmektedir. Bi:YIG ince filmlerinin farklı substratlar üzerinde, farklı büyüme parametreleri kullanılarak darbeli lazer biriktirme ile büyümesi, büyüme koşullarını optimize etmek için incelenmiştir. Bi:YIG filmlerinin yapısal ve optik karakterizasyonu, garnet substratlar üzerinde epitaksiyel büyümenin ve kuvars substratlar üzerinde poli-kristalin tek fazlı filmlerin büyümesinin başarısını ortaya koymaktadır. Malzeme araştırmalarına ek olarak, MO etkilerinin güçlendirilmesi için fotonik cihazlar tasarlanmıştır. Yüksek kontrastlı MOSLM'ler için çeşitli manyetofotonik kristal (MPC) yapıları

araştırılmıştır. MPC konfigürasyonunun ve katman kalınlıklarının optimizasyonu ile, bir piksel içinde eşzamanlı olarak kırmızı, yeşil ve mavi (RGB) üç temel dalga boyunda Faraday rotasyonunu artırabilen üç kusurlu bir MPC gösterilmiştir. 20-55° dönme değerleri, 1,5 μm'den küçük bir toplam kalınlıkta, mikron altı garnet katmanları dahil olmak üzere elde edilirken, optik kayıp 20 dB'nin altında kaldığı gösterilmiştir. MO etkilerinin artırılmasına yönelik rezonans yaklaşımları, genellikle dar bir operasyon bandı ile sonuçlanır ve uygulamaları sınırlar. Bu çalışmada, Faraday etkisinin genişbant artırılması için bir manyetoplazmonik metayüzey tasarlanmıştır. Çalışılmış olan 600-1600 nm'lik dalgaboyu aralığında saf Bi:YIG filminde Faraday rotasyonu 0.02°'nin altında iken, önerilen metayüzeyde, geniş bir spektral aralıkta, maksimumu 6.5°'yi aşan, birkaç derece rotasyon elde edilebildiği gösterilmiştir. Geometri ve uyarma parametrelerini optimize ederek, bu metayüzeyin MO işlevi ve operasyon bandının daha da geliştirilebileceği ve toplam 15 nm kalınlık içinde 20º'den daha yüksek rotasyon elde edilebildiği gösterilmiştir. Son olarak, manyetoplazmonik metayüzey tasarımı için bir kılavuz sunulmuş olup, plazmonik metayüzeylerin algılama sistemlerinde uygulanması konuları incelenmiştir. Farklı metayüzey tasarımları modellenmiş, imal edilmiş ve yüzeyde güçlendirilmiş Raman spektroskopisi (SERS) ile test edilip, Raman sinyalinin bin kattan fazla iyileştirilmesi deneysel olarak gösterilmiştir.

AKNOWLEDGMENT

I would like to express my deepest gratitude to my PhD advisors Prof. Hakan Ürey and Dr. Mehmet Cengiz Onbaşlı for their infinite support, guidance, encouragement and patience throughout my PhD studies. The opportunity of working with them gave me the chance to learn from their great knowledge and experience.

I would also like to thank to my thesis defense committee members, Dr. Muhammed Fatih Toy, Prof. Ahmet Oral, and Dr. Emir Salih Mağden, for their valuable time and comments which help me improve this Thesis.

I wish to express my special thanks to Dr. Adil Mustafa for the limitless support and help during my PhD studies. I also appreciate the help from Dr. Kivanç Hedili and my colleagues at the Optical Microsystems Lab.

Finally, yet importantly, I thank my family and friends without whose support and encouragement, it was impossible to accomplish this journey.

TABLE OF CONTENTS

LIST OF TABLES

LIST OF FIGURES

Chapter 1

INTRODUCTION

Magnetooptical (MO) effects are the phenomena occurred by the interaction of light with a magnetized matter due to the angular momentum that is transferred between the photons and the magnetic moments in the matter. When a circularly polarized light component interacts with matter, the charged particles in the matter are affected by the angular momenta of the photons, which leads to their circular motion. The circular motions of the charged particles result in oppositely directed effective magnetic fields for left- and right-hand circularly polarized (LHCP and RHCP) light beams. For a magnetized matter, LHCP and RHCP components experience different net fields and thus, interact and propagate in a dissimilar manner. In other words, the permittivity values and refractive indices for LHCP and RHCP light would be different.

Light with linear polarization can be considered as a superposition of an LHCP and an RHCP component with identical amplitudes and a phase difference that defines its polarization angle. When a linearly polarized light is incident on a magnetized material, the different refractive indices for its LHCP and RHCP components lead to a relative phase accumulation between the two components which causes a change in the polarization angle of the resultant beam. Such a rotation in polarization plane of a linearly polarized light beam when it passes through or reflects from a magnetized material is called MO Faraday or Kerr effect, respectively. The intensity of MO effects depends on the material properties and frequency of light [1]–[5].

In the quantum mechanical explanation, magnetooptical effects can be defined as a second-order perturbation on the combined electron and spin wavefunctions. The angular

momenta transferred from photons to the orbital and spin angular momenta of electrons results in a shift in light polarization due to the MO effects.

The MO effects can distinctively impact the electromagnetic (EM) waves or electronic and spin structure of materials [6], which can be applied in analytical chemistry and different spectroscopic methods such as IR or visible magnetooptical spectroscopy [7]–[9], x-ray magnetic circular dichroism (XMCD) [10]–[12], Brillouin light spectroscopy (BLS) [13] as well as other applications such as data storage [14]–[17], sensing/imaging systems [18]–[20], polarized microscopy [21]–[23], and spintronic devices [24]–[26]. Other applications of MO effects include optical devices such as isolators [27]–[29], circulators [30]–[32], and more importantly, spatial light modulators [33]–[35] that are a crucial part of a variety of photonic devices like projectors and display systems, holograms, optical interconnects, visible light communication apparatus, and functional Raman microscopy [36]–[40].

Spatial light modulator (SLM) is an optical device which uses an array of pixels controlled by external signals to alter the amplitude, phase, or polarization of a wavefront as a function of position [41]. SLMs can modulate light in a binary or analog manner, changing only phase [42]–[45] or amplitude [46], [47], or work in a phase-amplitude mode [48], [49]. The developed SLM types are either digital micromirror devices (DMDs) or liquid crystal (LC)-based devices, which include liquid crystal displays (LCDs), liquid crystal on silicon (LCOS), and ferroelectric liquid crystal on silicon (FLCOS). A summary of the state-of-the-art SLM products in the market is provided in Table 1.1. LCOS devices have smaller pixel sizes (min. pixel pitch of 3.74 μm) with long response times (~ milliseconds), whereas DMDs are faster (response times of ~10 μs), but have larger pixels (min. pixel pitch of 5.4 μm).

Table 1. 1. Specifications of the state-of-the-art SLM products (LC: liquid crystal, LCOS: liquid crystal on silicon, FLCOS: ferroelectric liquid crystal on silicon, and DMD: digital micromirror device).

Device Manufacturer & Model	Type	Modulation mode	Response time/ Frame rate	Pixel pitch (μm)	Resolution (pixels)	Power consumption (W)	Waveband (nm)
HOLOEYE LC 2012 [50]	LC Translucent	Phase/ amplitude Analog	60 Hz	36	1024 × 768	1-2	420-800
HOLOEYE GAEA-2 [51]	LCOS Reflective	Phase Analog	58 Hz	3.74	4160 × 2464	12	420-1100 1400-1700
Jasper Display Corp. SRK4K – JD7714 [52]	LCOS Reflective	Phase Analog	30 Hz	3.74	4096 × 2400	24	430-750
Hamamatsu X13138 series [53]	LCOS Reflective	Phase Analog	60 Hz	12.5	1280 × 1024	50	400-1550
Meadowlark Optics ODP512 [54]	LCOS Reflective	Phase Analog	3-6 ms	15	512 × 512	15	400-1650
Forth Dimension Displays M180 [55]	FLCOS Reflective	Phase/ amplitude Analog	75 Hz	8.2	2048 × 2048	-	430-700
Texas Instruments DLP 4710 [56]	DMD Reflective	Amplitude Binary	10 μs	5.4	1920 × 1080	0.804	-

The above-mentioned SLMs are final products that fulfill different application requirements, yet not capable of simultaneous high-speed modulation and fine spatial resolution, which is crucial for applications such as holography and 3D imaging. Video holograms with high quality require SLMs with large space bandwidth product (SBP) and fast response time. SBP is the product of spatial bandwidth and physical size of SLM, which is determined by the total number of pixels in an SLM. A trade-off between the field of view (FoV) and the size of the viewing window (eye box) exists for a constant SBP. A large number of pixels is required for a practical holographic imaging, where both large FoV and large eye box are important, SLMs with high pixel counts are required. Due to prohibitive growing of the system sizes and involved driving optics and electronics, in most applications, it is not feasible to increase the size of SLM for this purpose. Therefore, the solutions suggest to reduce the pixel sizes. Furthermore, large pixels lead to overlap of diffraction orders and aliasing noise along with narrow viewing zone, according to:

$$\theta = 2\sin^{-1}\left(\frac{\lambda}{2p}\right) \tag{1.1}$$

where θ, λ, and p are the viewing angle, wavelength, and pixel pitch, respectively. According to equation 1.1, the pixel pitches on the order of the light wavelength (< 1 μm for visible) are required for an acceptable viewing angle [57]–[60]. Summarising the discussion above, SLMs with small pixel sizes, large pixel counts, and fast enough to address a large number of pixels in a single frame are desired for holography and 3D displays. The ongoing research for reducing the pixel size [45], [61]–[66] and decreasing the response time [67]–[70] of SLMs has demonstrated plenty of designs and prototypes. However, a practical active SLM having a large number of pixels, small pixel size, and short response time has not been realized yet.

Exploiting MO effects for light modulation introduces a new type of SLMs, named magnetooptical spatial light modulators (MOSLMs), which are promising in satisfying the requirements mentioned above. In this type of SLMs, MO effects provide polarization rotation and using polarizers allows for passing only certain polarization components. As a result, controlling the magnitude of rotation (intensity of the MO effect) tunes the intensity

of the outcoming beam and enables light modulation. A pixel can be switched by reversing its magnetization state, which changes the direction of the Faraday/Kerr rotation [71]. Figure 1.1 describes the working principle of MOSLMs. An unpolarized light beam gains linear polarization after passing through a polarizer. The linearly polarized light is directed to the MO pixels, and a polarization rotation (θ_F or $-\theta_F$) is achieved according to the magnetization direction of the pixel (due to magnetic field H or -H, respectively). A second polarizer that is called analyzer is placed on the way of the exiting light. Based on the achievable rotation degree, the analyzer is set with an angle to the polarizer so that it is approximately aligned with the light rotated in one of the directions, e.g. θ_F in Figure 1.1. Thus, almost all the light coming from a pixel magnetized in H direction passes through the analyzer and such a pixel represents an ON status. However, the light rotated in the opposite direction ($-\theta_F$) has no or small component parallel to the analyzer, which results in no or weak outcoming light for the pixels magnetized in -H direction (OFF status). Figure 1.2 shows a 128 × 128 MOSLM and two different patterns formed by ON and OFF pixels in such an MOSLM. The switching of pixels in this MOSLM was realized by the conductor drivelines stretched from the pixel array towards the chip edges [58].

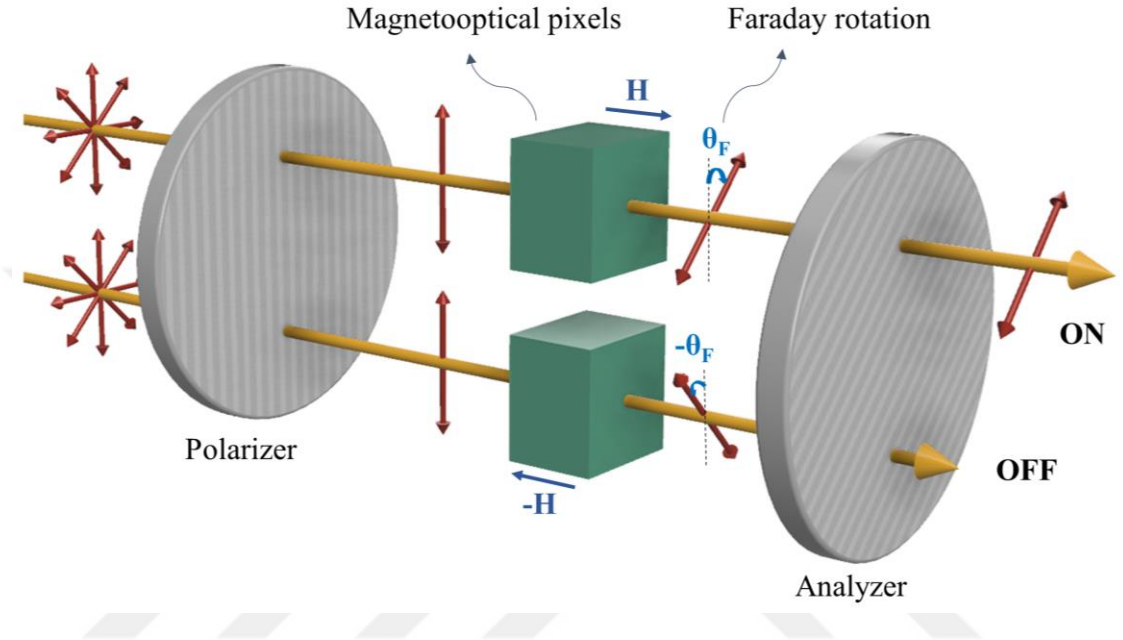

Figure 1. 1. Working principle of MOSLMs.

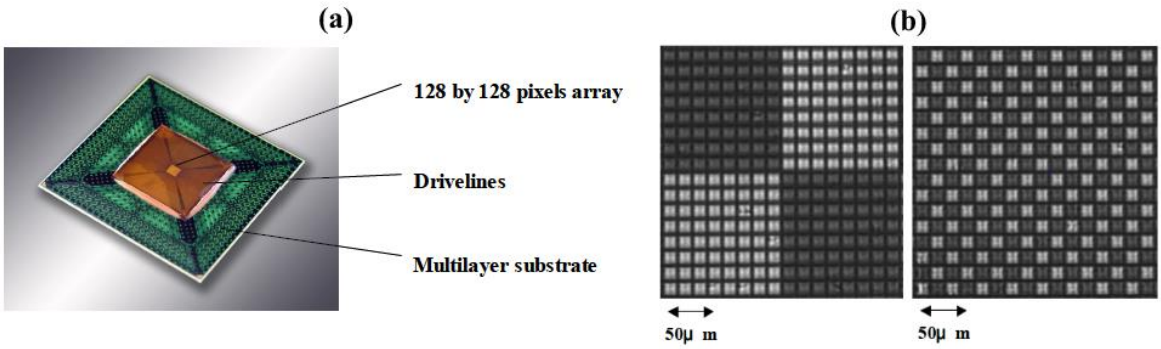

Figure 1. 2. (a) A 128 × 128 MOSLM and (b) two different patterns formed by ON and OFF states in a 16 × 16 pixels area of this MOSLM [58].

MO effects and magnetization switching are intrinsically fast phenomena happening in time scales in the order of nanoseconds [72]–[74] down to femtoseconds [75] or less [76]. Thus, MOSLMs could enable ultrafast light modulation and extend the modulation frequencies to multi-THz rates. MOSLMs can also take advantage of magnetic remanence

property, which brings about nonvolatility and enable them to act as memory elements capable of saving data in even after power cut-off. Moreover, MOSLMs are robust solid-state devices that can eliminate drawbacks of mechanically moving parts and complex fabrication in DMDs, or crosstalk between pixels in LC-based devices which originates from the liquid state of the material and no physical partitioning of the pixels [37], [38]. Employing magnetism in MOSLMs makes it possible to use monolithically integrated thin films for modulation and allows for realizing smaller pixels. Active control of magnetization by external electrical signals [77]–[79], enabling independent switching of every pixel, turns MOSLMs into active and programmable integrated devices. Combination of the mentioned features makes MOSLMs superior for holographic applications and 3D displays [80]–[82], augmented (AR) and virtual reality (VR) devices, beam steering devices for photonic projectors and other imaging applications [83], [84], optical isolators and circulators [85], light detection and ranging (LIDAR), and visible light communications [86].

Despite the above-mentioned advantages, there are challenges associated with MOSLMs that have held back their practical applications. The inherent weakness of MO effects is the main issue in this regard. The rotation angle achieved by the MO effect, which is proportional to magnetization (M), define the modulation depth and contrast of MOSLM. At maximum M, i.e saturation magnetization (M_s), Kerr rotation is generally in the order of milliradians and Faraday rotation is proportional to the light path length in the MO material. Therefore, enhancement of MO effects is crucial for practical miniaturized and integrated MO devices [1], [35], [87]. Another challenge with MOSLMs that has hindered their industrial development is the prohibitively high energy consumption originating from high magnetic fields demand for switching the pixels and optical power required for compensation of large optical losses in the MO materials. Moreover, in conventional current-driven MOSLMs, Joule heating increases energy consumption and causes switching errors and reliability issues [58], [88].

Table 1.2 presents a summary of prototype MOSLM demonstrations in the literature. Comparison of Tables 1.1 and 1.2 shows that early MOSLM prototypes had frame rates

higher than 1 kHz in the visible range, which makes them advantageous over the state-of-the-art SLM products with frame rates below 100 Hz. Power consumption of SLM products is in the range of 1-50 W and switching power for MOSLM prototypes is below 1 W, however, the power values stated for MOSLM prototypes exclude consumption of driving electronics and optics. Hence, a valid comparison of power consumption can only be done after MOSLMs turn into products. In terms of pixel pitch, pixel count, wavelength range, and the modulation types, there is still a lot of room for improvement in MOSLMs.

Table 1. 2. Prototype demonstrations of magnetooptical spatial light modulators (MOSLMs).

Ref., year	Modulation mode	Switching time /Frame rate	Pixel pitch (μm)	Number of pixels	Switching requirements	Wavelength (nm)
Krumme et al. [89], 1977	Amplitude Binary	10 μs	20	384 × 384	1 μW + 100 Oe + 1.2×10^{4} $V\cdot cm^{-1}$	632.8
Ross et al. [33], 1983	Amplitude Binary	1 μs	100	48 × 48	1 W	-
Cho et al. [72], 1994	Amplitude Binary	> 1 kHz	24	128 × 128	> 100 mW	685
Park et al. [90], 2003	Amplitude Binary	-	105	5 × 5	40 Oe + 8 V (sinusoidal, 10 MHz)	-
Park et al. [38], 2003	Amplitude Binary	-	18	16 × 16	45 Oe (or 16 mA)	532
Park et al. [91], 2004	Amplitude Binary	-	18	16 × 16	120 mA + 20 Oe	-
Iwasaki et al. [58], 2006	Amplitude Binary	25 ns	16	128 × 128	879 mW	532

Lately, considerable breakthroughs have been demonstrated in the materials engineering, fabrication methods, and magnetization switching methods. Cutting-edge deposition techniques such as pulsed laser deposition (PLD) and advanced sputtering systems enable the synthesis of materials with high MO quality. Advanced micro/nanofabrication and characterization methods facilitate the fabrication of small pixels. The recent discovery of low-power mechanisms for controlling magnetism may help for a remarkable reduction of power consumption. Overall, proper exploitation of these advances offers a potential opportunity to empower novel ultrafast, low-power, and nonvolatile SLMs.

In this chapter, various MO materials are evaluated for spatial light modulators. The challenges on the way of further development of MOSLMs and suggested solutions in the literature are reviewed. Different device architectures and potential switching methods with their advantages and disadvantages are discussed. Finally, the contribution of this thesis to the field is presented.

1.1 Magnetooptical Materials

Magnetic materials with nonzero magnetization, i.e. ferro/ferrimagnets are the most common materials to show MO effects; however, antiferromagnetic materials have been reported with MO properties as well [92]–[94].

The property of a magnetooptical or gyrotropic material can be described by an antisymmetric permittivity tensor, which has the following form assuming the magnetization in the z direction:

$$\varepsilon = \begin{pmatrix} \varepsilon_1 & +i\varepsilon_2 & 0 \\ -i\varepsilon_2 & \varepsilon_1 & 0 \\ 0 & 0 & \varepsilon_3 \end{pmatrix} \tag{1.2}$$

All the nonzero tensor elements have complex values with real and imaginary components. ε_3 has a value close or equal to ε_1, below and above Curie temperature (T_c), respectively. Under conditions of small magnetic fields and linear MO effects, it is valid to assume $\varepsilon_3 = \varepsilon_1$

and simplify the matrix into two elements, diagonal (ε_{xx}) and off-diagonal (ε_{xy}) [95]–[97]. The diagonal element $\varepsilon_{xx} = \varepsilon_1$ represents the optical properties including refractive index (n) and extinction coefficient (k) of the material. The off-diagonal element $\varepsilon_{xy} = \varepsilon_2$ is related to the difference in refractive indices $n_{\pm}$ and extinction coefficients $k_{\pm}$ for LHCP and RHCP components of light. The magnitude of ε_2 shows the intensity of the MO effect [98], [99]. In materials with non-zero off-diagonal elements, LHCP and RHCP components of a linearly polarized light experience dissimilar refractive indices and propagate at different velocities. Consequently, a relative phase difference is formed between the two components, which leads to rotation in the polarization plane of the incident light (Faraday/Kerr rotation). Furthermore, due to the different extinction coefficients, LHCP and RHCP components are attenuated with different rates. Hence, the amplitudes of these components would be different at the output, which results in Faraday/Kerr ellipticity. While there is no direct relationship between the diagonal elements in the permittivity tensor and magnetization (M), ε_2 has a linear dependence on M [100].

The occurrence of MO effects can be explained in three different ways based on the material types. In the first category, MO effects are the result of the direct influence of the magnetic field on orbital motions of the electrons, and ε_2 is principally a function of the magnetic field (H). This category includes all diamagnetic materials including organic molecules and planar molecules with at least one uniaxial symmetry. In the second category, MO effects stem mainly from the spin-orbit coupling in aligned spins, and the direct impact of the magnetic field is negligible. In other words, the magnetic interaction of an oriented spin has a much stronger effect on the electronic orbital motion, in comparison to the direct effect of an external magnetic field. In this category which includes ferromagnetic and nonmetallic paramagnetic materials at low temperatures, ε_2 is considered to be a function of M rather than H. The third category which represents a transition between the stated classes, includes semiconductors and nonferromagnetic metals. In this category, there is no explicit distinction and both direct action of the magnetic field and spin-orbit interactions play significant roles in the emergence of the MO phenomena [101]. The role of spin-orbit

interactions in the MO effects was quantitatively investigated by Misemer [102], who reported a nearly linear relation between MO coefficients and spin-orbit coupling, in transition metals.

Magnetooptics involves an interplay between absorption of light and rotation of the polarization plane, where a strong dependence on the electronic band structure exists. Therefore, MO materials can be classified based on their band structures as follows:

1.1.1 Dielectrics

Dielectric MO materials including different magnetic oxides, ferrites, spinels, sulfides, and trihalides are mostly transparent and suitable for the Faraday effect, which is generally a larger MO effect and preferred for practical applications [1]. In this category, ferrimagnetic iron garnets with the formula of $R_3Fe_5O_{12}$ (R representing a rare-earth element) generally show unique MO properties. These garnets have a highly symmetric body-centered cubic (bcc) lattice with relatively large lattice constants of 1.2 – 1.3 nm. Substitutional elements could modify the lattice parameters and improve the MO properties [103], [104]. Table 1.3 presents a summary of the extensively studied MO materials synthesized through different fabrication methods. The material properties desired for MO devices include both large Faraday rotation and small optical loss, so MO figure of merit (FoM) is defined as:

$$\text{FoM}\ (\text{deg}\cdot\text{dB}^{-1}) = \frac{\text{Faraday rotation}\ (^\circ)}{\text{Optical loss}\ (\text{dB})} \tag{1.3}$$

In Table 1.3, the best FoM values for fundamental wavelengths red, green, and blue are calculated based on the data provided in the literature. Finite-difference time-domain (FDTD) simulations are used for these calculations, as explained in the Methods section in Chapter 2.

Table 1. 3. Figure of merit values calculated for different MO materials based on the values reported in the literature (FoM: figure of merit, SFR: specific Faraday rotation, α: absorption coefficient, ε_{xx}: diagonal element of permittivity tensor, ε_{xy}: off-diagonal element of permittivity tensor, T: transmission, n: refractive index, k: imaginary part of complex refractive index).

Material	Synthesis method	Blue (474 nm)		Green (520 nm)		Red (633 nm)		Ref.
		Reported values	Calculated FoM	Reported values	Calculated FoM	Reported values	Calculated FoM	
$Y_3Fe_5O_{12}$ (T<20K)	Epitaxial flux growth	SFR = 1.45 °·μm^{-1} α= 15333 cm^{-1}	0.22 °·dB^{-1}	SFR = 0.23 °·μm^{-1} α = 645 cm^{-1}	0.82 °·dB^{-1}	SFR = 0.04 °·μm^{-1} α = 245 cm^{-1}	0.38 °·dB^{-1}	[105] [106] [107]
$Bi_{0.7}Y_{2.3}F_5O_{12}$	Flux technique	-	-	FoM= 2.75 °·dB^{-1}	2.75 °·dB^{-1}	FoM = 3.22 °·dB^{-1}	3.22 °·dB^{-1}	[108]
$Y_3Fe_5O_{12}$	Milling and sintering	ε_{xx} = 5.94 + 0.15060i ε_{xy} = 0.00801 - 0.00251i	0.24 °·dB^{-1}	ε_{xx} = 5.52 + 0.02410i ε_{xy} = 0.00036 + 0.00012i	0.09 °·dB^{-1}	ε_{xx} = 5.34 + 0i ε_{xy} = 0.00084 + 0.00084i	0.08 °·dB^{-1}	[98]
$Bi_1Y_2Fe_5O_{12}$	Milling and sintering	ε_{xx} = 7.19 +0.55723i ε_{xy} = -0.06631 -0.14457i	1.45 °·dB^{-1}	ε_{xx} = 6.64 + 0.03313i ε_{xy} = -0.07499 - 0.00634i	9.62 °·dB^{-1}	ε_{xx} = 6.04 + 0i ε_{xy} = - 0.01697 + 0.00176i	1.18 °·dB^{-1}	[98]
$FeBO_3$	Vapor-phase transport	SFR = 0.42 °·μm^{-1} α = 418 cm^{-1}	2.31 °·dB^{-1}	SFR = 0.21 °·μm^{-1} α = 21 cm^{-1}	23.03 °·dB^{-1}	SFR = 0.08 °·μm^{-1} α = 98 cm^{-1}	1.88 °·dB^{-1}	[107] [109]
$NiFe_2O_4$	Conventional ceramic technology	n = 2.53 + 0.79059i ε_{xy} = 0.01326 - 0.01889i	0.04 °·dB^{-1}	n = 2.62 + 0.68830i ε_{xy} = - 0.00072 - 0.00923i	0.02 °·dB^{-1}	n = 2.58 + 0.38044i ε_{xy} = -0.00077 -.00005i	0.002 °·dB^{-1}	[110]
$Y_{1.93}Bi_{1.07}Fe_5O_{12}$	Liquid phase epitaxy	ε_{xx} = 7.70 +2.00718i ε_{xy} = - 0.02954 - 0.16213i	0.47 °·dB^{-1}	ε_{xx} = 7.95 + 0.89612i ε_{xy} = 0.06470 - 0.04779i	0.51 °·dB^{-1}	ε_{xx} = 6.40 + 0.04003i ε_{xy} = 0.01536 - 0.002064i	1.97 °·dB^{-1}	[111]
$(BiDy)_3(FeGa)_5O_{12}$	Sputtering	ε_{xx} = 6.96 + 1.290393i ε_{xy} = - 0.06934 - 0.00559i	0.35 °·dB^{-1}	ε_{xx} = 5.79 + 0.51333i ε_{xy} = 0.00020 + 0.01680i	0.19 °·dB^{-1}	ε_{xx} = 5.20 + 0.09728i ε_{xy} = 0.01164 - 0.00233i	0.51 °·dB^{-1}	[112]
$Lu_{2.5}Bi_{0.5}Fe_5O_{12}$	Liquid phase epitaxy	ε_{xx} = 6.88 + 0.60002i ε_{xy} = 0.00588 - 0.05661i	0.55 °·dB^{-1}	ε_{xx} = 6.43 + 0.19270i ε_{xy} = - 0.01176 + 0.01342i	0.41 °·dB^{-1}	ε_{xx} = 5.78 + 0.02631i ε_{xy} = - 0.00323 + 0.00506i	0.02 °·dB^{-1}	[100]

$Lu_{2.3}Bi_{0.7}Fe_{4.4}Ga_{0.6}O_{12}$	Liquid phase epitaxy	ε_{xx} = 6.48 + 0.44424i ε_{xy} = - 0.00323 - 0.07393i	0.90 °·dB^{-1}	ε_{xx} = 6.17 + 0.16254i ε_{xy} = - 0.02049 - 0.01245i	0.49 °·dB^{-1}	ε_{xx} = 5.62 + 0.02133i ε_{xy} = - 0.00607 + 0.00370i	0.21 °·dB^{-1}	[100]
$Bi_3Fe_5O_{12}$	Rf-magnetron sputtering	-	-	FR = 11.83° T = 0.71 %	0.55 °·dB^{-1}	FR = 5.38 ° T = 69 %	3.34 °·dB^{-1}	[74]
$Gd_{1.24}Pr_{0.48}Bi_{1.01}Lu_{0.27}Fe_{4.38}Al_{0.6}O_{12}$	Liquid phase epitaxy	ε_{xx} = 7.52 + 0.96644i ε_{xy} = 0.13229 - 0.05390i	0.91 °·dB^{-1}	ε_{xx} = 6.82 + 0.12387i ε_{xy} = 0.01803 - 0.05864i	2.88 °·dB^{-1}	ε_{xx} = 6.06 + 0.03278i ε_{xy} = - 0.00130 - 0.01759i	1.15 °·dB^{-1}	[113]
$Ce_1Y_2Fe_5O_{12}$	Pulsed laser deposition	FoM = 0.12 °·dB^{-1}	0.12 °·dB^{-1}	FoM = 0.096 °·dB^{-1}	0.096 °·dB^{-1}	FoM = 0.16 °·dB^{-1}	0.16 °·dB^{-1}	[114]
$Bi_{1.5}Y_{1.5}Fe_5O_{12}$	Metal organic decomposition	SFR= 5.82 °·µm^{-1} k= 0.2869	0.18 °·dB^{-1}	SFR = 8.16 °·µm^{-1} k = 0.1913	0.41 °·dB^{-1}	SFR = 1.90 °·µm^{-1} k = 0.0171	1.29 °·dB^{-1}	[115]
$Bi_2Y_1Fe_5O_{12}$	Metal organic decomposition	SFR= 14.60 °·µm^{-1} k= 0.3263	0.39 °·dB^{-1}	SFR = 16.05 °·µm^{-1} k = 0.2093	0.73 °·dB^{-1}	SFR = 3.47 °·µm^{-1} k = 0.0168	2.40 °·dB^{-1}	[115]
$Bi_{2.5}Y_{0.5}Fe_5O_{12}$	Metal organic decomposition	SFR= 24.06 °·µm^{-1} k= 0.4477	0.47 °·dB^{-1}	SFR = 20.1 °·µm^{-1} k = 0.2450	0.78 °·dB^{-1}	SFR = 5.72 °·µm^{-1} k = 0.0134	4.95 °·dB^{-1}	[115]
$Bi_3Fe_5O_{12}$	Metal organic decomposition	SFR= 35.27 °·µm^{-1} k= 0.5327	0.58 °·dB^{-1}	SFR = 25.44 °·µm^{-1} k = 0.2912	0.83 °·dB^{-1}	SFR = 6.84 °·µm^{-1} k = 0.0069	11.49 °·dB^{-1}	[115]

It can be concluded From Table 1.3 that FoM is generally below 1 °·dB^{-1}, but doping iron garnets with elements like Bi could significantly improve the FoM [115]. Although Iron borate ($FeBO_3$) shows an outstanding FoM, it has attracted less interest for MO applications due to two main issues. First, growing single-crystalline $FeBO_3$ in sufficiently large scales is a challenging process. Second, the complications arising from its birefringence make $FeBO_3$ a difficult option for MO studies [107], [116].

1.1.2 Metals

MO properties in metals and alloys are governed by the difference in the density of electrons with up and down spins, near the Fermi level, in addition to the oscillator strength of the optical transitions. Hence, a direct explanation of the MO effects from microscopic point of view is not intuitive in the metals, nevertheless, first-principle calculations give a hint [1].

Magnetic transition metals such as Fe, Ni, Co, and their alloys are the most common metallic MO materials. Rare earth-transition metallic and intermetallic compounds also show MO effects. MO activity has been observed even in the noble metals, yet much weaker than the ferromagnets. High reflectivity and low transmission in metals make them more suitable for the Kerr effect. MO Kerr effect (MOKE) has been used for imaging magnetic domains, investigation of the magnetic hysteresis behavior and high-resolution dynamics in magnetism [117]–[121]. However, MO metals have been of less interest for MOSLMs, because of the generally small magnitude of the Kerr effect and large absorption of metals for the Faraday effect [122], [123].

In Figure 1.3, MOKE as a function of magnetization is presented for some metals and insulators. The MO Kerr rotation angle $|\theta_K|$ was measured in the polar arrangement (M perpendicular to the film plane) at room temperature. In ferri/ferromagnetic films, there is generally a linear relationship between $|\theta_K|$ and the magnetization, i.e. $|\theta_K| = K_s M$, where K_s is coefficient in the range of 0.2-2 deg·T^{-1} (the shaded region in Figure 1.3). For antiferromagnetic insulators, K_s has a value within 10-20 deg·T^{-1} (the gray signs in the figure). Mn_3Sn is an antiferromagnetic metal with a larger K_s of 25.6 deg·T^{-1} [94].

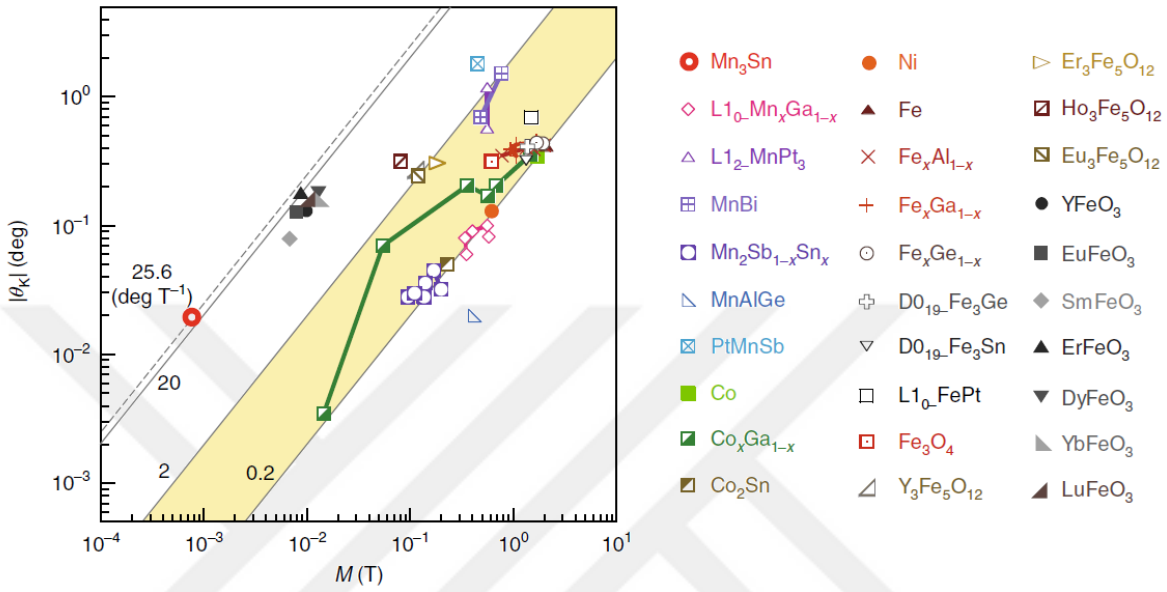

Figure 1. 3. Polar MO Kerr rotation angle $|\theta_K|$ measured as a function of magnetization for various ferro-, ferri-, and antiferromagnetic materials at room temperature [94].

1.1.3 Semimetals and 2D materials

The conventional MO materials studied widely to date and used for prototype MO devices are dielectrics and metals. However, recently a new class of materials, namely semimetals and two-dimensional (2D) materials, have proved potential for MO properties. The utilization of these materials is promising for realizing revolutionary dense MO and spintronic devices.

Graphene, an atomically thin layer of graphite, is the most common material in this class. Graphene has a semimetallic behavior and distinctive mechanical, optical, and thermal properties [124]. Theoretical studies reported MO properties in graphene [125], [126]. The first experimental study in this regard was performed by Crassee et al. in 2011 [127], who investigated MO properties of epitaxial graphene on SiC substrate. They reported an increase of the Faraday rotation (FR) with the magnetic field and observed rotation angles up to 0.1 rad (~6º) for a single-layer graphene, under a magnetic field of 7 T and 5 K temperature

(Figure 1.4a). Furthermore, they discovered that the magnetic field remarkably affects the absorption and transmission in graphene (Figure 1.4b).

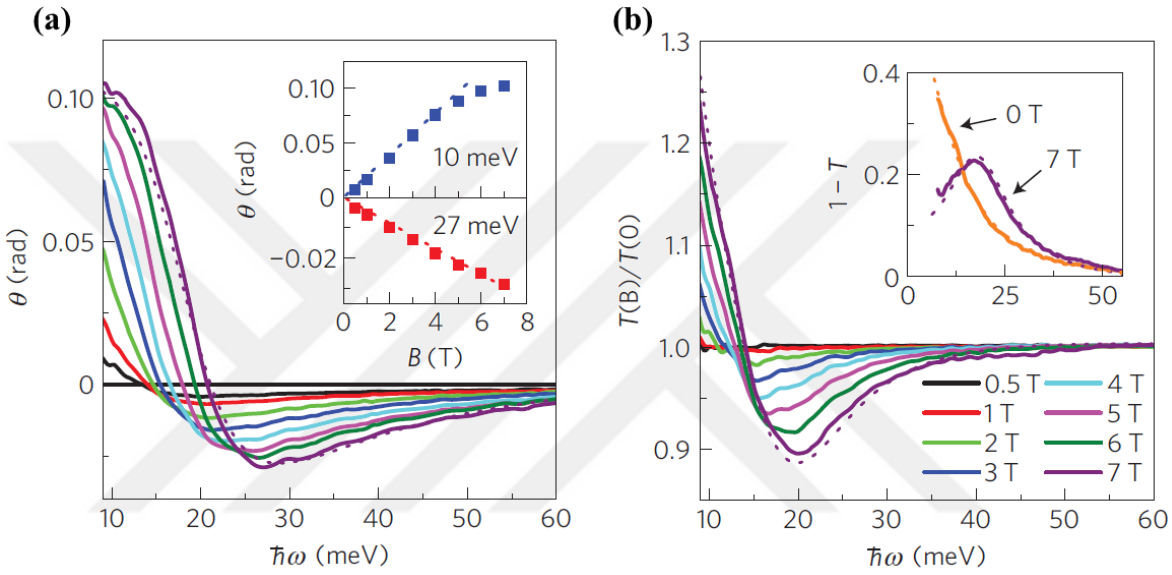

Figure 1. 4. Faraday rotation and magnetooptical transmission spectra of single-layer graphene grown on SiC substrate. (a) Faraday angle θ measured at 5 K under different magnetic fields. The inset shows the magnetic field dependence of θ at photon energies ħω = 10 and 27 meV. (b) The zero-field-normalized transmission spectra under the different magnetic fields. The inset shows the absorption (1−T) under 0 and 7 T magnetic fields [127].

In another study, they suggested enhancing the FR in graphene, by constructive Fabry-Perot interference from the substrate. Their theoretical calculations demonstrated giant rotation angles, as large as 0.15 rad (~9º), for multilayer graphene on SiC substrate [128]. Using THz time-domain spectroscopy (THz-TDS), Shimano et al. [129] reported Kerr effect along with the Faraday effect in graphene. These effects were explained by Falkovsky [130] to be a result of a Hall component that appears in the conductivity tensor of graphene, σ_{xy}, when a magnetic field is applied. The off-diagonal component σ_{xy} breaks rotational symmetry around the major axis and implies a polarization rotation for a linearly polarized EM wave, i.e. MO Faraday/Kerr effect. He showed that for a freely suspended graphene under a

magnetic field of 7 T, Faraday rotations as large as 0.25 rad can be attained. Tuning the MO properties of graphene through innovative methods such as applying strain [131], [132] and electrostatic doping [133] at zero or fixed magnetic fields introduces novel means for controlling MO effects in the new generation of opto-electro-mechanical devices based on 2D materials.

MO effects have been studied in 2D materials other than pristine graphene, likewise. It was demonstrated by first-principles calculations that in 2D nitrogen-graphene crystals (different substitutions of C atoms with N in graphene), the intensity of MO effects is highly dependent on the concentration of the carriers, thus could be controlled by a gate voltage [124]. Silicene (a 2D allotrope of silicon) has also proven remarkable MO properties. According to theoretical modeling, a silicene monolayer is capable of demonstrating 8º Faraday and 13º Kerr rotation in the terahertz regime [134]. Phosphorene [135], molybdenum disulphide (MoS_2) [136], tungsten diselenide (WSe_2) [137], chromium triiodide (CrI_3) [138]–[140], and $Cr_2Ge_2Te_6$ [141], [142] are the other 2D materials studied for MO applications.

In the past years, MO effects have been investigated in bulk semimetals as well. In fact, MO properties bring about a scheme to differentiate Weyl and Dirac semimetals [143]–[145]. MO measurements can serve for probing chiral anomaly in the Weyl semimetal state that can be found in nonmagnetic and noncentrosymmetric transition-metal monoarsenides or phosphides such as TaAs [146] and NbP [147]. Different behavior is observed in Dirac semimetals like single-crystalline bulk Cd_3As_2, according to Zhang et al. [148]. They performed rotational magnetooptical Kerr effect measurements and showed that under a magnetic field, the Kerr effect only happens when a current is applied across the sample. The rotation proved to be maximum for parallel magnetic and electric fields and it increased with both the magnetic field and the current density.

The materials discussed in this subsection offer new mechanisms and exceptional MO properties, however, they need to function at ambient conditions and with acceptably low magnetic fields for practical applications.

1.1.4 Materials engineering for improvement of MO properties

Fabrication processes and parameters have a significant role in MO properties due to their effect on the final stoichiometry, crystallographic and phase structure, and other factors such as defect density and residual stresses [149]. For obtaining decent MO properties, a variety of materials with different compositions and structures have been studied in the literature. Various synthesis methods and experimental conditions are tested, and composite MO materials are fabricated for this purpose. Ex-situ and thermal treatments after deposition have been examined to obtain pure phases and better crystallization to improve the MO properties [150]–[153].

Among the numerous efforts to produce materials with better MO properties, doping iron garnets with elements like Bi [154]–[157], Ce [158]–[161], and Nd [162] has become a standard approach. Doped garnets have higher potential for application in nonreciprocal devices, because of the higher MO FoM in comparison to undoped ones. Hansen et al. [163], [164] showed that in Bi-doped garnets, FR has a linear relationship with the amount of Bi substitution.

Epitaxial growth of garnets on Gadolinium Gallium Garnet (GGG) substrates with lattice match [103] is a widespread fabrication method for MO films, however, growing garnets on non-garnet substrates is challenging due to the lattice coefficient mismatch, which causes inconsistent thermal expansions leading to stress and cracks, forms undesired secondary phases, or results in incomplete crystallization [165]. These issues impede the fabrication of high-quality films and diminish the transmission and MO properties. In 2005, Sung et al. [166] showed a breakthrough and grew yttrium iron garnet (YIG) on non-garnet substrates, using RF sputtering followed by a rapid thermal annealing. Nevertheless, in the case of the doped garnets, similar attempts were not entirely successful and research is going on to integrate doped garnets to common non-garnet substrates such as glass and silicon. It was shown by Furuya et al. [167] that a hematite underlayer with spinel structure could significantly improve the MO properties in Bi-doped garnets deposited on quartz substrates. Later studies suggested using a seed layer of undoped YIG at the bottom or top, for assisting

better crystallization of doped garnets on non-garnet substrates, which ensures improved film properties [85], [168], [169]. It was subsequently reported that for the terbium iron garnet (TIG) family, even with Bi or Ce substitutions, no seed layer is necessary for integration to non-garnet substrates [157], [161].

The following studies signify other efforts in terms of materials engineering for MO devices: Nur-E-Alam et al. [170] sandwiched MO films with in-plane easy axes between out-of-plane MO films and achieved high-quality MO heterostructures that had small coercivity and nearly perpendicular magnetization. Chen et al. [171] incorporated YIG crystals into phosphorus-based glass and reported enhancement of FR with YIG content, while annealing temperature had a reverse effect on FR value. Sadatgol et al. [172] fabricated MO metamaterials with improved MO properties, by embedding nonmagnetic conductor wires into an MO material. It was explained that the enhancement in MO effects is not due to plasmonic resonances and occurs by tuning the permittivity of the MO material near the diluted plasma frequency. As a result, the enhancement can be tailored by modifying the geometry of the metamaterial structure and it offers wider operation bandwidth and lower losses in comparison to resonant approaches. Gu et al. [173] calculated enhancement of MO Kerr effect in Fe/insulator interfaces proportional to σ_{xy}/σ_{xx} (the ratio of off-diagonal to diagonal elements of the optical conductivity tensor). Such enhancement could be justified by an increase in the orbital magnetic moments and spin-orbit couplings of the interfacial Fe atoms.

In addition to the materials engineering aspect discussed above, enhancement of MO effects has been sought through the device engineering as well. Based on these endeavors, different MOSLM structures have formed which will be discussed in detail in the following section.

1.2 Magnetooptical enhancement and different structures for MOSLMs

As explained before, for realizing miniature and integrated devices for high-edge applications, it is necessary to enhance MO effects but prevent increase of optical losses over acceptable levels. Device engineering has proven productive in this regard. It is described

below, how different designs have served this purpose and improved the functionality of MOSLMs:

The first MOSLM consisted of magnetic garnet pixels on a nonmagnetic substrate, which operated in transmission mode and were controlled by the thermal energy of a laser beam [89]. In 1994, Cho et al. [72] introduced a reflection-mode MOSLM based on the Faraday effect and reported significant improvement of pixel switching sensitivity, resolution, and optical efficiency. Using a reflector on the backside of the MO film, they were able to obtain a double rotation angle in comparison to the conventional transmission mode. As illustrated in Figure 1.5, the light enters from the transparent substrate, propagates through the MO film, reflects from the back reflector, traverses the MO film for the second time, and eventually exits from the substrate. MO effects are nonreciprocal phenomena, where the change in propagation direction does not alter the direction of polarization rotation, as long as the sign of the magnetic field is unchanged. In other words, the sign of MO effects depends on the sign of the magnetic field rather than the propagation vector. Thus, the new design enabled a double FR angle by realizing a two-fold path length for light, in the same film thickness. Considering θ_F as the specific Faraday rotation of the material, a film with thickness of d provides a rotation angle equal to $\theta_F \cdot d$ in transmission-mode device, while the new design allows for $2\theta_F \cdot d$ rotation, which can be switched by reversing the magnetization direction (Fig. 1.5). This approach was the first measure in device engineering for enhancing MO effects and became a part of the later designs.

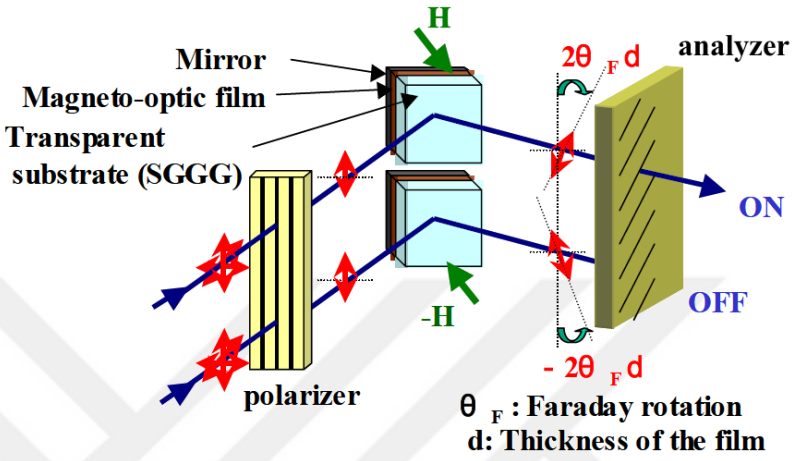

Figure 1. 5. Working principle of a reflection-mode MOSLM based on the Faraday effect, which could achieve a double rotation angle ($2\theta_F \cdot d$) in comparison to the conventional transmission-mode ($\theta_F \cdot d$). θ_F is the specific Faraday rotation [58].

The other methods in the context of device engineering for enhancement of MO effects that have attracted extensive attention in the literature are described in the subsections below:

1.2.1 Magnetophotonic crystals

One of the approaches widely used for enhancing MO effects is exploiting photonic crystals, which are periodic structures with alternating regions having high and low refractive indices. When the periodicity is in one dimension, the structure is called 1D photonic crystal, and a 1D photonic crystal with dielectric components is known as Bragg mirror. The periodic structure of a photonic crystal breaks the continuous translational symmetry, which prevents propagation of EM waves within a certain wavelength range and forms a photonic bandgap. Indeed, the bandgap of a photonic crystal stems from the destructive interference of multiple reflections of the wave from the interfaces of the high- and low-index layers. Creating defects in the periodic structure of a photonic crystal further breaks its discrete translational symmetry, which forms transmission peaks in the bandgap. Such defects play the role of optical cavities and trap the light, which leads to greater light-matter interactions.

When an MO material is used as the defect layers in the photonic crystal cavities, the structure is called a magnetophotonic crystal (MPC) [23], [83], [174]–[180]. MPC enables significant enhancement of MO effects due to the confinement of light in the MO cavity. Intuitively, the light reflects back and forth multiple times in the cavity, which increases its path length in the MO material and accumulates MO effects, owing to the nonreciprocity of these phenomena. A single-defect MPC [35] is schematically illustrated in Figure 1.6a, where an MO film is sandwiched between two Bragg mirrors. The transmission spectra from both experimental and calculation results show a bandgap including a transmission peak (Figure 1.6b). Faraday rotation spectra (Figure 1.6c) show that at the wavelengths correlated to the transmission peak, the MPC yields expressively higher FR values in comparison to the single-layer MO film.

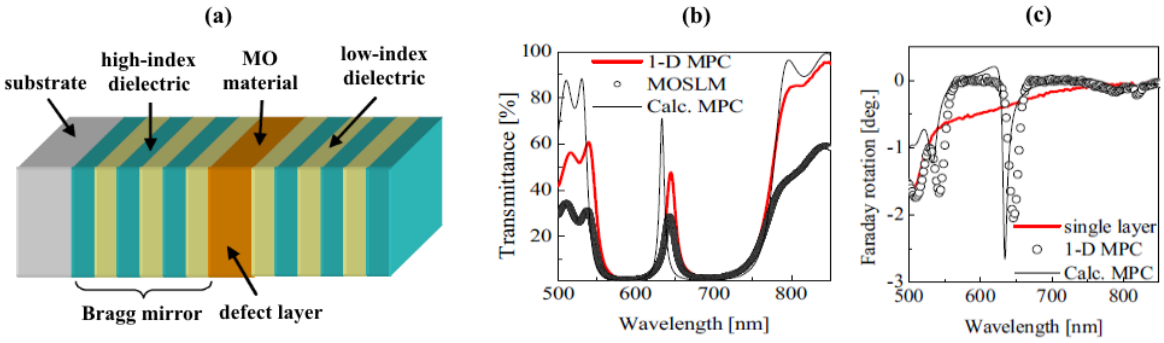

Figure 1. 6. Photonic crystal-based enhancement of MO effects. (a) Schematic of a single-defect magnetophotonic crystal (MPC). (b) Transmission spectra from the experimental results for the MPC (red line) and a pixelated MOSLM composed of the MPC (hollow dots), as well as the calculated results for the MPC (black line). (c) Faraday rotation spectra from the experimental results for a single-layer MO film (red line) and the MPC (hollow dots), as well as the calculated results for the MPC (black line) [35].

Increasing the number of high- and low-index bilayers in the Bragg mirrors allows for stronger localization of the light in the defect cavity, leading to higher quality factors and better enhancement of the MO effects. Having more MO defects in the structure is also

expected to result in greater values for the MO effects. However, the increased optical path length in the cavity, especially when MO materials are involved, prohibitively increases the optical losses. Furthermore, the optical and MO responses of the MPCs depend on the parameters such as the material properties, thicknesses, and relative positions of the constituent layers. Therefore, optimization of the configuration and mentioned parameters is necessary for the MPC to accomplish desired MO properties, minimum optical loss, and low power consumption.

We have used finite-difference time-domain (FDTD) calculations to design and optimize an MPC which could enhance FR and perform light modulation with high contrast, simultaneously at three fundamental wavelengths of red, green, and blue (RGB). The FR values of 20º, 55º, and 30º were achieved for RGB wavelengths, respectively [71], as discussed in Chapter 4 of this thesis.

Fabrication and integration of MPCs with optimized optical and MO properties is complicated in practice. Growing a stack of thin films and deposition of MO films on non-garnet sublayers encompasses challenges due to lattice mismatch issues resulting in the creation of defects, cracks, and secondary absorptive phases, which deteriorate the MO properties. Nevertheless, auxiliary methods such as in-situ and post-deposition annealing or using intermediate layers could help realize these structures. Another challenge with the practicality of the MPCs for device applications is the bandwidth limitation arising from the resonant nature of the enhancement. By increasing the quality factor of the cavity in MPC one could achieve a better enhancement of the MO effects, however, the linewidth of the transmission peak would decrease consequently, which limits the operation bandwidth for the system. Hence, broadband applications necessitate nonresonant or multi-resonant schemes.

1.2.2 Magnetoplasmonics

Hybridizing MO materials with plasmonic structures, known as magnetoplasmonics, is the other major approach used for enhancing MO effects [5], [6], [96], [123], [181]–[185].

Exciting surface plasmon resonances (SPRs) in the interface of the MO material with the plasmonic component (typically noble metals e.g. gold or silver) leads to localization of the electric and magnetic fields in the interface, which increases the light-matter interactions and enhances the MO effect in this method. The schematic of a magnetoplasmonic structure is illustrated in Figure 1.7a, where a periodic array of gold nanowires is patterned on an MO thin film deposited on a substrate. Field profiles at cross section of such a structure, when excited by a light beam polarized parallel or perpendicular to the nanowires (denoted as TE and TM polarizations, respectively) are shown in Figure 1.7b,c. In addition to the plasmon resonances, the periodicity of a plasmonic structure could enable the coupling of light to the film underneath and activate slab waveguide modes. Figure 1.7b presents the results for TE polarization, where the electric field of the incident light is parallel to the nanowires. The diffraction with non-zero orders results in total internal reflections in the MO slab, which enhances the field in MO film as displayed. In Figure 1.7c, TM polarization, the incident light has its magnetic field parallel to the nanowires. In this case, besides the waveguide mode, plasmon resonances are also excited in the interface between the gold nanowires and the MO film, as the field distribution suggests [183].

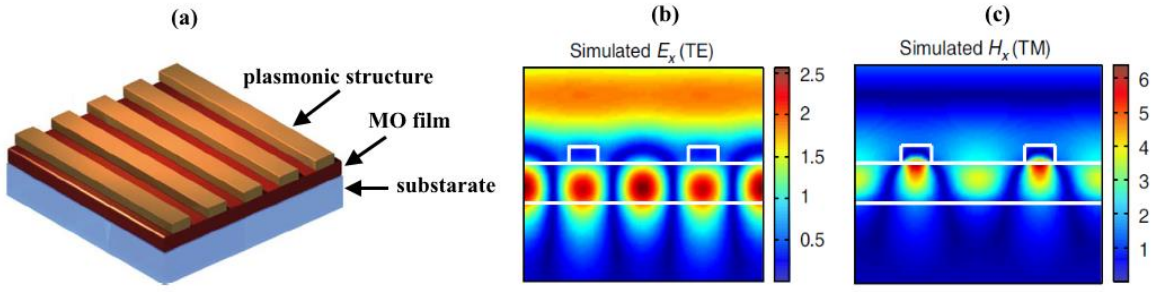

Figure 1. 7. (a) Schematic illustration of a magnetoplasmonic structure composed of gold nanowires patterned on an MO film on a substrate. Cross-sectional field profiles for (b) TE- and (c) TM-polarized incident light. Field amplitudes were calculated by numerical methods and normalized with respect to that of incident light [183].

We have designed a broadband magnetoplasmonic structure capable of remarkable enhancement of the Faraday effect in a broad wavelength range, which enables up to three orders of magnitude enhancement, as described in Chapter 5 of this thesis. By structural optimization of magnetoplasmonic system, we demonstrated rotation angles over 20º in an overall thickness of 15 nm (comprised of 5-nm thick gold nanoantennas on a 10 nm Bi:YIG film).

Magnetoplasmonics does not bear the problems related to the fabrication of multilayer stacks. Besides, the metallic components could also serve as bias contacts or drivelines and facilitate realizing active devices. Nonetheless, the enhancement of EM fields and subsequently MO effects through SPRs only occurs in small subwavelength volumes in the interface with plasmonic structure [186]. Hence, the total enhancement attainable in this method is limited and for thicker films, multiple layers of plasmonic structures are needed to achieve efficient enhancement all over the film [187]. Such a structure suffers from challenging fabrication and low transmission due to the optical losses caused by multiple layers of the metallic arrays. Moreover, the resonant nature and dependence of the enhancement on the plasma resonances of available metals limit the flexibility and narrow the operation wavelength ranges. In addition, fabrication procedure for plasmonic structures could be complex and costly and restrict scalability.

1.2.3 Plasmonic enhancement for sensing applications

Plasmonic enhancement of EM fields and MO effects have been particularly promising for sensing applications. This makes it possible to sense any slight changes in the near-field environment and allows for identifying the surrounding materials by recognizing and amplifying their unique response to an EM wave. Enhanced MO effects increase the signal-to-noise ratio in magnetooptical surface plasmon resonance (MOSPR) sensors and improve the limit of detection (LOD) [188]–[190]. Furthermore, enhancement of both field intensity and optical activity using plasmonics could benefit Raman spectroscopy, which provides information about a sample by the vibrational, rotational, and translational modes of the

molecules. The inherent weakness of the Raman signal limits the sensitivity of this technique and necessitates long testing times and large sample sizes [191], [192]. Exploiting plasmonics in Raman spectroscopy enables enhancement factors up to 10^{14}-10^{15} and eliminates the mentioned drawbacks [193]. Besides, the metallic surface of the plasmonic structures allows for selectivity to specific analytes. Therefore, surface-enhanced Raman Spectroscopy (SERS) and surface-enhanced Raman optical activity (SEROA) empower sensing small concentrations and detecting trace, even to single-molecule or single-cell level. These methods have attracted interest in a variety of fields such as chemistry and reaction monitoring [194], analytical sciences [192], biomedical applications and pharmacy [195]–[198], and forensic sciences [199]. The enhancement factor and wavelength depend on the composition of the surrounding medium and geometry, size, and proximity of the structures [200]. Different plasmonic structures studied for this purpose include colloidal nanoparticles [201]–[207], nanoshells [208], [209], bi-metal nanoparticles [210], [211], encapsulated and functionalized nanoprobes [212]–[218], controlled nanoparticle clusters [219], metal nanoparticles immobilized on solid surfaces [220], films and roughened electrodes [221], and patterned and nanostructured substrates [222]–[225]. The ongoing research in the field focuses on the designing optimized plasmonic structures for a better functionality. In this work, we have designed, fabricated, and tested novel plasmonic structures for SERS purposes.

1.3 Magnetization switching and MOSLM driving systems

This section describes various mechanisms for magnetization switching and their potential for driving active MO devices. A comparison of these methods and how they can be applied in MOSLMs is also discussed.

1.3.1 Thermomagnetic switching

In 1958, thermomagnetic writing on magnetic films was demonstrated by Mayer, using a heated pen [226] and an electron beam [227]. In this process, the thermal source heats the selected spots on a magnetic film up to the Curie temperature (T_C) or any other transformation

temperature capable of making the spots nonmagnetic. Due to the energy minimization considerations originating from thermodynamic rules, when the spots cool down below the transformation temperature, they will be magnetized in the opposite direction. This phenomenon introduces a mechanism for switching the magnetization, which is called thermomagnetic switching.

In the later years, a laser (as the thermal source) with aid of an oppositely directed bias magnetic field was used by Fan et al. [228], [229] for reversing the magnetization of small regions and realized an MO hologram by this method. According to Krumme et al. [230], the local thermomagnetic switching can be explained by nucleation and motion of the domain walls. The nucleation threshold strongly depends on the uniaxial magnetic anisotropy (K_u). In the heated region, the lattice misfit due to the thermal gradient reduces the K_u and can even cause a sign change. Thus, spontaneous switching is possible with small or zero "tipping fields."

Recently, an experimental demonstration of reproducible and field-free magnetization switching was realized by Stanciu et al. [231], using a circularly polarized laser pulse, which involved the thermomagnetic mechanism. A single 40-fs pulse was proven to accomplish the magnetization reversal in an amorphous ferrimagnetic GdFeCo alloy. This laser-induced switching was explained by the cooperation of two phenomena: First, a portion of the pulse energy absorbed by the material rapidly heats the magnetic system to just below T_C and creates a state that is highly nonequilibrium. Second, the inverse Faraday effect according to which, an external oscillating electric field can induce a static magnetization proportional to $\vec{E}(\omega) \times \vec{E}^*(\omega)$. So a circularly polarized light serves as a magnetic field that is parallel to its wavevector. These two effects together make it possible to switch the magnetization by a circularly polarized laser pulse, with no need for external magnetic fields. The subsequent studies [232] confirmed such a non-precessional method for reversing magnetization direction. Figure 1.8 displays the progression of magnetization switching in this method. The images depict the magnetic domains with initial upward (white) or downward (black) magnetization in a $Gd_{24}Fe_{66.5}Co_{9.5}$ sample, after being excited by 100-fs RHCP (σ^+) or LHCP

(σ^-) laser pulses. In the first few hundreds of femtoseconds, the absorption of the laser pulse, regardless of its helicity, leads the material with an initial magnetization to a nonequilibrium state with no determinate net magnetization. In the subsequent few tens of picoseconds, depending on the helicity of the pump laser with respect to the initial magnetization of the system, the material either relaxes to its initial state or a tiny domain with a magnetization in opposite direction is generated.

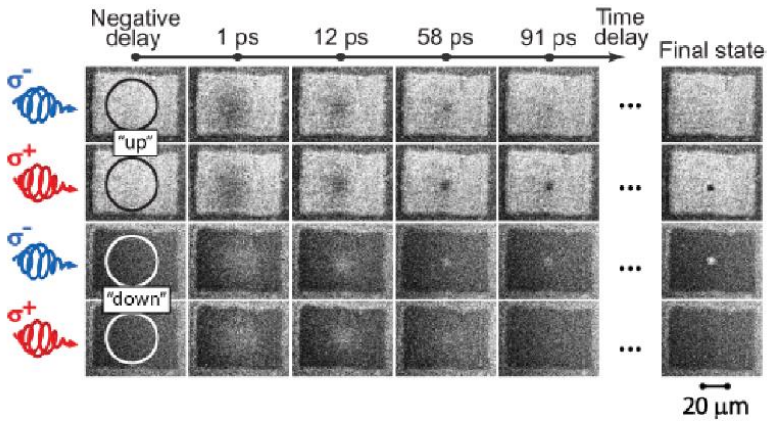

Figure 1. 8. Thermomagnetic switching by circularly polarized laser pulses, via a nonequilibrium state. The images show the magnetic domains in a $Gd_{24}Fe_{66.5}Co_{9.5}$ sample with initial upward (white) or downward (black) magnetization, after excitation by 100-fs right- (σ^+) or left-handed (σ^-) circularly polarized laser pulses. The circles show the regions affected by the pump pulses [232].

Thermomagnetic switching was applied in the first MOSLM [89], which comprised two transparent electrodes sandwiching a garnet film and a Cu-doped CdS photoconductor. A HeNe laser with 1 μW power, a sinusoidal magnetic field of 100 Oe, and an electric field of 1.2×10^4 $V\cdot cm^{-1}$ were used for switching in this so-called magnetooptic photoconductor sandwich (MOPS). The switching mechanism involved three main stages: (i) absorption of the laser light by the photoconductor, which generates conduction electrons in the illuminated regions, (ii) creation of Ohmic heat in the mentioned regions by applying an electric field through the electrodes, which acts as the thermal source required for thermomagnetic writing,

and (iii) exploiting an external magnetic bias as the tipping field for changing the magnetization orientation.

In 2014, Takagi et al. [233] fabricated an MOSLM with submicron pixels for 3D imaging and wide-viewing-angle holographic displays. The pixel array was thermomagnetically written on an amorphous TbFe film as shown in Figure 1.9, using 10-ns pulses of a 532-nm laser. In a following study [234], localization of light through an MPC structure was suggested to decrease the energy requirement of the laser for switching, and a 59% reduction in comparison to a single layer magnetic film was reported.

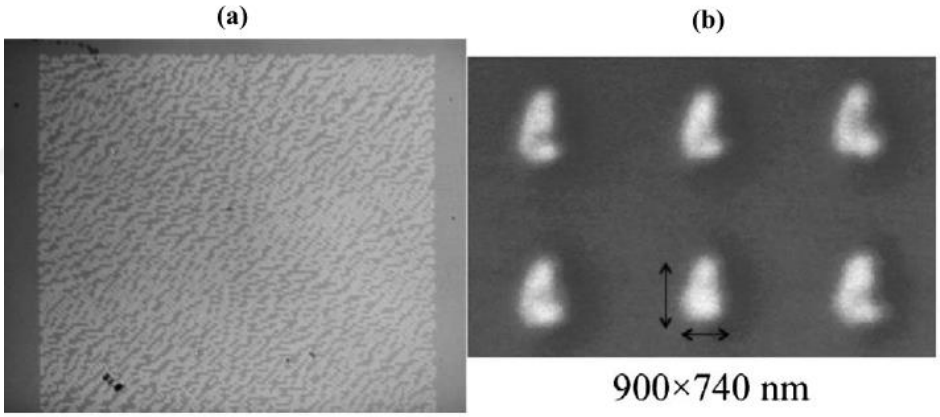

Figure 1. 9. Submicron MOSLM pixel array written on an amorphous TbFe film with 10-ns pulses of a 532-nm laser. (a) Polarization microscope image of 256×256 pixels with 1 μm pitch and (b) magnetic force microscopy image of 3×2 pixels with 2.5 μm pitch [233].

1.3.2 Nonthermal all-optical switching

The laser-induced magnetization reversal schemes discussed above were majorly based on the thermal effect of a laser pulse, where the polarization is not determinant. The disadvantage of this method is the low switching rate, as the reiteration frequency is limited by slowness of the cooling rates. However, ultrafast laser pulses can also switch the magnetization by nonthermal effects, which are instantaneous and the speed limit in this case,

is only related to the pulse width. In contrast to the thermal-induced switching, the polarization of the pump laser has an important role in nonthermal optical switching. The nonthermal effects of an optical pulse can be discerned as photomagnetic and optomagnetic effects. In photomagnetic effects, photons are absorbed and effectively excite the magnetic system. In optomagnetic effects, photon absorption is not necessary and a coherent Raman-like optical scattering is involved. Indeed, optomagnetic effects can be explained as the inverse of magnetooptical effects [235]–[237], which could substantially enhance through magnetophotonic microcavities [238].

Kimel et al. [237] indicated that based on the inverse MO effects, a 200-fs circularly polarized laser pulse can serve as a magnetic field pulse as large as 5 T. The feasibility of nonthermal all-optical control over spin oscillations in $DyFeO_3$ was experimentally demonstrated by them. The following research by Hansteen et al. [239] signified that both linearly and circularly polarized light are capable of nonthermal photomagnetic effects, which could change the magnetocrystalline magnetic anisotropy and create a new magnetization equilibrium. Such a long-lasting change in the magnetocrystalline anisotropy stems from optical transfer of electrons between ions on nonequivalent lattice sites and consequently, redistributed ions in the crystal lattice. When a circularly polarized light is applied, the inverse Faraday effect along with the described effect results in a strong transient magnetic field in the direction of propagation. These two effects together bring about an all-optical magnetization switching through nonthermal effects. Hansteen et al. attained 0.6º rotation in magnetization orientation using a 100-fs laser pulse, though production of shorter laser pulses paves the way for achieving full switching.

In the recent years, Stupakiewicz et al. [240] demonstrated an ultrafast photomagnetic switching of magnetization in Co-substituted yttrium iron garnet (Co:YIG), using a 50-fs linearly polarized laser pulse. By adjusting the polarization direction of the pump pulse, they could reversibly steer the magnetization between two distinct states, which enables magnetic writing and erasing. As shown in Figure 1.10a, the initial magnetic structure consisted of small labyrinth-like domains (black spots) inside larger background domains (white regions).

Substitution of Fe^{3+} ions in YIG with dopant ions of Co^{2+} and Co^{3+} creates strong magnetocrystalline and photoinduced magnetic anisotropy. Indeed, pumping Co:YIG with laser pulses leads to d-d transitions in cobalt ions and induces a magnetic anisotropy, which lifts the degeneracy between two metastable magnetic states in Co:YIG (Black and white domains). Therefore, when the initial state of the material is excited by a single [100]-polarized pulse, the large white domains turn into black and simultaneously, small black domains turn into white (Figure 1.10b). A laser pulse perpendicular to the first pulse, [010] polarization, recovers the initial state (Figure 1.10c).

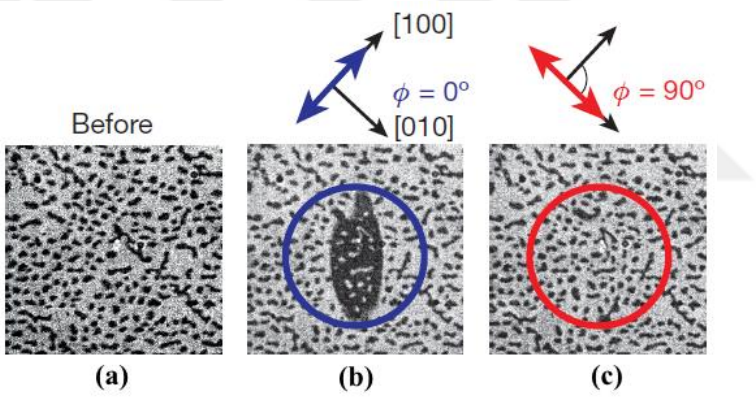

Figure 1. 10. Nonthermal reversible magnetization switching (magnetic writing and erasing) by 50-nm laser pulses with linear polarization. ϕ is the angle between the pump pulse polarization and the [100] axis. The 200 μm × 200 μm images are taken by a femtosecond magnetooptical imaging technique. (a) Initial domain structure before laser excitation, which was set by applying an external magnetic field $\mu_0 H$ = 80 mT along the $[1\bar{1}0]$ axis for a few seconds. (b) Domain structure after excitation by a single laser pulse polarized along the [100] axis, and (c) subsequent excitation with a similar laser pulse polarized along the [010] axis [240].

Stupakiewicz et al. also investigated how the pump fluence affects the switched area (Figure 1.11). The minimum pump fluence necessary for magnetic recording in Co:YIG was strongly affected by the wavelength, as depicted by the black and blue data points. The magneto-optical images of the material pumped by different fluences are displayed on top of

the figure. The inset graph shows how the switched area depends on the wavelength in range of 1150-1450 nm (1.08-0.86 eV), for a pump fluence of 83 mJ·cm^{-2}. A resonance is observed around 1305 nm (0.95 eV) due to the resonant excitation of electronic d-d transitions in Co ions.

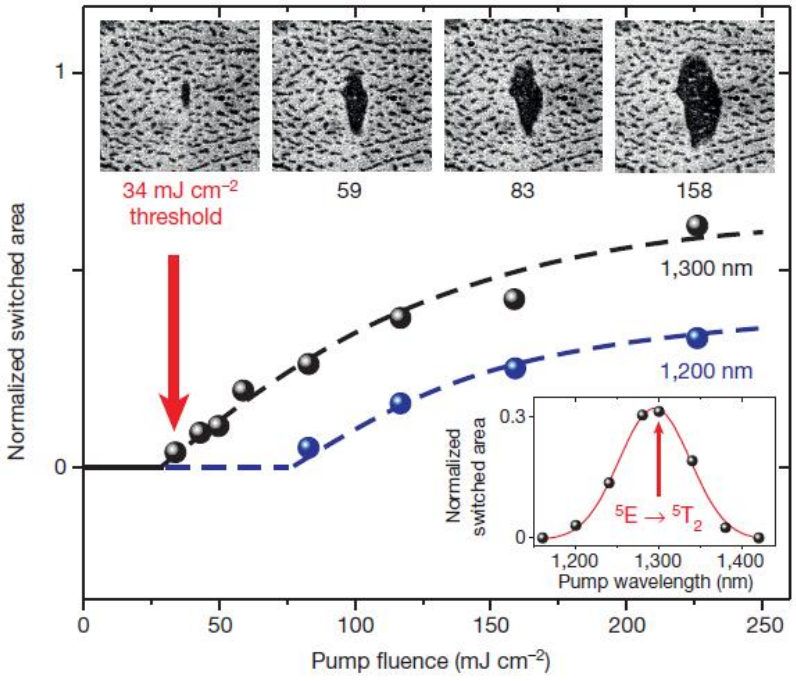

Figure 1. 11. Dependence of the nonthermal all-optical magnetization reversal on the laser influence. The images display the switched areas on a magnetized Co:YIG sample after pumping by different laser fluences. The blue and black data points guided by dashed lines show the normalized switched area as a function of the pump fluence, for the lasers with central wavelengths of 1200 and 1300 nm, respectively. The normalized switched area was calculated as the ratio of the switched domain area (the black large domain on the images) to the area of pump laser spot πr^2 (r: the pump spot radius). The inset depicts the spectral dependence of the normalized switched area for a pump fluence of 83 mJ·cm^{-2} [240].

Finally, Stupakiewicz et al. investigated the time dependence of the nonthermal all-optical magnetization switching via time-resolved MO imaging with captures at different

time delays between the pump and probe pulses (Δt). The results (Figure 1.12) showed the formation of a switched domain within a characteristic time, τ, about 20 ps and stabilization of the domain after approximately 60 ps. The hollow dots fitted by the red line represent the projection of the magnetization on [001] axis (normalized to the saturation magnetization), M_z, as a function of Δt. The lower inset schematically illustrates the magnetization trajectory between the two states.

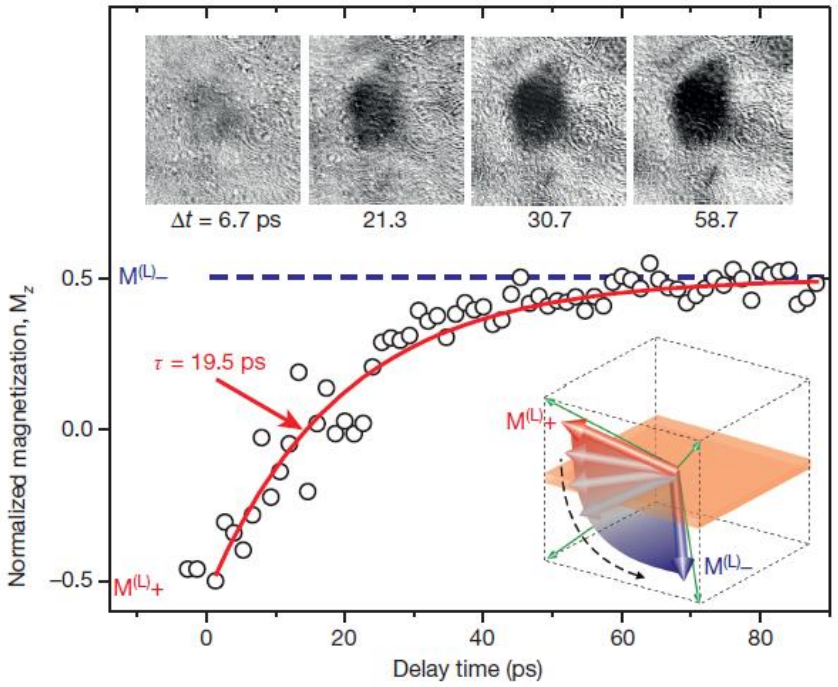

Figure 1. 12. Time dependence of nonthermal all-optical magnetization switching. The time-resolved femtosecond single-shot magnetooptical images are captured at different time delays between pump and probe pulses. The magnetization projection on the [001] axis (M_z) normalized with respect to the saturation magnetization was plotted as a function of the time delay by the hollow dots. The data points were calculated as the ratio of the magnetooptical signal (the average image contrast) in the switched area to the magnetooptical signal in the case when the magnetization is aligned along the [001] axis. The red solid line was fitted using the exponential increase $(1 - \exp[-\Delta t/\tau])$ with the characteristic time $\tau = 19.5 \pm 1.6$ ps. The lower inset shows the schematics of the magnetization trajectory during the switching. The magnetization is

switched between $M^{(L)+}$ and $M^{(L)-}$ states, representing the magnetization states corresponding to the large background domains observed in white and black colors, respectively. A laser pulse polarized along the [100] axis with fluence of 150 $mJ \cdot cm^{-2}$ and central wavelength of 1250 nm was used for switching [240].

In contrast to laser-induced switching of magnetization in metals, which essentially occurs through the thermomagnetic effects as explained in subsection 1.3.1, the all-optical switching in transparent dielectrics does not impose the heating of the material up to T_C to re-establish magnetic state.

1.3.3 Current-induced Oersted field switching

In 1983, a fast, nonvolatile, cost-effective SLM was introduced, named as LIGHT-MOD (Litton iron garnet H-triggered magneto-optic device) [33]. The device was composed of Bi-substituted iron garnet pixels on a nonmagnetic substrate (Figure 1.13a), which were addressed electrically using a crossbar array of conducting drivelines. Indeed, the Oersted field created by flowing current in the drivelines was responsible for switching magnetization of the pixels. The conductor drivelines with an XY matrix pattern separated by an insulator layer were fabricated on the pixels. To realize the switching in a certain pixel, current was applied to the the row and column drivelines that intersect at the desired pixel. To prevent switching the whole pixels of a row or column, the current magnitude in one driveline was designated to be insufficient to generate the magnetic field necessary for the magnetization reversal. Only the combined magnetic fields from both of the current lines on a pixel were capable of switching it. The position of the drivelines with respect to pixels and the switching procedure is schematically illustrated in Figure 1.13b. The magnetization switching was described as a two-step process: (i) nucleation of a domain with reversed magnetization in the corner where the drivelines intersection and (ii) spread of the domain towards the other corners of the pixel to complete the switching.

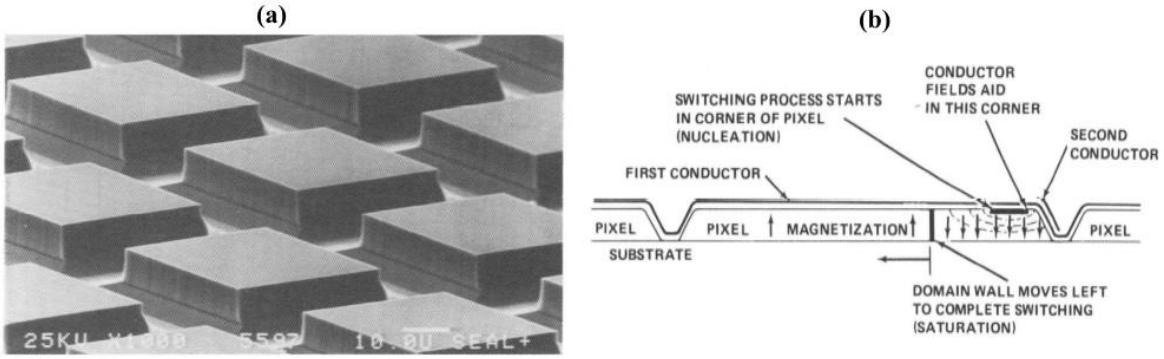

Figure 1. 13. Litton iron garnet H-triggered magneto-optic device (LIGHT-MOD), which was an MOSLM exploiting current-induced Oersted field switching. (a) SEM image of the pixelate MO film and (b) schematic illustration of the conducting drivelines on a pixel and the switching procedure [33].

Taking advantage of the electrical addressing method, LIGHT-MOD was a stable and programmable device that was applied in various optical processing systems [241]. However, the relatively large current requirement for switching the pixels [72] was a challenge on the way of its predominant commercialization. The research in the following years focused on lowering the current demand of this MOSLM by altering the material, shape, size, and position of the drivelines [34], [58], [72], the fabrication of pixels [37], [38], [58], [91], and the timing of the driving scheme [242]. As a result, a reduction of the driveline current from over 100 mA to below 10 mA was reported. Figure 1.14 presents a current-driven MOSLM that functions in reflection mode and could generate a homogeneous magnetic field all over the pixels due to the arrangement of its drivelines. The conductors resemble a small coil on top of each pixel which allows for low-power magnetization switching.

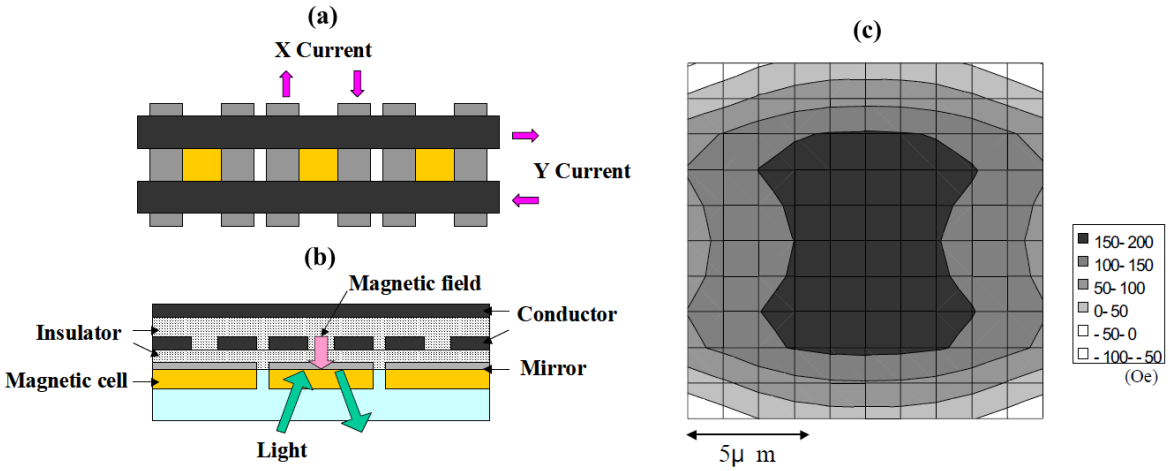

Figure 1. 14. A low-power current-driven MOSLM, which works in reflection mode and the design of its drivelines allows for generating a rather homogeneous magnetic field over the pixels. Schematic (a) top and (b) side views. (c) Field distribution over a pixel [58].

1.3.4 Spin torque switching

Spin torques present a novel current-based approach for switching the magnetization, which has the potential to be applied in MOSLMs. In contrast to the Oersted field switching described in the previous subsection, no external magnetic field is involved in this switching mechanism. Thus, the crosstalk problem due to stray fields, which is substantial for the small pixel pitches, is not a concern in this method. Furthermore, a complex XY-matrix driveline system is not required in this approach and sub-nanosecond switching speed is possible. More importantly, the current requirement is orders of magnitude smaller than the methods based on the Oersted-field [59], [243]–[245]. Taking into account the involved phenomena, two types of spin torques have been studied for magnetization switching:

Spin-transfer torque (STT)

One mechanism for spin-torque switching is called spin-transfer torque (STT), that is, when the current passing through a multilayer becomes spin-polarized and transfers spin angular

momentum from one magnetic layer to another. As the giant magnetoresistance (GMR) in multilayer stacks [246], where flow of current is highly impacted by the magnetic moment alignment in the layers, the inverse effect could also be expected. So the electrons scattering in a magnetic multilayer can influence the magnetic moments by imposing torque and transfer of angular momentum between the layers. STT has been demonstrated in different multilayer stacks [247]–[251] and has proven to be compatible with MO devices [59], [81], [252], [253]. The cross-section view of a pixel in an STT-switching MOSLM is schematically shown in Figure 1.15. The pixel is composed of a transparent top electrode, two magnetic layers that are separated by a non-magnetic spacer, and a bottom electrode. The spacer can be metal (in spin valves) or insulator (in magnetic tunnel junctions) [254].

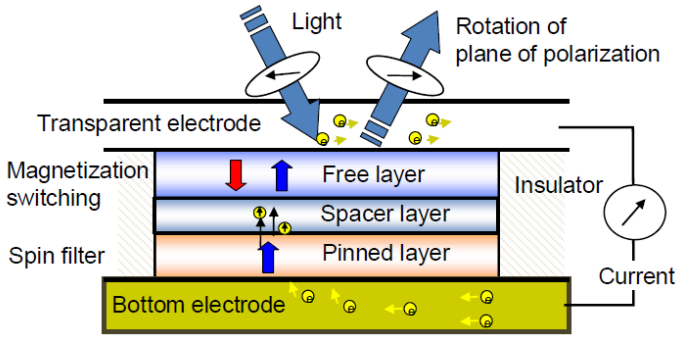

Figure 1. 15. Schematic cross-section of a pixel in a MOSLM based on spin-transfer torque (STT) switching [81].

In one of the magnetic layers, the magnetization could be easily tuned by weak magnetic fields (named as free layer), while the other layer requires a large magnetic field to switch the (named as pinned layer). A current flow applied perpendicular to the stack, gains spin polarization by passing through the pinned layer. Transfer of angular momentum from the spin-polarized current to the free layer can alter its magnetization direction. If an MO material is used as the free layer, the system can be used for MO modulation of light.

Current densities that are typically sufficient for switching the magnetization in this approach are on the order of 10^7 A·cm^{-2} [254].

Spin-orbit torque (SOT)

The other mechanism for magnetization switching via spin torques is called spin-orbit torque (SOT), which involves spin Hall [243], Rashba [255], [256], or Dresselhaus [256] effect. In this mechanism, the coupling between spin and orbital motion of electrons generates a non-equilibrium spin accumulation, which subsequently affects the magnetization state by applying torque. The spin-orbit (SO) coupling states that the electrons moving under an electric field experience a magnetic field (SO field) that couples to their magnetic moment [257].

According to the spin Hall effect (SHE) [258], in the flow of a charge current, due to the SO coupling, electrons with opposite spins deflect in opposite directions that are perpendicular to the initial flow direction, as illustrated in Figure 1.16. Thus, the charge current of unpolarized spin translates to a spin current in the crosswise direction. The equal number of electrons with up and down spins in an unpolarized current prevents flow of a net charge current at this direction. The spin current creates a spin accumulation that can be utilized for reversing the magnetization in a neighboring layer through the spin torque, as described before.

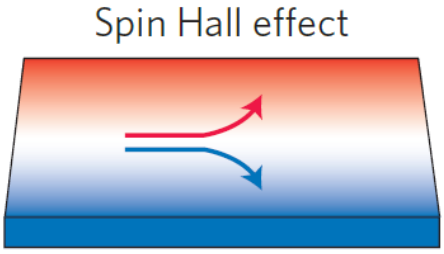

Figure 1. 16. Schematic concept of Spin Hall Effect (SHE) where an unpolarized charge current converts to a pure spin current transverse to the initial current path [257].

According to the Rashba effect, in a stack comprised of a ferromagnetic material between two dissimilar layers, a highly asymmetric electric potential forms perpendicular to the films plane, which gives rise to a structural inversion asymmetry (SIA) in the mentioned direction. The electrons that move in such a structure, face a net electric field E which is transformable into an effective magnetic field, H_R, by the SO interaction:

$$H_R = \alpha_R (\hat{z} \times \langle k \rangle) \quad (1.4)$$

where α_R is a material factor showing the strength of the SO coupling, $\hat{z}$ is the unit vector parallel to E, and $\langle k \rangle$ is the average wavevector of the electrons. In absence of charge current, k and −k states have equal populations and $\langle k \rangle = 0$, however, when current is applied, the electrons distribute asymmetrically in k-space. Thus, a net effective field and subsequently, a nonequilibrium accumulation of spin is generated at a right angle with respect to the current flow. The accumulated spin density can induce a magnetization switching by applying a spin-transfer torque as discussed above [259], [260].

In a similar situation, if the E field leading to the effective magnetic field responsible for the spin accumulation and spin-torque switching, originates from a bulk inversion asymmetry (BIA), the phenomenon is named Dresselhaus effect [256]. The zinc blende structure with no inversion center shows Dresselhaus effect.

SOT is typically observed in heterostructures consisted of a ferromagnetic film which is placed between an insulator and a heavy metal that has strong SO coupling [261], [262]. Creation of the Rashba field from a charge current in such a heterostructures is depicted in Figure 1.17. This mechanism has been widely deliberated and developed for spintronic devices [263], [264], [273], [274], [265]–[272].

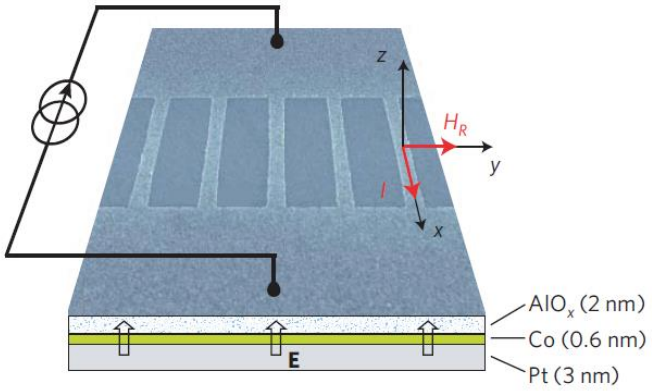

Figure 1. 17. Rashba field produced by a charge current, in typical heterostructures exhibiting spin-orbit torques (SOT). E shows the net electric field originating from the asymmetric electric potential in the direction with structural inversion asymmetry (SIA). Because of spin-orbit interactions, in the presence of a charge current (I), the E field transforms into an effective magnetic field H_R and induces a nonequilibrium spin density perpendicular to both I and E. The spin accumulation exerts a torque on the magnetic moment of the material and provokes magnetization reversal [259].

In summary, SOT uses an in-plane current for flipping the magnetization of the free layer and unlike SST, does not oblige passing a current through the tunnel junction. Therefore, SOT enables a faster magnetization switching and reduces the required current densities down to 10^5 A·cm^{-2} [275], [276].

1.3.5 Multiferroic switching

Despite the above-mentioned efforts for improving the current-bases magnetization switching methods, the required current densities (typically in the range of 10^5-10^7 A·cm^{-2}) are not satisfactory for reliable device operation and commercially acceptable energy consumption. The current-based methods inevitably involve Joule heating and consequently, thermal drift and operational errors, especially when applied in miniature devices. These conditions have motivated the search for switching schemes with lower power consumption.

Multiferroics offers another electrical method for magnetization switching, based on the electric field and voltage control. According to the early experimental demonstrations, this

method could decrease the energy dissipation per unit area per switch to 1-500 $\mu J.cm^{-2}$, compared to the current-based methods (1-10 $mJ.cm^{-2}$) by eliminating the resistive losses [277]. Multiferroic compounds denote systems with several ferroic orders. One example of theses dual orders is the coupling of ferromagnetics and ferroelectrics, which is called the magnetoelectric effect. Practically, magnetic devices entail electrical control of magnetization, which indicates the importance of magnetoelectric effect in device applications. Multiferroic systems capable of demonstrating the magnetoelectric effect can be classified into two types: First, single-phase multiferroic materials in which the magnetoelectric coupling allows for modification of the magnetic properties by applying an electric field. Second, composite structures in which, a ferroelectric (or piezoelectric) material is combined with a ferromagnetic (or magnetostrictive) material. Intuitively, the magnetoelectric coupling in the composite systems occurs through one of the following means [77]:

- Strain coupling: modifying the magnetic properties by the inverse magnetostrictive (named as magnetoelastic) effect, which is controlled by the voltage-induced strain from a piezoelectric material [90], [278].
- Influence of the electric polarization of a ferroelectric component on the electronic structure and magnetic properties of a neighboring ferromagnet, in the interface [279].
- Utilizing the exchange interactions between a ferromagnetic and a (magnetic) ferroelectric materials [280].

A multiferroic MOSLM by voltage control, which takes advantage of a piezoelectric material, PZT with the chemical composition of $PbZr_{0.52}Ti_{0.48}O_3$, for magnetoelectric coupling [90] is schematically depicted in Figure 1.18. Application of voltage over the drivelines of a pixel that has out-of-plane magnetization, creates a stress on the selected pixel due to the presence of the electrostrictive PZT film. Because of the magnetoelastic effect, such stress serves as an effective magnetic field and aligns the magnetization of the domains to the in-plane direction. At this step, a small external magnetic field in the direction opposite

to the initial magnetization could result in the switching of the selected pixel to the new state, which can be retained even after turning off the voltage.

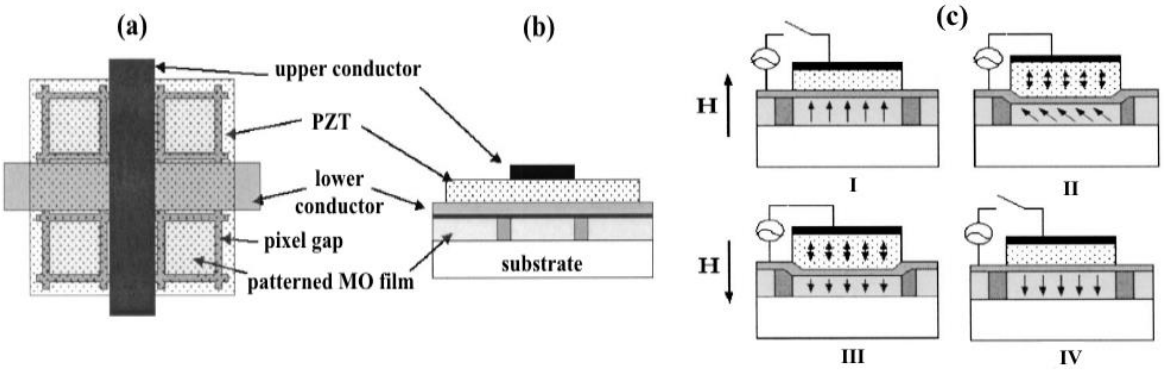

Figure 1. 18. Schematic (a) top view and (b) cross section of a pixel in a multiferroic voltage-driven MOSLM that uses magnetoelectric effect through strain coupling for switching. Top view represents 3×3 pixels and conductor lines are shown only on the central pixel for clarity. Pixels are comprised of a PZT layer on top of the MO garnet film. (c) Switching procedure: I) A pixel with out-of-plane magnetization. II) By applying a voltage through the crossbar metallic contacts, a stress is generated by the electrostrictive PZT layer on the selected pixel. This stress acts as an effective magnetic field which helps the magnetized domains to realign to the film plane due to the magnetoelastic effect. III) In this stage, a small magnetic field in the opposite direction to the initial magnetization causes the selected pixel to easily switch. IV) The pixel retains the new magnetic state even after turning off the voltage [90].

The resistive losses are minimized in magnetoelectric or voltage-driven switching, which uses an electric field for modifying the magnetic properties as a mechanism to realize magnetization reversal. This method only needs an electrical resource for charge and discharge of a capacitor. Thus, its energy consumption is two orders of magnitude smaller than the current-driven approaches [281], which make it a preferable for MOSLM driving. Experimental reports suggest that this mechanism operates by modifying the magnetic anisotropy [118], [278], [279], [282]–[285], altering the magnetic state of the material [286]–[288], or coupling the ferroelectric and magnetic orders [289], [290]. In Figure 1.19 various

magnetic features are presented, which could be manipulated by an electric field [77]. These properties can affect the magnetization orientation and thus, offer prospective methods for low-power switching of magnetization.

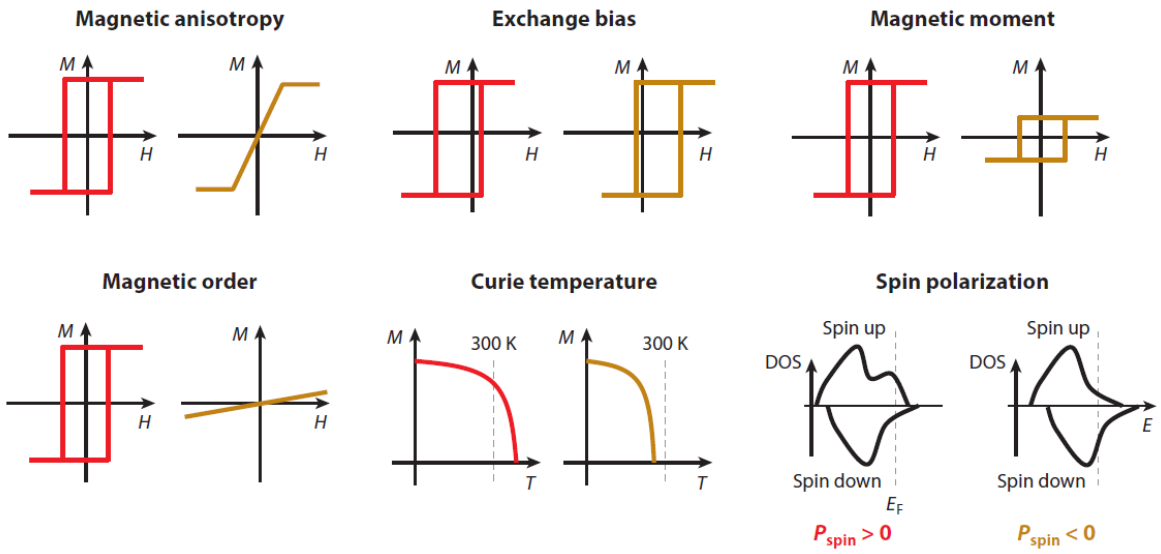

Figure 1. 19. Magnetic properties that can be controlled by an electric field and therefore, can be considered as potential mechanisms for low-power magnetization switching (DOS: density of states) [77].

In summary, different methods for switching magnetization in magnetic and MO devices were reviewed in this section, with their advantages and disadvantages. The thermomagnetic switching does not involve complicated mechanisms and can be realized with any heat source. However, power consumption is prohibitively high in this method. Control over the heated area is not simple and consequently, switching errors and instability problems related to thermal drift cannot be avoided. Moreover, being limited to the cooling rates, the switching rate is slow in this method. Nonthermal all-optical switching offers high speed but necessitates ultrashort and intense laser pulses, which are accompanied by safety and cost-efficiency concerns. Furthermore, heating due to the absorption of photons might be inevitable in this approach, which can cause temperature rise and attenuation problems,

complication of the involved phenomena, and fragile control over the process. Current-induced Oersted field switching introduces an electrical addressing method that enables programmable stable devices. Nonetheless, this method requires a rather complex driveline system, demands high current densities for generating large enough magnetic fields to switch the magnetization, and suffers from the Joule heating caused by current flow in long and narrow conductors, especially in miniature devices. So the current density and power consumption in this method exceed the acceptable values for commercial development and widespread use. Spin torques enable another current-based method for magnetization switching, which does not involve generation of external magnetic fields and thus, eliminates the crosstalk problems caused by stray fields. A crossbar driveline system is not required in this method and the current requirement is orders of magnitude smaller in comparison to the Oersted field approach. However, Joule heating is still a problem in this method. The device structures are comprised of multilayer stacks, which are challenging to fabricate. Moreover, this method has only been demonstrated for magnetization switching in very thin (nanometer scale) films, which cannot fulfill the requirements of many practical devices. Finally, multiferroics enable a voltage-induced mechanism for magnetization switching, which appears to be a more viable driving system for industrialization of the MOSLMs since it provides an electrical device control with no significant Ohmic losses and thermal drift. The challenge of this method is the necessity of materials and structures with simultaneous high MO quality and strong magnetoelectric effect, and ongoing research focuses on the design and fabrication of novel systems for this purpose.

1.4 Overview and contribution of the thesis

Magnetooptical spatial light modulators (MOSLMs) hold promise for simultaneous provision of fast modulation speed and fine spatial resolution. The main issue that has impeded the development of MOSLMs as practical devices and mature products is the inherent weakness of the MO effects, which limits the modulation depth and pixel contrast in MOSLMs. This thesis addresses the challenges related to MOSLMs from a materials

engineering point of view besides device design to takes a step forward in realizing nonvolatile, ultrafast, high-contrast, and high-resolution modulation of light.

A comprehensive literature review on the development of MOSLMs at different fronts is presented in Chapter 1. The recent progress in materials processing and fabrication methods in addition to the magnetization switching mechanisms is evaluated for the potential application in MOSLMs.

Chapter 2 focuses on the materials and methods used in this thesis for fabrication, characterization, and modeling of MO devices. The experimental procedures for pulsed laser deposition (PLD) of MO thin films along with the structural and optical characterization of the grown films are described in detail. Furthermore, the theoretical background and finite-difference time-domain modeling of the photonic and magnetooptic phenomena involved in MOSLM design are explained in this chapter.

Growth of Bi:YIG thin films with the chemical composition of $Bi_1Y_2Fe_5O_{12}$ as an MO material with a superior figure of merit for MOSLMs is deliberated in Chapter 3. The films grown by PLD on different garnet and non-garnet substrates under various growth conditions are studied. The effects of the substrate, growth temperature, oxygen pressure in the deposition chamber, and repetition rate of the laser pulse on the crystalline structure and phase composition, surface quality, and optical properties of the films are investigated.

In chapter 4, magnetophotonic crystals (MPCs) with different structures are studied for efficient enhancement of the MO Faraday effect to realize practical MOSLMs. The Faraday rotation, optical loss, and MO figure of merit are calculated as a function of MPC structure. After optimization of the configuration and layer thicknesses, a novel three-defect MPC enabling simultaneous MO enhancement at fundamental wavelengths of red, green, and blue (RGB) and accordingly, capable of RGB modulation within a pixel, is demonstrated.

In order to address the limitations related to the narrow operation band caused by the resonant nature of MO enhancement approaches, a broadband magnetoplasmonic metasurface is introduced in Chapter 5. The effect of geometric and excitation parameters on the optical and MO response of the metasurface is investigated and application-oriented

design guidelines are presented. Moreover, the performance of plasmonic metasurfaces in sensing applications is discussed and different metasurfaces are modeled, fabricated, and tested for surface-enhance Raman spectroscopy (SERS).

Finally, a conclusion is given in Chapter 6 and the perspectives for MO devices are appraised. Future research opportunities are discussed to guide the field towards a new generation of practical integrated MOSLMs.

The research for this thesis has led to the publication of the following articles:

- **S. Kharratian**, H. Urey, M. C. Onbaşlı, "Broadband Enhancement of Faraday Effect Using Magnetoplasmonic Metasurfaces", *Plasmonics* (2020). https://doi.org/10.1007/s11468-020-01304-6
- **S. Kharratian**, H. Urey, M. C. Onbaşlı, "Advanced Materials and Device Architectures for Magnetooptical Spatial Light Modulators", *Advanced Optical Materials 8*, 1901381 (2020).
- **S. Kharratian**, H. Urey, M. C. Onbaşlı, "RGB Magnetophotonic Crystals for High-contrast Magnetooptical Spatial Light Modulators", *Scientific Reports 9*, 644 (2019).
- A. V. Singh, T. Jahnke, S. Wang, Y. Xiao, Y. Alapan, **S. Kharratian**, M. C. Onbaşlı, K. Kozielski, H. David, G. Richter, J. Bill, P. Laux, A. Luch, M. Sitti, "Anisotropic Gold Nanostructures: Optimization via in Silico Modeling for Hyperthermia", *ACS Applied Nano Materials 1*, 6205 (2018).
- A. V. Singh, Y. Alapan, T. Jahnke, P. Laux, A. Luch, A. Aghakhani, **S. Kharratian**, M. C. Onbasli, J. Bill, M. Sitti, "Seed-mediated synthesis of plasmonic gold nanoribbons using cancer cells for hyperthermia applications", *Journal of Materials Chemistry B 6***,** 7573 (2018).

Chapter 2

MATERIALS AND METHODS

In this chapter, the materials and methods used for fabrication, characterization, and modeling of thin films and devices studied in this thesis are described.

2.1 Fabrication

The magnetooptical thin films in this study were grown by a pulsed laser deposition method. Maskless photolithography using a direct laser writer was employed for the fabrication of plasmonic structures. These methods are further elucidated below:

2.1.1 Pulsed laser deposition

Pulsed laser deposition (PLD) is a physical vapor deposition (PVD) technique that combines the advantages of evaporation and sputtering methods. PLD uses high-power pulses of a focused laser beam to vaporize the material from a target and deposit it as a thin film on the provided substrate. The target is a bulk material, generally in a disc shape. The laser pulse striking the surface of the target is absorbed, resulting in electronic excitation, which is then converted into thermal, chemical, and mechanical energy that lead to evaporation. The ejected high-energy species including atoms, molecules, electrons, ions, clusters, particulates, and molten globules, expand into the surrounding and develop a plasma plume. The ablated particles can get condensed when they collide with the substrate and grow a film on its surface. The deposition takes place in a chamber with a controlled atmosphere, which could be ultra-high vacuum or background gases such as oxygen, argon, nitrogen. Growth parameters such as target material, laser energy and pulse repetition rate, temperature and roughness of the substrate, type and pressure of background gases in the chamber, and the

distance between the target and substrate determine the deposition rate, stoichiometry and quality of the deposited film [154], [291], [292].

PLD enables high-quality epitaxial growth of complex oxide thin films with superior control of stoichiometry and thickness. The functionalities of complex oxides are very sensitive to ionic ratios (Re:Fe ratio in $Re_3Fe_5O_{12}$ garnets). Imperfect efficiency of the surface reactions (due to kinetic or even thermodynamic limitations) holds chemical vapor deposition (CDV) or simple evaporation methods from reproducible growth of desired material phases on a sufficiently large area. PLD simply transfers a preexisting material plume and allows for deposition of the desired single-phase complex oxides by avoiding the surface reactions. Decent stoichiometry transfer from the target to deposited film, the possibility of growing composites and compositional gradients from different targets, the feasibility of deposition from various target materials including nearly all the elements of the periodic table by proper choice of the laser energy, flexibility of the system due to decoupling of laser source from the chamber, and the possibility of doping and oxygenation during the deposition are the advantages associated with PLD, which make it an attractive deposition method especially for complex oxide thin films. In comparison to other epitaxial methods such as molecular beam epitaxy, PLD has a simpler system and is more cost-effective. PLD-grown thin films have found applications in functional piezoelectric, magnetic, ferroelectric, magnetoelectric, thermoelectric, and many other advanced devices [154], [291].

A Solmates (SMP 800) customized PLD system, schematically illustrated in Figure 2.1, was used for preparing the thin films studied in this thesis. The system is equipped with a KrF excimer laser with a UV wavelength of 248 nm and pulse duration in the order of 25 ns. A beam delivery module (BDM) comprised of highly reflective mirrors guide the laser beam to the optical scanning stage (OSS) from where it was directed towards the reaction chamber. The OSS is comprised of optical components including a wedge and a lens focusing the laser beam on the target. The movement of OSS enables rastering the beam on the radius of the target disc, from edge to a turning point (TP). Choosing a proper TP along with the rotation of the target stage allows for scanning the whole surface of the target to ensure uniform

consumption of the target and preserve the stoichiometry. The laser entrance window (LEW) which is an interface between the beam delivery unit and the reaction chamber, needs to be cleaned, in order to prevent the deterioration of the laser energy by a residue layer from the previous depositions. A wafer holder is positioned centrally above the target in the vacuum chamber, where the substrate is located facing the target. The substrate is also rotated during deposition to achieve a uniform film with low surface roughness all over the substrate. The IR lamps over the substrate allow for heating it to a desired temperature which is controlled by thermocouples.

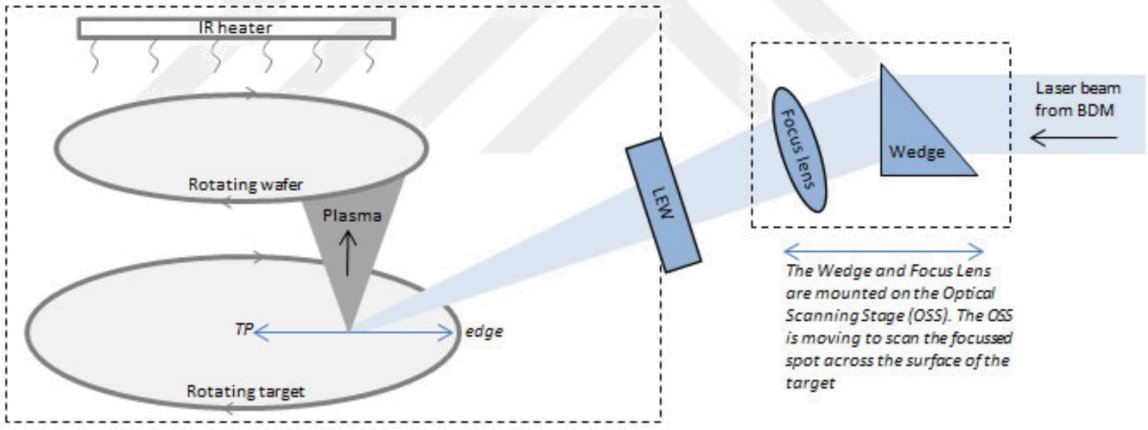

Figure 2. 1. Schematic illustration of the pulsed laser deposition system (BDM: beam delivery module, OSS: optical scanning stage, LEW: laser entrance window, TP: turning point).

A 99.9% pure $Bi_1Y_2Fe_5O_{12}$ disc with 2″ diameter and 0.125″ thickness provided by Advanced Engineering Materials was used as the PLD target for growing the magnetooptical thin films in this study. In each deposition run, different chips were simultaneously placed in the deposition chamber as substrates:

- GGG: gadolinium gallium garnet ($Gd_3Ga_5O_{12}$), with (111) cut
- SGGG: substituted gadolinium gallium garnet ($Gd_{2.6}Ca_{0.4}Ga_{4.1}Mg_{0.25}Zr_{0.65}O_{12}$), with (111) cut

- quartz (SiO_2), with (0001) cut.

All the substrates were two-side polished single-crystalline chips provided by the MTI Corporation. The chips were in square-shape with 5×5 mm^2 size and 0.5 mm thickness. In order to adapt the chips to the wafer holder of the PLD system, a chip holder made of Si wafer was used.

2.1.2 Maskless photolithography

Photolithography is a technique for patterning structure on substrates using a photo-sensitive resist. In common mask-based photolithography, the pattern is imaged to the photoresist using a mask. The difficulty, time, and expenses associated with the production and repair of masks in addition to the complexity and lack of flexibility in this process have led the researchers towards maskless methods. In maskless photolithography, a laser beam is focused on the photoresist to expose the desired pattern. In this method, the pattern information is stored in a digital form rather than a physical mask, which enables fast and active edit of the design for an arbitrary pattern [293], [294].

A Heidelberg Instruments (DWL 66^+) laser lithography system in high-resolution mode was used for the fabrication of plasmonic structures in this thesis. The system utilizes a 375 nm UV diode laser for direct writing on the photoresist. Figure 2.2 shows the fabrication process for plasmonic structures on a Si wafer. AZ 1514H photoresist provided by MicroChemicals was spin-coated on a Si wafer at 6000 rpm for 30 s, with an acceleration rate of 100 rpm/s. The coated wafer was pre-baked for 50 s at 100°C on a hotplate. The pattern was exposed on the photoresist using the Heidelberg laser lithography system. After an optimization process, the exposure parameters were chosen as:

- Laser power: 60 mW
- Intensity: 100%
- Filter: 5%
- Focus offset: +100% (Pneumatic mode)

After exposure, the pattern on the photoresist was developed using AZ 726 MIF developer provided by MicroChemicals. Development took place at room temperature by dipping the wafer into the developer solution for 20-30 s, based on the design and size of the features. A hard bake for 50 s at 115°C on a hotplate was used to stabilize the patterned features on the photoresist. As the next step, the wafer was taken to a PVD chamber for the deposition of the plasmonic metal. After thin film deposition, a lift-off process was performed by dipping the wafer into AZ 100 remover provided by MicroChemicals. After washing away the sacrificial photoresist and the metal excess, the aimed metal structures were left on the Si wafer as can be seen in Figure 2.2f.

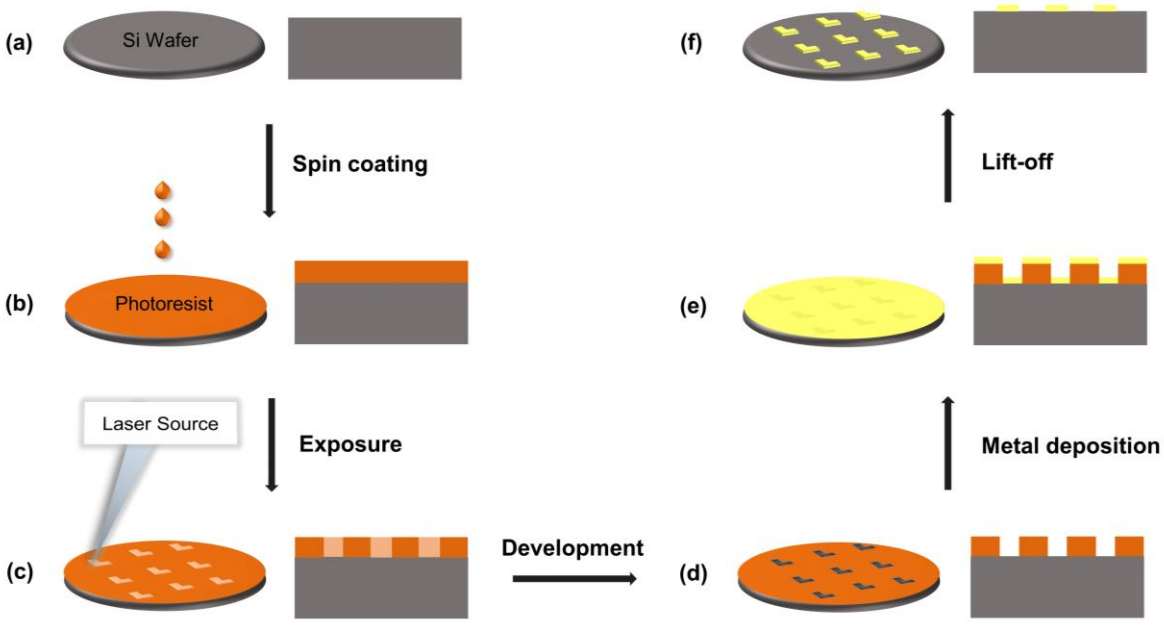

Figure 2. 2. Schematic illustration fabrication process (maskless photolithography and lift-off) for plasmonic structures.

2.2 Characterization

Thicknesses of the MO films grown for this thesis were measured by means of profilometry. The phase composition and crystalline structure of the films were studied by X-ray diffraction. Atomic force microscopy was performed for the investigation of surface topography and calculation of the surface roughness in the films. The optical properties of the films were measured by spectrophotometry. Finally, the Raman scattering data were collected by Raman spectroscopy.

2.2.1 Profilometry

Profilometry provides a simple method for determining the thickness of a film on a substrate. In this method, a stylus with an extremely fine tip scans the surface of the sample on a straight line while its height is recorded as a function of position. For measuring the thickness of a film on a substrate, the substrate needs to have an uncovered part where the deposited film makes a vertical step on the substrate. By measuring the vertical displacement of the stylus between the film surface and the substrate surface, i.e. the step size, one could determine the thickness of the film. A Bruker (DektakXT) stylus profiler was used for the film thickness measurements in this thesis.

2.2.2 X-ray diffraction

X-ray diffraction (XRD) is a characterization technique based on the diffraction of an incident monochromatic X-ray beam from atomic planes of a material, which provides information about the crystalline structure of the tested materials. Diffraction is caused by the interference of the waves scattered by electrons in the atomic sites, which is constructive only in the specific directions stated by Bragg's law:

$$2d \sin\theta = n\lambda \quad (2.1)$$

where d is the spacing between the atomic planes, θ is the angle of the incident beam with the surface of the sample, n is an integer showing the order of diffraction, and λ is the wavelength of the beam [154], [295], [296].

A Bruker (D8 Advance) X-ray diffractometer was used to study the phase composition of the MO thin films in this thesis. A silicon zero diffraction plate provided by MTI Corporation was used under the samples to avoid noise and spurious peaks from the sample holder. XRD tests were performed in a Bragg-Brentano θ-θ configuration, where the sample is fixed but the X-ray source and the detector simultaneously scan a range of θ angle to record the diffraction pattern resulting from the lattice planes with different orientations (Figure 2.3). The angle between the extension of the incident beam and the reflected beam is equal to 2θ. A 2θ range of 15-55° was scanned for the thin films in this study.

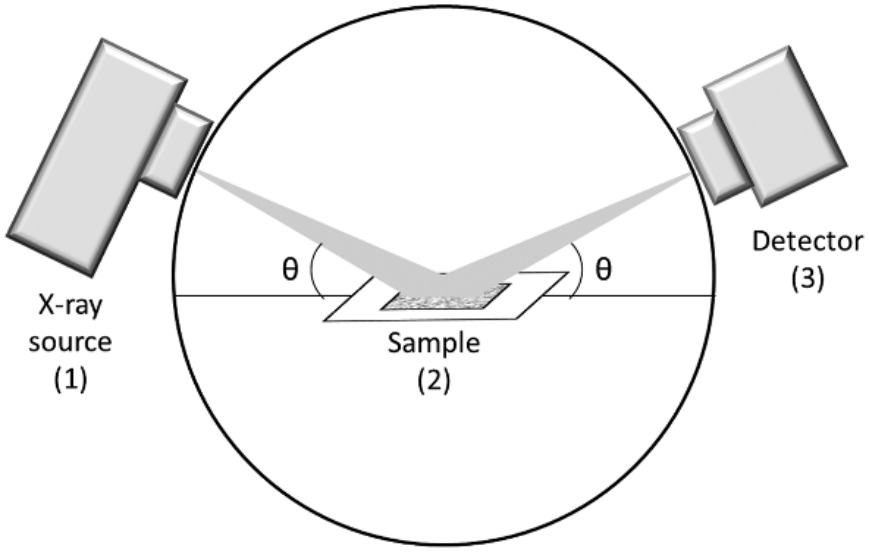

Figure 2. 3. Schematic illustration of the X-ray diffractometry configuration [297].

2.2.3 Atomic force microscopy

Atomic force microscopy (AFM) enables a high-resolution investigation of the surface topography based on the interaction of a mechanical probe with the sample. The probe is comprised of a sharp tip fixed to the open end of a cantilever which can raster scan the surface of the sample. The sample-probe interaction which involves atomic-scale forces is transduced

to the deflection of the cantilever on a larger scale. The height of the probe is recorded providing information about the surface topography.

A Bruker (Dimension Icon) AFM system was used in this thesis to measure the surface roughness of the MO films and investigate the surface topography of the plasmonic structures. The root mean squared (RMS) parameter is used to report the surface roughness:

$$R_q = \sqrt{\frac{1}{l_r}\int_0^{l_r} z(x)^2 dx} \tag{2.2}$$

where R_q denotes the RMS roughness, l_r is the length of the roughness profile, and $z(x)$ represents the height as a function of the position.

2.2.4 Spectrophotometry

Transmission spectra of the MO thin films were measured by a Shimadzu (UV-3600) UV-VIS-IR spectrophotometer. The system uses a deuterium lamp in the UV range and a halogen lamp in the visible and IR range. A grating-type double monochromator scans the wavelength range. In the UV and visible range, a photomultiplier tube is exploited to detect the transmitted light whereas, in the IR range, an InGaAs photodiode and a cooled PbS photoconductive element are used as the detector.

The measurements were performed using the film holder accessory of the device and in order to adapt the chips to this holder, 3D printed chip holders were used. For normalizing the measurement results, a baseline with no samples on the way of the optical path was acquired before measuring the samples. Transmission data for the films were collected in the wavelength range of 200-1800 nm with scanning steps of 1 nm. The light coming from the lamp with a slit width of 1 nm was passed through a sample and a free sample holder as the reference, and the detected light was reported after comparison.

2.3 Modeling

Finite-Difference Time-Domain (FDTD) method was used to model the optical and MO phenomena in this thesis. FDTD is a numerical method for simulating the EM waves in interaction with arbitrary structures of various materials by solving Maxwell's equations in

the time domain. In contrast to frequency-domain methods that solve the problem for only one frequency at a time, FDTD is capable of solving for an entire frequency range with a single simulation, which makes it an ideal method for modeling dispersive and broadband systems [298].

Maxwell's equations formulate the fundamentals of classical electromagnetism and describe the intercorrelation of electric and magnetic fields originating from charge and current density distributions:

$$\nabla \times \vec{E}(\vec{r},t) = -\frac{\partial}{\partial t}\vec{B}(\vec{r},t) \tag{2.3}$$

$$\nabla \times \vec{H}(\vec{r},t) = -\frac{\partial}{\partial t}\vec{D}(\vec{r},t) + \vec{J}(\vec{r},t) \tag{2.4}$$

$$\nabla \cdot \vec{D}(\vec{r},t) = \vec{\rho}(\vec{r},t) \tag{2.5}$$

$$\nabla \cdot \vec{B}(\vec{r},t) = 0 \tag{2.6}$$

where $\vec{E}$, $\vec{H}$, $\vec{D}$, $\vec{B}$, $\vec{J}$, $\vec{\rho}$, and $\vec{r}$ are the electric field [$V \cdot m^{-1}$], magnetic field [$A \cdot m^{-1}$], electric flux density [$C \cdot m^{-2}$], magnetic flux density [$Wb \cdot m^{-2}$], electric current density [$A \cdot m^{-2}$], electric charge density [$C \cdot m^{-3}$], and position [m] vectors, respectively, and t denotes time. In the FDTD method, Maxwell's equations are discretized in time and space dimensions. The spatial discretization is performed via a Cartesian staggered grid suggested by Yee in 1966. Cartesian components of the electric and magnetic fields, i.e. E_x, E_y, E_z, H_x, H_y, and H_z, are not collocated and each component is measured at a specific position in the Yee cell. As illustrated in Figure 2.4, an electric field component E_i is offset by half a grid step in the direction i and the magnetic field component H_i is offset by half a grid step in every direction but i [299]–[301].

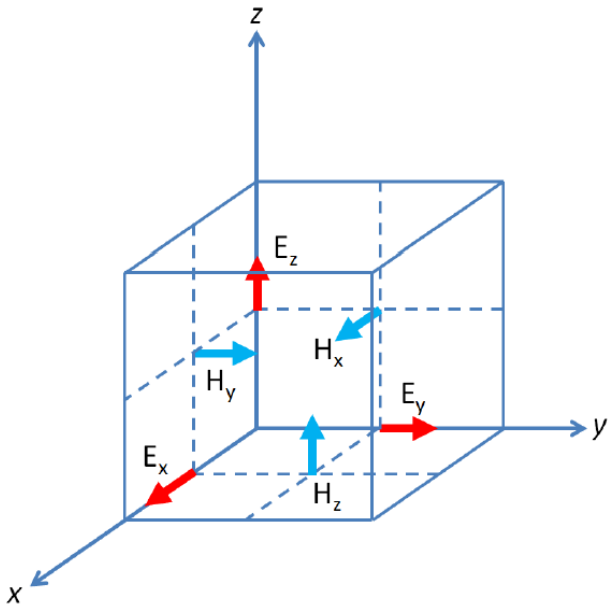

Figure 2. 4. Positions of the electric and magnetic field components in a unit cell of the Yee grid lattice [302].

Yee algorithm entails temporal staggering as well so that the electric and magnetic fields are solved sequentially by a leapfrog scheme, with half a time step offset. Assuming the simulation time step as Δt, the calculations are performed with the following temporal sequence:

$$E(t=0) \rightarrow H(t=\tfrac{1}{2}\Delta t) \rightarrow E(t=\Delta t) \rightarrow H(t=\tfrac{3}{2}\Delta t) \rightarrow \cdots \quad (2.7)$$

When many Yee cells are placed next to one another to fill the entire problem space, each E/H field component is surrounded by four circulating H/E components as shown in Figure 2.5. The new value of an E component in a Yee cell at $t=(n+1)\Delta t$ is related to its old value at $t=n\Delta t$ and the four H components surrounding it. Each H component is calculated in a similar way. Since the H-fields at integer time steps and E-fields at half-integer time steps are not known, an approximation is introduced to complete the calculations. The unknown field component at a time instant is estimated by the average of its known values at half time steps before and after the desired time point [303].

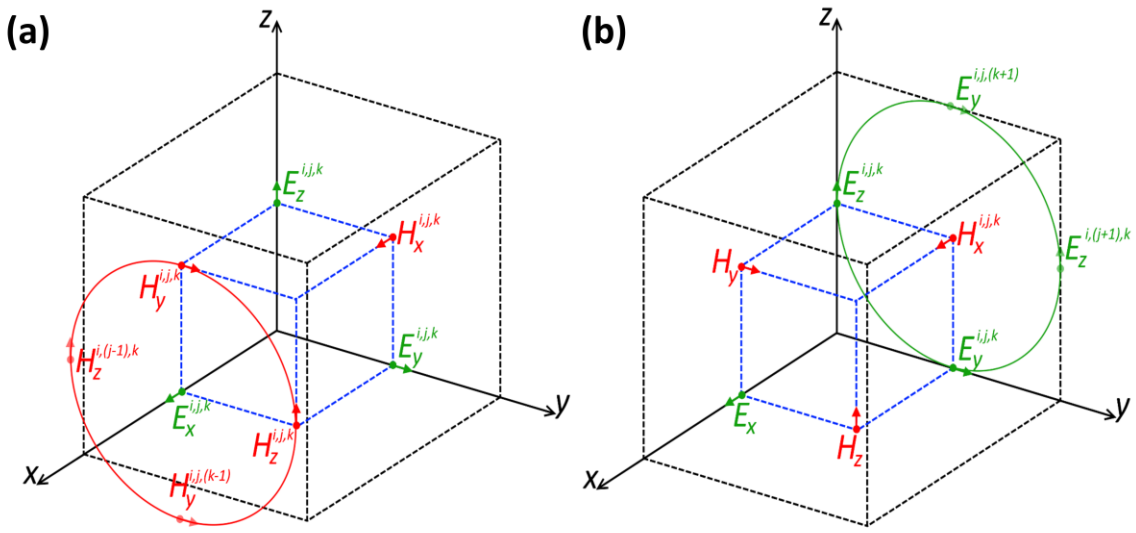

Figure 2. 5. A Yee cell illustrating (a) an E-field component with its neighboring H-field components and (b) an H component with its neighboring E components [304].

Since the FDTD principle is based on interaction with the nearest neighboring mesh cell, the wave must not propagate more than a grid step in one time step. This imposes a relationship between the grid cell size and duration of the time step for calculations:

$$\Delta t \leq \frac{1}{v\sqrt{\frac{1}{(\Delta x)^2}+\frac{1}{(\Delta y)^2}+\frac{1}{(\Delta z)^2}}} \tag{2.8}$$

where v is the maximum velocity of the wave in the simulation region. Equation 2.8 is known as Courant-Friedrichs-Lewy (CFL) stability condition and for a cubic grid cell simplifies to:

$$\Delta t \leq \frac{\Delta}{v\sqrt{3}} \tag{2.9}$$

where Δ is the cell size. Since the time discretization is also proportional to the spatial gridding, the simulation time increases with the fourth power of the grid size in the FDTD method, which leads to long simulation times and the necessity of large computational resources. The feasibility of parallel implementation makes FDTD advantageous in this regard. The simulation space can be divided into multiple blocks to be processed in parallel

using different processors. As each field component is calculated from the nearest neighboring field components, only the outermost field components of the separate blocks need to be exchanged to complete each iteration, which makes the parallel operation quite easy in this method [299], [303].

In this thesis, the Lumerical software package is used to implement FDTD simulations. Lumerical provides a computer-aided design (CAD) environment to create and visualize the simulation geometry. Each object of interest for simulation is assigned with a material that comprises the complex refractive index or permittivity tensor information, required for solving Maxwell's equations. For simulations within a frequency range, Lumerical uses a material fit (complex refractive index/permittivity vs. frequency) based on the data points provided for different frequencies. The FDTD simulation region is truncated by specific boundary conditions (BCs). In this thesis, periodic BCs are used in the directions that the structure has infinite periodicity and perfectly matched layer (PML) BCs are used in the other directions, to account for simulating the objects in the free space. PML represents absorbing BCs which act essentially as layers of lossy material and prevent back reflections by matching the impedances of the PML and the free space. Lumerical also supports non-uniform meshing which offers more efficiency by providing accurate results with shorter computation times and less memory requirement [303].

To perform a simulation, all the field components are initially set to zero. Using a wave source, nonzero values are introduced for some field components according to the physics of the problem. By applying the FDTD algorithm, propagation of the wave throughout the entire simulation region is modeled. In this thesis, plane wave sources that inject laterally uniform EM waves, with incidence normal to the object surface, are used for excitation. When the field components reach a steady state, the energy inside the simulation region falls below a set threshold value, or the time set for the continuation of the propagation has reached, the simulation is terminated. The results produced in the time domain can be easily transformed into the frequency domain by the Fast Fourier Transform (FFT). In Lumerical software, the

frequency-dependent field profile monitors allow for direct measurement of field components at each mesh point [298], [303], [304].

Chapter 3

OPTIMIZATION OF GROWTH CONDITIONS FOR MAGNETOOPTICAL THIN FILMS

Magnetooptical (MO) thin films are crucial components of integrated nonreciprocal photonic devices. Hence, growing MO thin films with bulk quality and high figure of merit (FoM) has attracted remarkable research interest. Ferrimagnetic rare earth iron garnets and particularly, yttrium iron garnet (YIG) with the chemical formula of $Y_3Fe_5O_{12}$ are common MO materials because of their superior MO properties. Partial substitution of Y with elements such as Ce or Bi further improves the MO properties. Cerium doped garnets (Ce:YIG) have been studied extensively for near-infrared telecommunication applications. Ce:YIG has a high specific Faraday rotation (a few degrees per μm film thickness), however, its losses dominate in the visible range and result in low FoM. Lack of such optical losses in bismuth-substituted yttrium iron garnet (Bi:YIG) makes it a more favorable material in terms of MO FoM. Large spin-orbit coupling in Bi^{+3} ion increases the excited state splitting and leads to greater MO activity. Thus, Faraday effect enhances in proportion to the Bi content. On the other hand, this substituent tends to crystallize to secondary phases which deteriorate the transparency and thus, the overall performance of the MO device [85], [114], [160], [168], [305]. According to Table 1.3, Bi:YIG with the composition of $Bi_1Y_2Fe_5O_{12}$ offers the best MO FoM in the RGB wavelengths.

Growing garnet thin films with bulk quality is challenging due to a number of factors. Control over the complex stoichiometry in this class of materials is not feasible with common thin film deposition methods and might be intricate and expensive. Pulsed laser deposition (PLD) enables a controlled transfer of the target stoichiometry to the deposited film. Lighter elements such as Bi, Li, O, etc can be volatile in the PLD plume leading to slight differences

in the film stoichiometry. The choice of targets richer in the mentioned elements can help alleviate this problem. Another difficulty in growing high-quality MO thin films is the high thermal budget required for the crystallization of the garnets, while layers interdiffusion in the film-substrate interface must be prevented using low enough growth temperatures. Such a transition diffusion layer becomes crucial in extremely thin films, as the inhomogeneous layer forms the major portion of the film. An imperfect structure can cause a rough surface and creation of impurity phases as mentioned before, resulting in dropped film quality. Hence, an ex-situ thermal annealing in certain conditions, such as rapid thermal annealing (RTA), might be necessary to assist better crystallization of the garnet film. Polycrystallinity is also a concern in the growth of MO films since scattering from the grain boundaries leads to higher optical losses. Growing garnet thin films on non-garnet substrates is even more challenging due to the incompatibility of lattice parameters and thermal expansion mismatch. Such a disparity can cause strain, defects, and cracks. Garnet films grown on non-garnet substrates are more prone to the formation of secondary phases such as Fe_2O_3, Bi_2O_3, and $YFeO_3$ which prevent perfect crystallization and contribute to the losses [23], [291], [305]–[309].

For decent structural, optical, and MO quality, in addition to the factors mentioned above, other process parameters such as growth rate, chamber pressure, present gases, and target-substrate distance need to be optimized. In this chapter, $Bi_1Y_2Fe_5O_{12}$ thin films grown by PLD on different garnet and non-garnet substrates, with exclusively different deposition parameters are studied for the purpose of optimizing the growth conditions. Fabrication and characterization processes are explained in detail in Chapter 2. A list of the grown samples with corresponding deposition parameters and film thicknesses is given in Table 3.1.

Table 3. 1. List of $Bi_1Y_2Fe_5O_{12}$ thin films grown by PLD using different deposition parameters. Film thicknesses are measured by a Dektak profiler.

Sample	Substrate	Temperature (°C)	O_2 Pressure (mbar)	Pulse repetition rate (Hz)	Film thickness (nm)
G1	GGG	300	0.1	50	150
G2	GGG	500	0.1	50	160
G3	GGG	550	0.1	50	100
G4	GGG	600	0.1	50	90
G5	GGG	650	0.1	50	40
G6	GGG	550	0.05	50	70
G7	GGG	550	0.01	50	150
G8	GGG	550	0.001	50	60
G9	GGG	550	0.1	10	110
G10	GGG	550	0.1	20	50
G11	GGG	550	0.1	100	70
S1	SGGG	300	0.1	50	150
S2	SGGG	500	0.1	50	160
S3	SGGG	550	0.1	50	100
S4	SGGG	600	0.1	50	90
S5	SGGG	650	0.1	50	40
S6	SGGG	550	0.05	50	70
S7	SGGG	550	0.01	50	150
S8	SGGG	550	0.001	50	60
S9	SGGG	550	0.1	10	110
S10	SGGG	550	0.1	20	50
S11	SGGG	550	0.1	100	70
Q1	Quartz	300	0.1	50	150
Q2	Quartz	500	0.1	50	160

Q3	Quartz	550	0.1	50	100
Q4	Quartz	600	0.1	50	90
Q5	Quartz	650	0.1	50	40
Q6	Quartz	550	0.05	50	70
Q7	Quartz	550	0.01	50	150
Q8	Quartz	550	0.001	50	60
Q9	Quartz	550	0.1	10	110
Q10	Quartz	550	0.1	20	50
Q11	Quartz	550	0.1	100	70

3.1 Crystalline structure and phase analysis

X-ray diffraction (XRD) patterns of the $Bi_1Y_2Fe_5O_{12}$ thin films grown on different substrates including gadolinium gallium garnet (GGG), substituted gadolinium gallium garnet (SGGG), and quartz, using different growth parameters are studied for investigation of the crystalline structure and present phases:

3.1.1 Growth on GGG substrate

GGG is a common substrate for the deposition of YIG films due to the identical lattice parameters (12.376 Å), which enables the growth of epitaxial and single-crystalline films. Lattice parameters of the doped garnets are slightly bigger than that of YIG, but GGG can be still used as a substrate for growing these films [291]. XRD patterns of the Bi:YIG thin films grown on single-crystalline GGG (111) substrates are presented in Figure 3.1. All the patterns are compared to that of the bare GGG substrate. The plots are shown with an offset for easier interpretation. GGG has a diffraction peak around $2\theta = 25°$ related to (222) planes and a strong peak centered around 51° for (444) planes, which shows splittings due to the contributions from Cu $K\alpha_1$, $K\alpha_2$, and $K\alpha_{3,4}$ [310], [311].

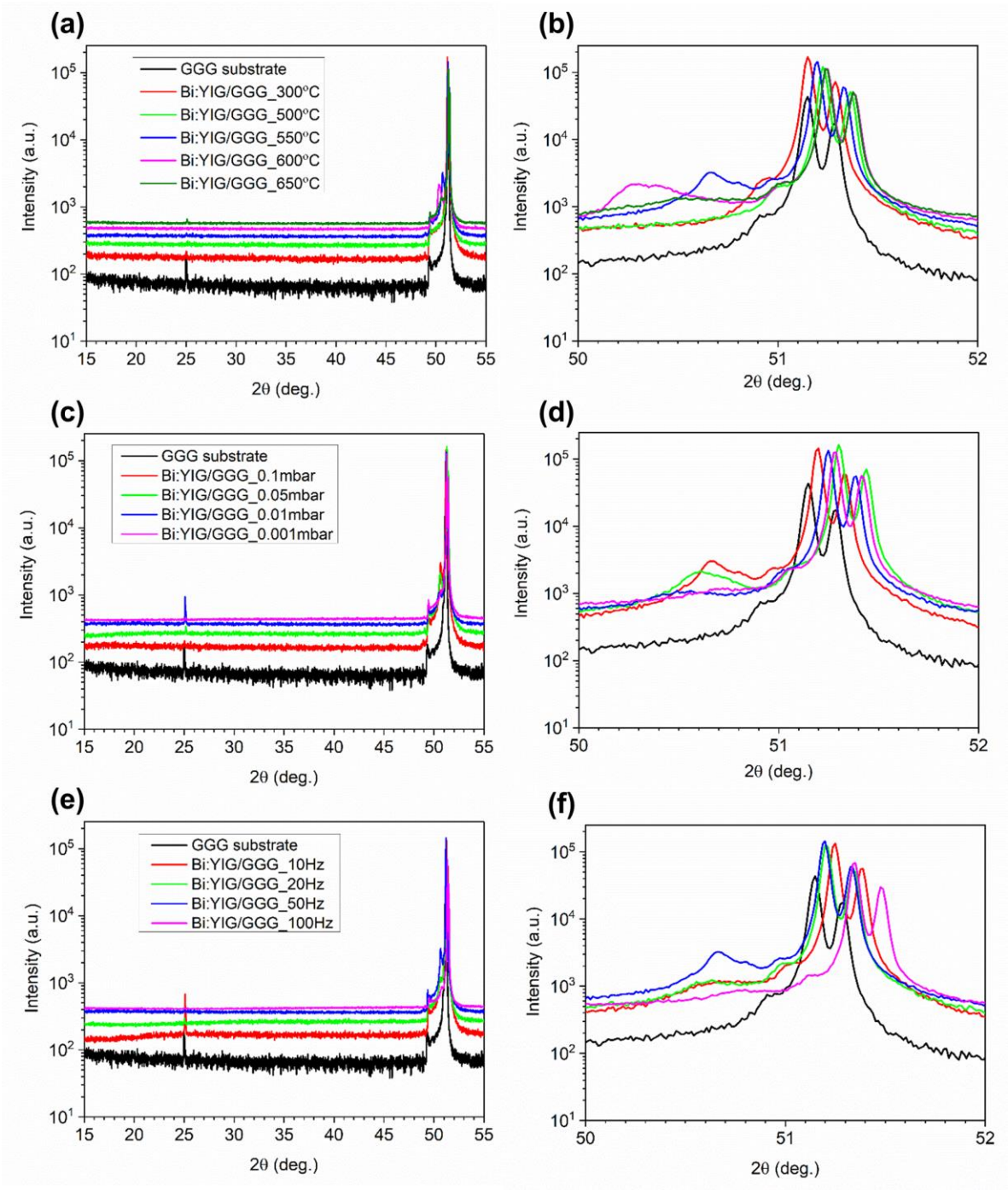

Figure 3. 1. XRD patterns of Bi:YIG thin films grown on GGG at different (a,b) temperatures, (c,d) oxygen pressures, and (e,f) pulse repetition rates.

Figure 3.1a shows the XRD patterns for films grown at different temperatures. All the films studied in this figure are grown at an oxygen pressure of 0.1 mbar and a pulse repletion rate of 50 Hz. In addition to the peaks related to the substrate, the films grown at temperatures of 550-650 °C show diffraction peaks in the 2θ range of 50.2-50.7°, as magnified in Figure 3.1b. These peaks are attributed to the Bi:YIG (444) planes [154], [312] and their intensity decreases by increasing temperature. The film grown at 550 °C shows the sharpest peak which is an indication of achieving better crystal quality at this temperature.

The diffraction patterns of the films grown with different oxygen pressures, at 550 °C and pulse rate of 50 Hz are shown in Figure 3.1c,d. In addition to the substrate peaks, all the films show Bi:YIG (444) peaks around 50.5-50.7° which have lower intensities for lower pressures. Hence, it could be concluded that crystalline quality decreases by decreasing the oxygen pressure. Moreover, a peak around 2θ = 33° is observed for the growth pressure of 0.01 mbar, which can correspond to Bi:YIG (322) planes, contravening the epitaxial nature of this film.

Figure 3.1e compares the XRD patterns for the films deposited at different repetition rates of the laser pulse. Growth temperature and O_2 pressure for the films investigated in this figure are 550 °C and 0.1 mbar, respectively. Only (222) and (444) peaks of GGG and Bi:YIG are detected in these films. As can be observed in the magnified graph (Figure 3.1f), the sharpest Bi:YIG peak is related to the case of 50 Hz, promising for a better crystalline structure at this rate.

3.1.2 Growth on SGGG substrate

SGGG with a lattice parameter slightly larger than GGG (12.480 Å) is conventionally used as a substrate for growing doped YIG [154], [312]. Figure 3.2 presents the XRD patterns for Bi:YIG films grown on single-crystalline SGGG (111) substrates, in comparison to the bare substrate. The plots are shown with an offset for easier interpretation. SGGG has a major peak centered around 2θ = 50.7° with splittings due to Cu $K\alpha_1$, $K\alpha_2$, and $K\alpha_{3,4}$ [310], [311].

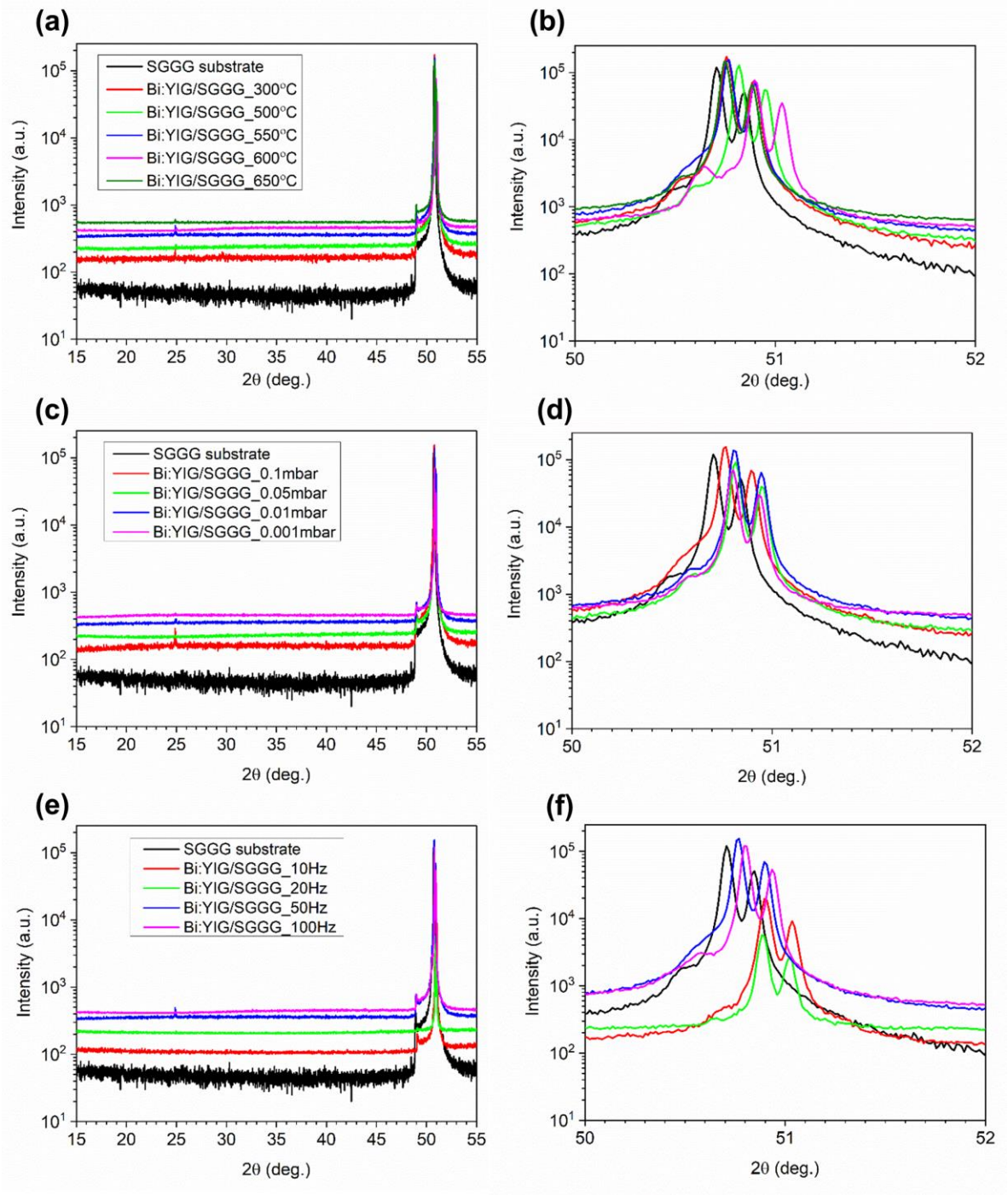

Figure 3. 2. XRD patterns of Bi:YIG thin films grown on SGGG at different (a,b) temperatures, (c,d) oxygen pressures, and (e,f) pulse repetition rates.

Figure 3.2a compares the diffraction patterns for the films grown on SGGG at different temperatures. O_2 pressure of 0.1 mbar and a pulse rate of 50 Hz is used in the deposition of these samples. Bi:YIG (222) peaks around $2\theta = 24.8°$ are detected for all the films. As the magnified graph in Figure 3.2b shows, for the film deposited at 600 °C, another peak is distinguishable within about 0.25° of the main SGGG peak, which can be attributed to Bi:YIG (444). This peak is apparent in the case of 550 °C as well, however, it is highly overlapping with the substrate peak. Bi:YIG has a lattice parameter very similar to SGGG, which makes it difficult to discern the film peak from that of the substrate in the films grown on SGGG.

The effect of oxygen pressure in the deposition of the films is investigated in Figure 3.2c,d. The films that are studied here have been deposited at 550 °C by a pulse rate of 50 Hz. Considering both (222) and (444) peaks, it is observed that Bi:YIG is best crystallized at 0.1 mbar O_2 pressure.

Figure 3.2e,f show the diffraction patterns for the films deposited by different repetition rates of the laser pulses, in a chamber with a temperature of 550 °C and O_2 pressure of 0.1 mbar. For the case of 50 Hz, Bi:YIG (222) and (444) peaks are clearly detectable. By a precise comparison to the substrate pattern, minor Bi:YIG (222) and overlapping Bi:YIG (444) peaks can be observed for the other rates as well.

3.1.3 Growth on quartz substrate

Epitaxial growth of MO Garnets on GGG and SGGG substrates has been extensively demonstrated in the literature [100], [115], [154], [155], [158], [160], [291], [305], [307], [310], [312]–[316]. However, garnet substrates are expensive and for many practical applications, growing MO garnets on common non-garnet substrates such as glass and silicon is important. Another issue with garnet substrates is their strong paramagnetic behavior which causes problems in some magnetic applications [291]. Furthermore, photonic devices such as magnetooptical photonic crystals generally necessitate growing garnet films on SiO_2 [174], [178], [306], [317], [318]. Deposition of Bi:YIG thin films on single-crystalline quartz

(0001) substrates using different growth parameters is studied in Figure 3.3. The plots are shown with an offset for easier interpretation. Quartz shows an intense peak at $2\theta = 50.9°$ related to the (0003) planes, which has splittings that can be attributed to the contributions from Cu $K\alpha_1$, $K\alpha_2$, and $K\alpha_{3,4}$ [311], [319].

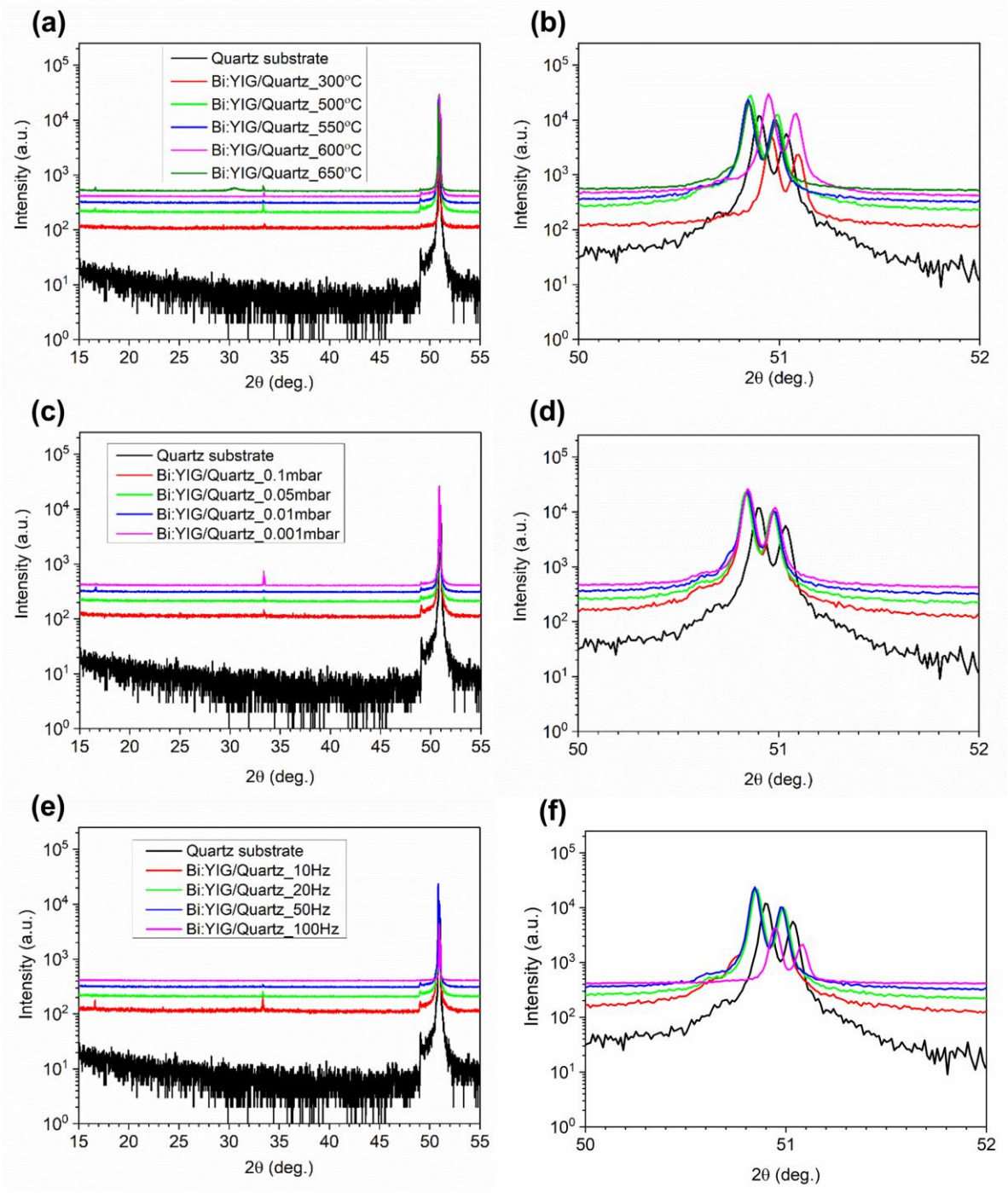

Figure 3. 3. XRD patterns of Bi:YIG thin films grown on quartz at different (a,b) temperatures, (c,d) oxygen pressures, and (e,f) pulse repetition rates.

Figure 3.3a shows the XRD patterns for the films grown on quartz at different temperatures. 0.1 mbar O_2 pressure and 50 Hz pulse rate is used for the deposition of these films. For all the temperatures a film peak at $2\theta = 33.5°$ is observed that can be assigned to Bi:YIG (322) planes. For the films grown at 500 and 650 °C, a peak at $2\theta = 16.6°$ is also detected, which can be attributed to Bi:YIG (211) planes as it is not close to the tabulated data of any impurity phases. For the case of 650 °C, a broad peak centering at $2\theta = 30.4°$ appears in the pattern, which can correspond to hexagonal $YFeO_3$. This peak indicates the formation of a secondary phase with a short-range order, at such a growth temperature [320], [321]. Bi:YIG (444) peaks around 50.7° are not clearly distinguishable here because of the tight overlap with the main substrate peak. However, for the case of 650 °C, a small hump is observed on the side of the substrate peak, which shows the presence of these grains (Figure 3.3b).

Studying the effect of oxygen pressure for the films grown at 550 °C and 50 Hz in Figure 3.3c shows the diffraction of Bi:YIG (322) planes in all the films, but more pronounced in the case of 0.001 mbar. Bi:YIG (211) planes are only detectable in the films grown at 0.01 and 0.001 mbar. For the case of 0.01 mbar, a hump on the side of the substrate peak leads to recognition of Bi:YIG (444) peak, despite the close overlap of the two peaks (Figure 3.3d).

The diffraction patterns of the films grown by different pulse rates at 550 °C and O_2 pressure of 0.1 mbar are shown in Figure 3.3e. No crystalline phase is observed in the film grown at 100 Hz, whereas the smaller rates result in the formation of Bi:YIG (322). At the low rate of 10 Hz, Bi:YIG (211) planes are also detected, and higher magnification around 50-51° (Figure 3.3f) shows a hump on the substrate peak indicating the presence of Bi:YIG (444) as well.

3.2 Topography and surface roughness

All the Bi:YIG films grown on different substrates and under different growth conditions have flawless adhesion and smooth surfaces. No cracks are observed in the deposited films. The topography of the films is investigated by atomic force microscopy (AFM), as presented in Figure 3.4. RMS roughness values extracted from the AFM measurements indicate surface

roughness of 0.55, 0.43, and 0.88 nm for the films grown on GGG, SGGG, and quartz, respectively. As expected, the film on quartz substrate has a higher roughness in comparison to the epitaxial films on garnet substrates.

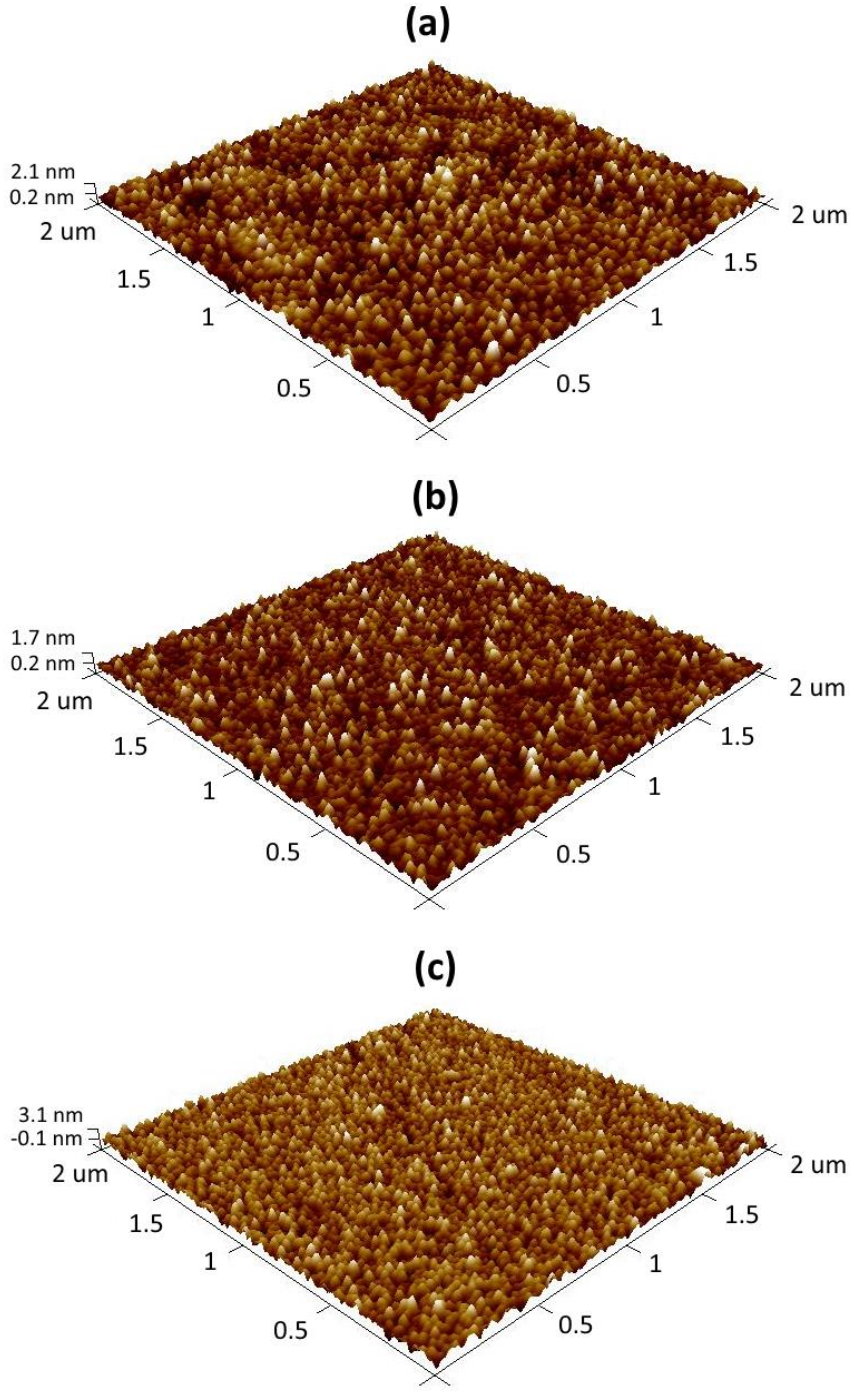

Figure 3. 4. Surface topography of Bi:YIG films grown on (a) GGG, (b) SGGG, and (c) quartz substrates, measured by atomic force microscope over a 2 μm × 2 μm area.

3.3 Optical properties

The optical properties revealing the electronic bandgap of the films grown on GGG, SGGG, and quartz substrates under different growth conditions are studied in this section.

Figure 3.5 presents the optical transmission of the films grown on GGG as a function of wavelength, compared to the bare substrate. GGG shows a band edge at the wavelength of 228 nm with a band tail extending towards 800 nm. At $\lambda = 274$ and 313 nm sharp absorption lines are observed which are related to 4f-4f electronic transitions of the Gd^{3+} ions from ^{8}S ground state to ^{6}I and ^{6}P, respectively [322]. Bi:YIG/GGG samples show similar transmission spectra with the same band edge but lower transmission and shift of the band tail towards IR regime.

Transmission spectra for the films grown on SGGG substrate are shown in Figure 3.6. SGGG has a spectrum similar to that of GGG, with a band edge at $\lambda = 236$ nm and a shorter band tail. The absorption peaks appear at the same wavelengths as stated for GGG, with higher absorption values in this case. The Bi:YIG/SGGG samples also show optical behavior similar to the bare substrate, with a reduction in transmission and extension of the band tail.

Figure 3.7 compares the optical spectra of the films grown on quartz to that of the bare substrate. Quartz has a spectrum different than those of GGG and SGGG, with no band edge in the studied range of 200-1800 nm. Addition of a Bi:YIG layer changes the optical behavior to a spectrum with a band edge around 200 nm and a band tail extending to the visible range.

The steps appearing in the spectra around 310, 720, and 830 nm are due to the switching between different light sources or detectors used in the spectrophotometer device. The difference in the transmission of the films grown in different conditions can be ascribed to the difference in the thickness (Table 3.1) and the structure of the films. The films grown at 650 °C have a smaller thickness and thus, higher transmission compared to the films deposited at lower temperatures. The films grown at 10 Hz have the highest thickness and hence, the lowest transmission values among the films processed at different rates.

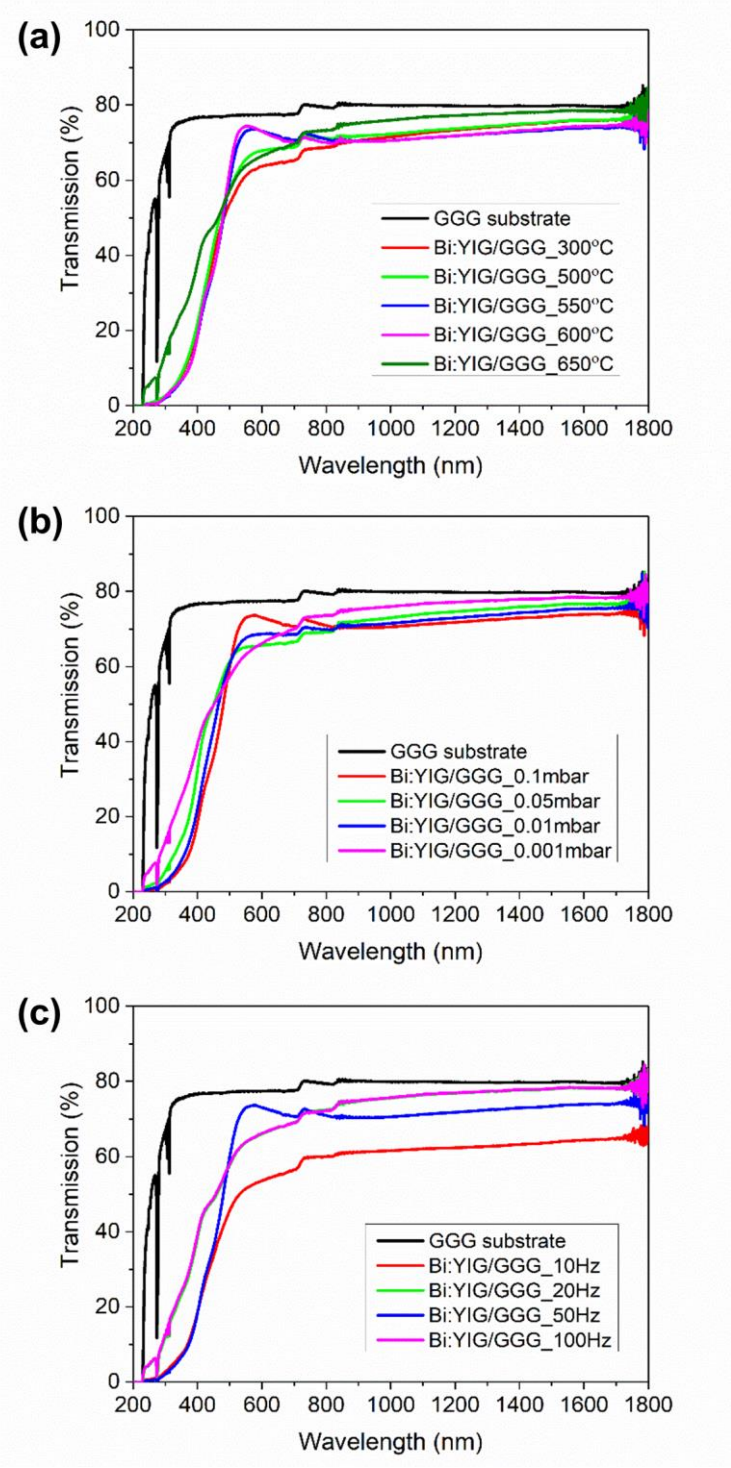

Figure 3. 5. Transmission spectra of Bi:YIG films grown on GGG at different (a) temperatures, (c) oxygen pressures, and (e) pulse repetition rates.

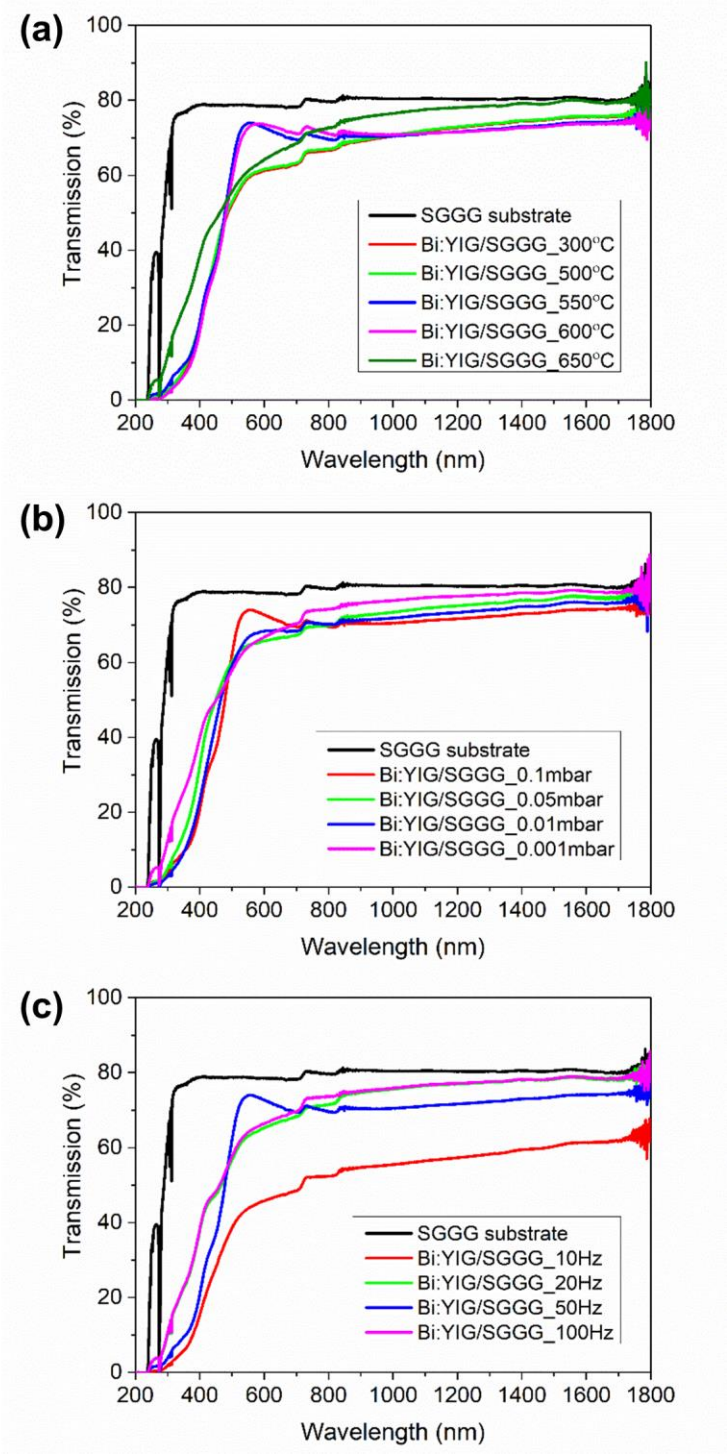

Figure 3. 6. Transmission spectra of Bi:YIG films grown on SGGG at different (a) temperatures, (c) oxygen pressures, and (e) pulse repetition rates.

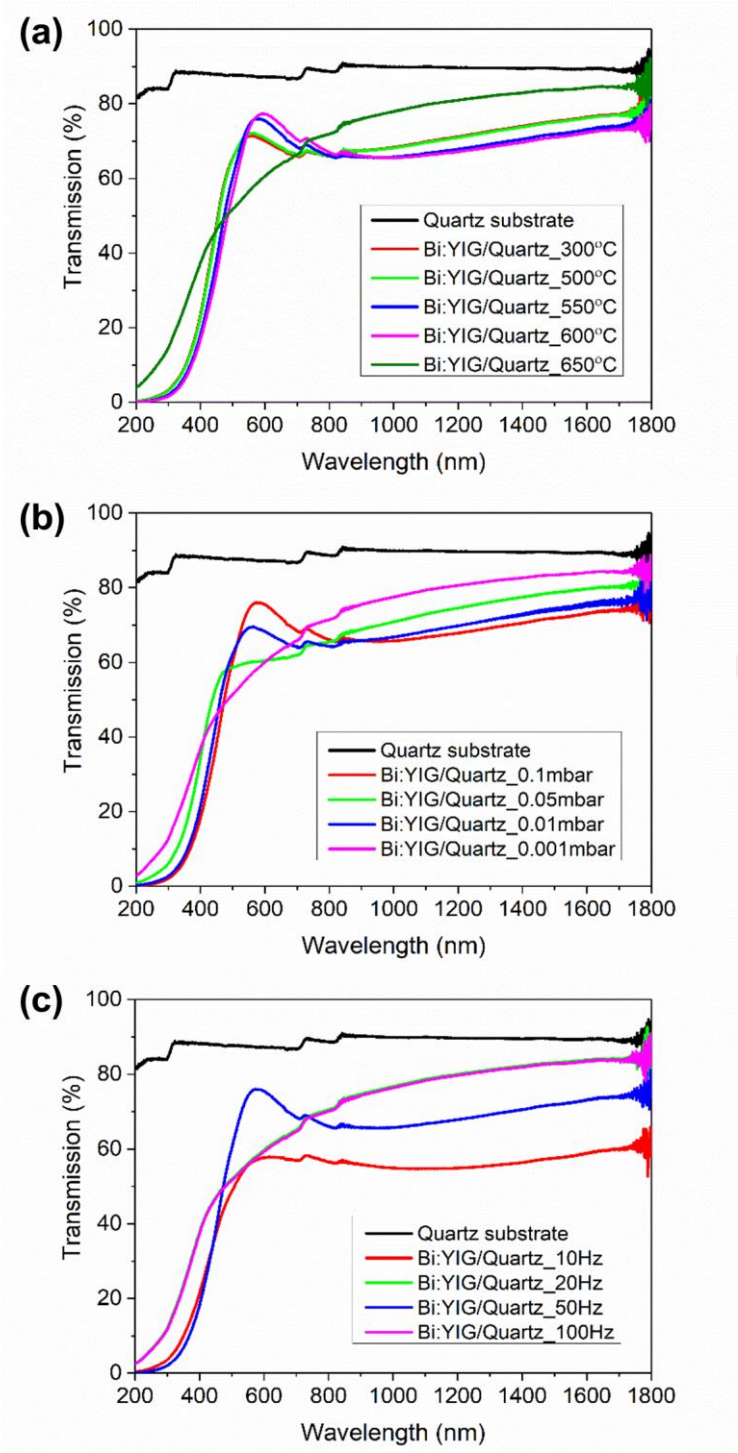

Figure 3. 7. Transmission spectra of Bi:YIG films grown on quartz at different (a) temperatures, (c) oxygen pressures, and (e) pulse repetition rates.

3.4 Summary

In this chapter, magnetooptical Bi:YIG films with a chemical composition of $Bi_1Y_2Fe_5O_{12}$ on GGG, SGGG, and quartz substrates, grown by pulsed laser deposition at different temperatures (300-650 °C), oxygen pressures (0.001-0.1 mbar), and pulse repetition rates (10-100 Hz) are studied in order to optimize the growth condition.

Epitaxial films were achieved on GGG with the best crystalline quality being related to the growth parameters of 550-600 °C, 0.05-0.1 mbar, and 50 Hz. On SGGG substrate, the best epitaxial films are realized in similar conditions of 550-600 °C, 0.1 mbar, and 50 Hz. No impurity phases were crystallized in the films grown on GGG and SGGG. Growth on the quartz substrate mostly resulted in polycrystalline Bi:YIG films. For the film grown at 650 °C, a secondary phase (hexagonal $YFeO_3$) with a short-range order was formed in addition to Bi:YIG. Recommended growth parameters to obtain single-phase and high-quality garnet on quartz substrate are a temperature of 550-600 °C, 0.05-0.1 mbar O_2 pressure, and a rate of 20-50 Hz.

All the films grown at different growth conditions on different substrates had perfect adhesion and smooth surface with RMS surface roughness below 1 nm. Transmission measurements showed typical garnet spectra for all the films with a band edge around λ = 200 nm and a band tail extending towards visible and IR range. The transmission values for different films were slightly different, depending on the thickness and structure of each film. Further optical, magnetic, and magnetooptical measurements will be performed on the films to fulfill a comprehensive characterization and optimization study, as a future study.

Chapter 4

RGB MAGNETOPHOTONIC CRYSTAL

Magnetooptical (MO) effects have demonstrated great potential for light modulation since they provide nonvolatility, ultrahigh speed, and the possibility of using thin films and size scalability, as discussed in Chapter 1. Magnetooptical spatial light modulators (MOSLMs) hold promise for integrated photonic devices emerging optoelectronic, particularly holographic systems and 3D displays, which require fast modulation and fine spatial resolution [80]–[82], [323]. The major challenge on the way of expanded application and industrialization of MOSLMs for this purpose is the inherent weakness of MO effects, while the contrast ratio of the modulation depends on the magnitude of the polarization rotation resulting from the MO effect. Thus, realizing practical miniaturized MOSLMs for 3D imaging and display applications necessitates enhancement of MO effects at fundamental wavelengths of red, green, and blue (RGB) [35], [87].

Magnetophotonic crystal (MPC), which is formed by introducing MO defects to the periodic structure of a photonic crystal (PC), offers a method to enhance MO effects [23], [83], [174]–[180]. In this method, MO films are sandwiched between two sets of Bragg mirrors comprised of alternating high- and low-index dielectrics. In such a structure, the MO films act as PC cavities where the EM waves are trapped, resulting in significant enhancement of the MO effects. The continuous translational symmetry is broken in a PC structure and only discrete translational symmetry is present due to the periodicity of the structure. Depending on the wavelength, some EM waves cannot propagate through the PC because of the destructive interference of multiple reflections in the structure, which leads to a photonic bandgap in the transmission spectrum. By inclusion of a defect in such a periodic structure, the discrete translational symmetry is further broken, which allows for propagation

of some wavelengths in the forbidden band and results in the appearance of a transmission peak in the bandgap.

Having a cavity with MO property, i.e. nonzero off-diagonal component in the permittivity tensor ($\varepsilon_{xy} \neq 0$), in the PC breaks the time-reversal symmetry as well and enables nonreciprocity [324], [325]. For the wavevectors that satisfy the phase-matching condition in such a structure and propagate through, PC cavity modes accumulate and enhance the MO effects by back and forth reflections and increasing the optical path length in the MO material. In an early study, Inoue et al. [174] showed that enhancement of Faraday rotation (FR) in an MPC is related to the localization of the EM wave in the MO layer and larger enhancement is achievable by stronger localization effect. Using a similar approach, Moccia et al. [326] demonstrated 12º FR in a tri-layer composed of a dielectric layer sandwiched between two metallic MO layers.

MPC enables the filtering of undesired wavelengths originating from a broadband light source in addition to the remarkable enhancement of MO effects. Better localization and higher enhancement in MO effects are expected by increasing the number of dielectric layers in the Bragg mirrors and improving the cavity quality factor. Moreover, having further MO cavity layers in MPC structure could yield a larger MO rotation angle. However, these factors contribute to the accumulation of optical losses by increasing the number of passes and overall optical path length within the structure. On the other hand, the optical and MO response of an MPC is affected by the material properties, thickness, and relative position of the constituent layers. Thus, an application-based optimization of the MPC structure is essential to obtain an efficient device with a sufficiently large MO effect and small optical loss.

In this chapter, MPCs with different configurations are investigated and compared based on the calculated figure of merit (FoM). An MOSLM capable of simultaneous modulation at RGB wavelengths with rotation angles larger than 20º is demonstrated. In the first section, the proposed device structure and the operation principle are introduced. Next, the

optimization process for display applications is discussed. Finally, a summary and design rules for RGB MOSLMs are presented.

4.1 Proposed Device Structure and Operation Principle

The structure of a magnetophotonic crystal-magnetooptical spatial light modulator (MPC-MOSLM) based on the Faraday effect and working in transmission mode is schematically illustrated in Figure 4.1. A randomly polarized wave originating from a light source attains linear polarization by passing from a polarizer and propagates through the MPC, which rotates the polarization plane due to Faraday Effect. The second polarizer, known as the analyzer, is set orthogonal to the first one. So with no magnetization in the MO layers and subsequently no polarization rotation, the outcoming light intensity would be zero (OFF status) as light cannot pass the combination of two orthogonal polarizers. However, by magnetizing the MO layers which leads to a rotation of polarization, the light passing MPC will gain some polarization component in the direction that the analyzer is set. As a result, a nonzero light intensity would be observed at the exit (ON status). The outcoming light intensity could be modulated by controlling the magnetization. Generally, the OFF and ON states could be set to correspond respectively to $-\theta_F$ and $+\theta_F$ (θ_F: Faraday rotation angle), yielding a modulation depth proportional to a range of $2\theta_F$. Nonetheless, the MPC structures proposed here are optimized for three wavelengths (RGB) at which, FR angles are different. Therefore, a common baseline corresponding to 0° rotation is suggested so that for all three wavelengths, the OFF status resembles zero light intensity. Using this scheme, i.e. the MPC-MOSLM within $0\text{-}\theta_F$ instead of the conventional range of $-\theta_F$ to $+\theta_F$, a simple operation system is devised and the contrast ratio can be optimally maximized for all three colors.

Figure 4. 1. Schematic illustration of the proposed structure and operation principle for the magnetophotonic crystal-magnetooptical spatial light modulator (MPC-MOSLM) based on the Faraday effect and working in transmission mode. A light beam from a laser or light-emitting diode (LED) with initial random polarization is passed through a polarizer. The vertically polarized light propagates through the MPC structure in the form of $(H/L)^p/(D/L)^q/(H/L)^p$, which is engineered to yield maximum transmission and Faraday rotation values in the targeted wavelengths. H, L, and D respectively stand for high-index, low-index, and defect dielectric layers in the MPC structure, shown by red, gray, and green colors in the figure. Due to the polarization rotation by the Faraday effect, the transmitted light acquires some polarization component in the horizontal direction, which is analyzed by a second polarizer, set in the horizontal orientation. By controlling the magnetization state of the magnetooptical defect layers, the polarization rotation and consequently, the magnitude of the horizontal component can be controlled and as a result, the outcoming light intensity can be modulated.

The MOSLM pixel contrast is defined as the ratio of transmitted light intensity at maximum FR to the signal intensity at zero FR. This definition takes into consideration that even at zero FR, there is a small nonzero signal passing the combination of two perpendicular polarizers, which is caused by unavoidable small angle difference from the extinction conditions. By calling this angle θ_P (polarizer misorientation), we quantify the MOSLM contrast ratio (CR) as:

$$\mathrm{CR} = \frac{\tan(\theta_F)}{\tan(\theta_P)} \tag{4.1}$$

where θ_P can be made arbitrarily small through an iterative feedback-controlled procedure for zeroing the angle between two polarizers. Misalignment angles as small as 0.086° have been reported [327] and this value is used to calculate CR for the MPC-MOSLM proposed here.

The proposed MPCs have structures in the form of $(H/L)^p/(D/L)^q/(H/L)^p$, composed of TiO_2 as high-index (H) and SiO_2 as low-index (L) dielectrics for the Bragg mirrors, and $Bi_1Y_2Fe_5O_{12}$ as MO defect (D). TiO_2 and SiO_2 are highly transparent and provide adequate index difference for a wide photonic bandgap in visible range [328]–[330]. $Bi_1Y_2Fe_5O_{12}$ was selected as the constituent material for the MO components because of its high FoM at all three RGB wavelengths (Table 1.3). $FeBO_3$ provides high FoM, but the challenges associated with its practical use, such as difficulty in single-crystalline growth and complications caused by its birefringence make it an unsuitable candidate for MO devices [107], [116], as discussed in section 1.1.1.

Previous efforts for growing magnetic garnets on non-garnet substrates [28], [85], [159], [331], [332] and fabricating magnetophotonic crystals [23], [180], [317], [318], [333] have mostly led to polycrystalline garnet structures, whereas the epitaxial growth on single-crystalline garnet substrates generally offers better optical and MO properties. Polycrystalline garnets may have weaker MO properties and higher optical losses due to the imperfect control on crystalline orientation and stoichiometry, and scattering from the grain boundaries. The deposition of garnet on non-garnet sublayers might also cause cracks and mechanical failure due to the lattice mismatch. Supplementary methods such as seeded-growth and thermal annealing [85], [169] could help alleviate these issues, especially in the films with small thicknesses. Besides, as the grain sizes of the garnet thin films on non-garnet layers can be larger than 5 μm in diameter, a near single-crystalline quality could be achieved for each small pixel in MOSLM [334]. In this study, the experimental data for polycrystalline $Bi_1Y_2Fe_5O_{12}$ [98] was used to design and calculate the response of magnetophotonic

structures. Thus, the fabrication challenges are taken to account and epitaxial films are not essential for implementing the MPC-MOSLMs presented here.

Ideal MO materials for imaging and display MOSLMs must have (i) stable structure, (ii) a wide material bandgap, (iii) low optical losses (which necessitates optimal stoichiometry and minimum concentration of oxygen vacancies), and (iv) high Faraday rotation in the visible band. For the device development purposes, novel MO materials with the mentioned properties and high FoM need to be developed.

In the following section, the performance of MPCs with different cavity structures is investigated and an optimized MPC for RGB MOSLMs is presented. Layer thicknesses were primarily assigned as quarter-wavelength for mirror dielectrics and half-wavelength for MO defects. However, for the MPCs with more than one defect, which have multiple peaks in their transmission spectra, a thorough thickness optimization is required to attain peaks at the desired wavelengths, as the hybridization of photonic modes causes a peak position to be affected by the presence of other peaks. It is also signified how changes in the structure and material properties affect the behavior of such an MPC and the device FoM.

4.2 Structure optimization

4.2.1 One-defect MPC

An inclusive optimization study on MPCs is performed starting with a one-defect MPC. Figure 4.2 depicts the transmission spectrum of an MPC having $(H/L)^p/(D/L)^q/(H/L)^p$ structure (H: SiO_2, L: TiO_2, D: Bi:YIG), where $p = q = 1$ and the layer thicknesses are set in a way that the transmission peak occurs within the green band. A bandgap covering the visible range is observed and the transmission peak is located at λ=519 nm. The calculation spectra with and without taking into consideration the absorption of Bi:YIG (shown by black and gray lines, respectively) describe the effect of material loss on the optical response of the MPC. The results reveal that the bandgap formed by the photonic crystal commences at a wavelength around 360 nm but due to considerable material loss in the ultraviolet range, the band edge is not discernible in the spectrum including the material loss.

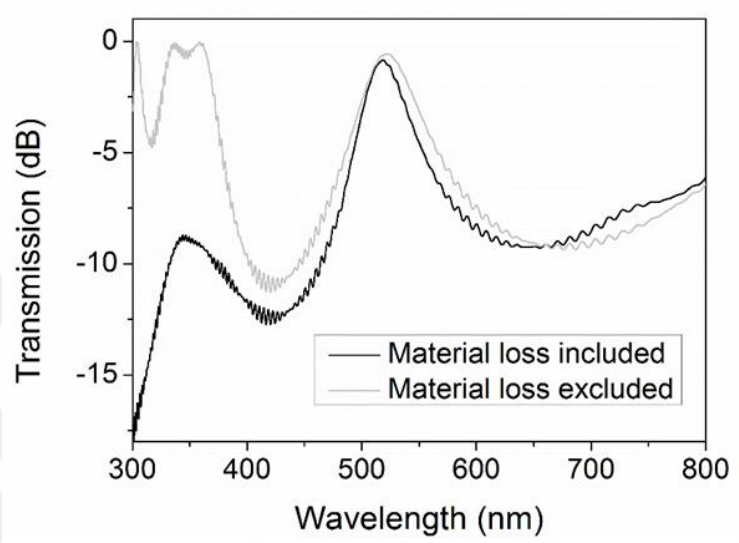

Figure 4. 2. The transmission spectrum of the MPC with (H/L)/(D/L)/(H/L) structure. The black line represents calculations that consider optical absorption of Bi:YIG and the gray line assumes the MO material is lossless (no imaginary part in the refractive index).

Figure 4.3 demonstrates how the number of (H/L) bilayers in the Bragg mirrors affects the performance of the single-defect MPC. Both FR and loss increase by adding more mirror layers to the structure, however, the domination of the rise in loss causes the FoM to drop considerably in the photonic crystal structure in comparison to the bare MO film (Figure 4.3b).

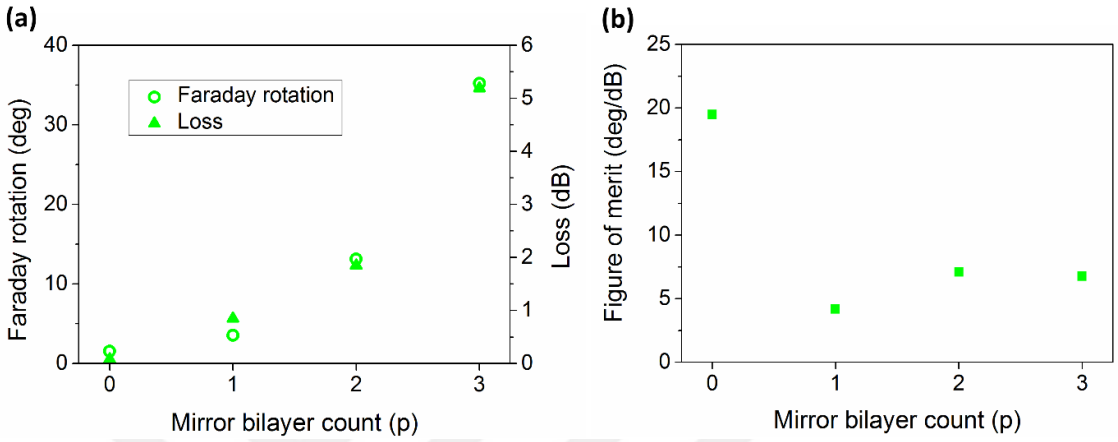

Figure 4. 3. Effect of the number of mirror bilayers on the performance of the one-defect magnetophotonic crystal. (a) Faraday rotation, loss, and (b) figure of merit calculated for the magnetophotonic crystal with $(H/L)^p/(D/L)/(H/L)^p$ structure, at its resonance peak around λ=519 nm.

4.2.2 Two-defect MPC

The transmission spectrum of a two-defect MPC with $(H/L)^p/(D/L)^q/(H/L)^p$ where p = q = 2, is presented in Figure 4.4. In this structure, there are two sets of H/L bilayer in the mirrors, each corresponding to one of the defects. By adding a second defect to the structure of MPC, not only a new transmission peak appears in the bandgap but also the position of the first peak changes, as observed previously as well [335]. Although the band edge in shorter wavelengths has slightly redshifted, the bandgap still covers the visible range. The transmission peaks are at λ=502 nm (green) and 596 nm (red).

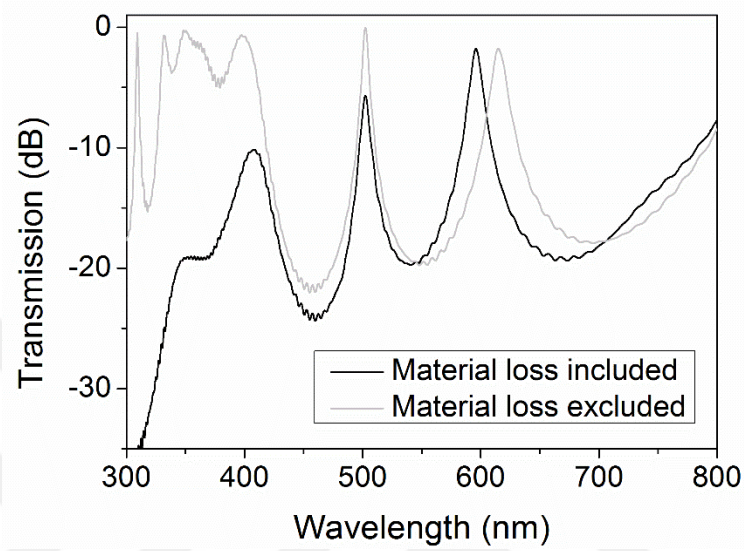

Figure 4. 4. The transmission spectrum of the MPC with $(H/L)^2/(D/L)^2/(H/L)^2$ structure. The black line shows the case where optical absorption of Bi:YIG is taken into consideration and the gray line assumes the MO material is lossless (no imaginary part in the refractive index).

Figure 4.5 signifies how the number of mirror bilayers in the two-defect MPC affects FR, loss, and FoM at the two resonance peaks. Increasing the number of H/L bilayers notably improves FR such that with 6 sets of bilayers in the mirrors, about 41º and 84º FR is attained for the peaks in the green and red bands, respectively. Progressively increasing loss for the structures with more than 2 mirror bilayers causes a drop in the figure of merit for green wavelength whereas for red, bilayers count of 4 offer the optimum structure and leads to an FoM higher than 10 $^{o}\cdot dB^{-1}$ (Figure 4.5b).

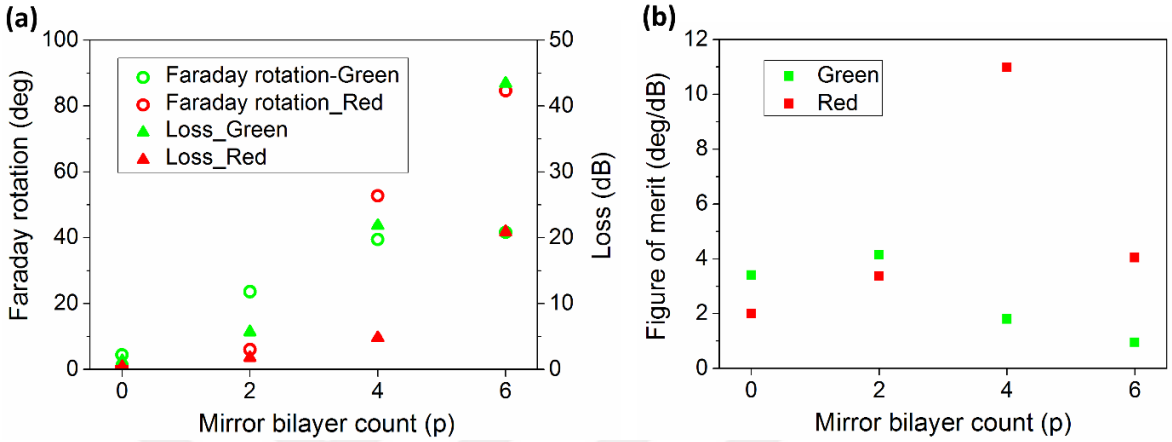

Figure 4. 5. Effect of the number of mirror bilayers on the performance of the two-defect MPC. (a) Faraday rotation, loss, and (b) figure of merit calculated for the two-defect MPC with $(H/L)^p/(D/L)^2/(H/L)^p$ structure, at its resonance peaks around λ=502 nm (green) and λ=596 nm (red). Green and red colors on the graphs represent green and red wavelengths, respectively.

4.2.3 Three-defect MPC

For an MOSLM capable of light modulation at RGB, an MPC with three defects yielding resonance peaks within the red, green, and blue bands is proposed. Figure 4.6 demonstrates the transmission spectrum for such an MPC with $(H/L)^p/(D/L)^q/(H/L)^p$ structure, where p=q=3. Layer thicknesses are optimized in a way that the peaks are positioned in RGB bands whereas, maximum FR and minimum loss are retained for each peak. Finalized thicknesses are in the order of 50, 100, and 110 nm for H, L, and D, respectively, conceding an overall thickness smaller than 1.5 µm. Using thin MO layers allows for reducing the total energy requirement for switching a pixel.

The bandgap of the proposed structure starts at the wavelengths about 425 nm and covers the rest of the visible band. The transmission peaks occur at λ=494 nm (blue), 541 nm (green) and 630 nm (red). The attained RGB wavelengths yield good coverage across the chromaticity chart for a full-color display. The comparison between the two graphs in Figure 4.6 indicates that unlike the green and red bands, material loss is substantial in the blue

region, which results in a peak with significantly less transmission. This issue needs to be addressed by synthesizing MO materials with high FoM and low loss in ideal RGB ranges.

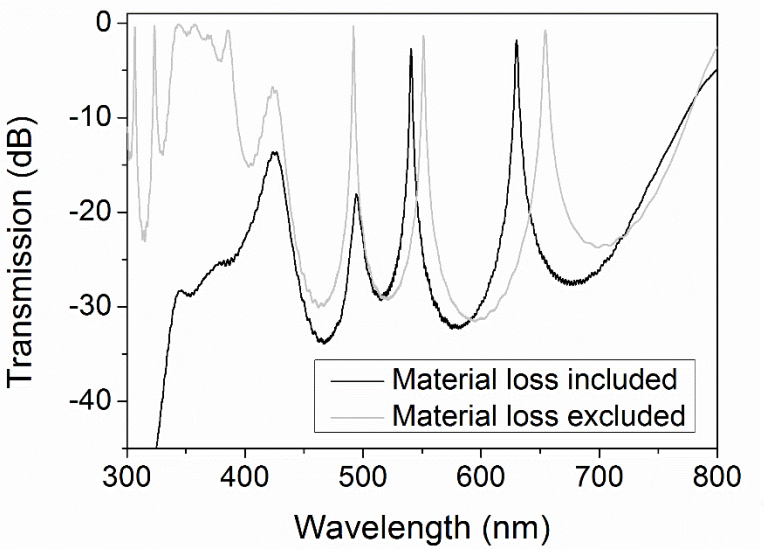

Figure 4. 6. The transmission spectrum of the MPC with $(H/L)^3/(D/L)^3/(H/L)^3$ structure. Black and gray lines represent the calculation with and without considering the MO material loss, respectively.

Figure 4.7. shows how the optical and MO performance of three-defect MPC with different numbers of mirror bilayers. Rotations larger than 80º are feasible using 6 bilayer sets in the Bragg mirrors. Considering the trade-off between Faraday rotation and transmission, the structure with 3 bilayers seems to be the optimal choice by enables figures of merit higher than 10 $^{o}.dB^{-1}$ in the green and red band. This optimized structure demonstrates rotation angles of 20º, 55º, and 30º for red, green, and blue wavelengths, leading to the CR values of tan(20)/tan(0.086) = 242.49, tan(55)/tan(0.086) = 951.47, and tan(30)/tan(0.086) = 384.65, respectively. By iteratively reducing the misorientation angle of the polarizer and analyzer, one can achieve higher contrasts.

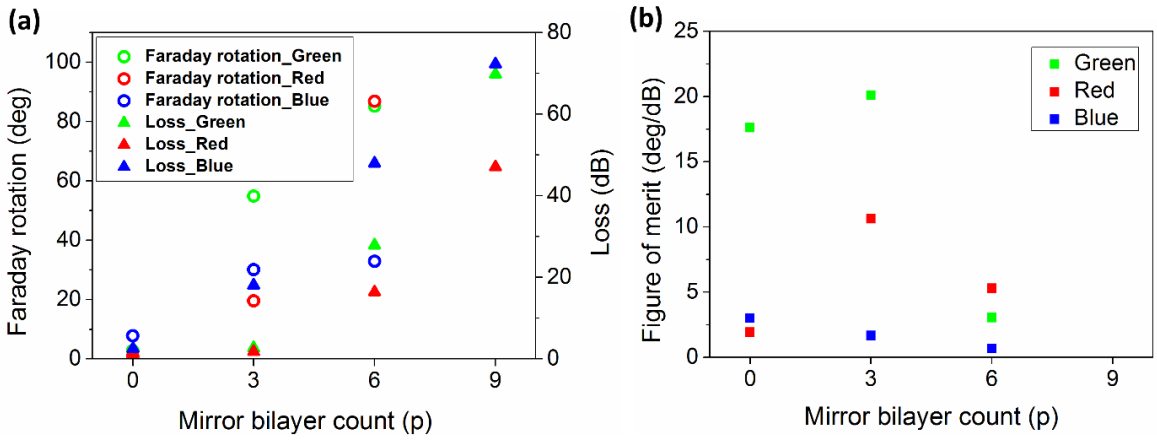

Figure 4. 7. Effect of the number of mirror bilayers on the performance of the three-defect MPC. (a) Faraday rotation, loss, and (b) figure of merit calculated for the three-defect MPC with $(H/L)^p/(D/L)^3/(H/L)^p$ structure, at its resonance peaks around λ=494 nm (blue), λ=541 nm (green) and λ=630 nm (red), shown respectively by blue, green, and red data points on the graphs.

The structural configuration of a photonic crystal might be the most important factor influencing its performance, however, other factors such as index contrast between the periodic mirror layers or layer thicknesses are also determinant [336]. The transmission spectra for the optimized three-defect MPC structure, considering different index contrast between high- and low-index dielectrics, are shown in Figure 4.8. The bandgap and transmission peaks are not evident for the case with zero difference in refractive indices and emerge only by introducing index contrast to the system. Increasing Δn leads to sharper peaks in deeper bandgaps and broadens the bandgap with a shift toward longer wavelengths.

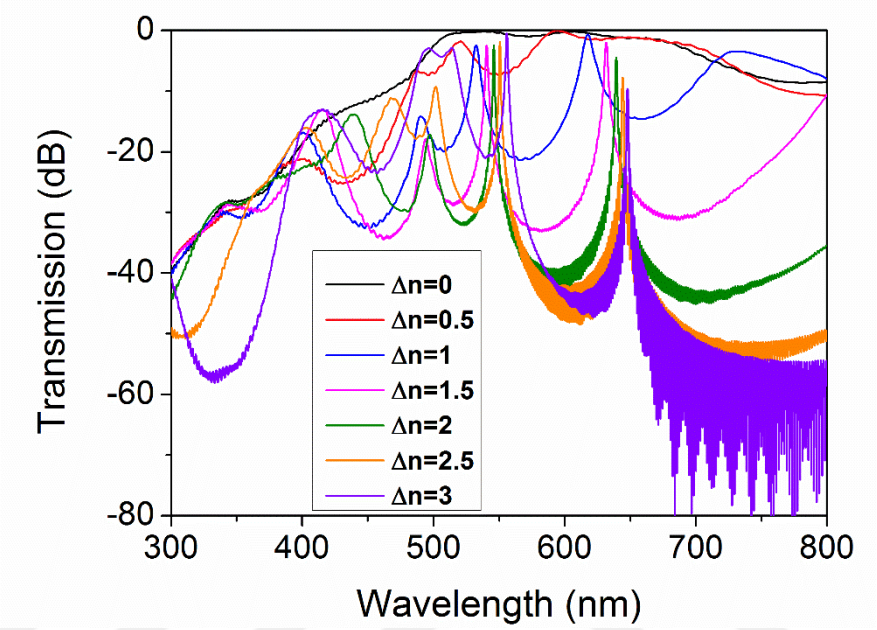

Figure 4. 8. Transmission spectra of the three-defect MPC including three sets of mirror bilayers at each side, for different values of refractive index contrast between high- and low-index dielectrics (Δn).

Figure 4.9 shows FR and loss results of the three-defect MPC as a function of index contrast between the high- and low-index dielectrics, for the attained RGB peaks at λ = 494, 541, and 630 nm. By increasing Δn, it is expected that both FR and loss increase as a result of higher localization. Nonetheless, a maximum is observed around Δn = 1.5, for all three wavelengths. That is because the dielectrics used in the proposed MPC are TiO_2 and SiO_2, which have an index difference of about 1.5 (considering the extraordinary refractive index of rutile) at the RGB wavelengths under study here. So the thicknesses are designed in a way that for such a Δn, resonance peaks of the transmission, and consequently FR are situated at the wavelengths of interest. As a result, for this particular design, the maximum transmission and FR occur around Δn = 1.5 and for other Δn values, the thicknesses of the dielectric layers must be adjusted accordingly to yield the best results. Oscillations observed in the FR spectra at high Δn are due to the large loss, which makes the E-field components that are used for the calculation of FR very small and highly sensitive to calculation errors. As can be seen from

Figure 4.8, for Δn values larger than 1.5, λ = 541 and 630 nm are located at dips of transmission spectra, which causes the high loss level (about 1 dB) for the green and red graphs in Figure 4.9b. Nevertheless, the reduction of loss for Δn > 2 in the blue graph in Figure 4.9b could be explained by the redshift of the band edges with increasing Δn (Figure 4.8), which drives λ = 494 out of the bandgap for higher Δn values.

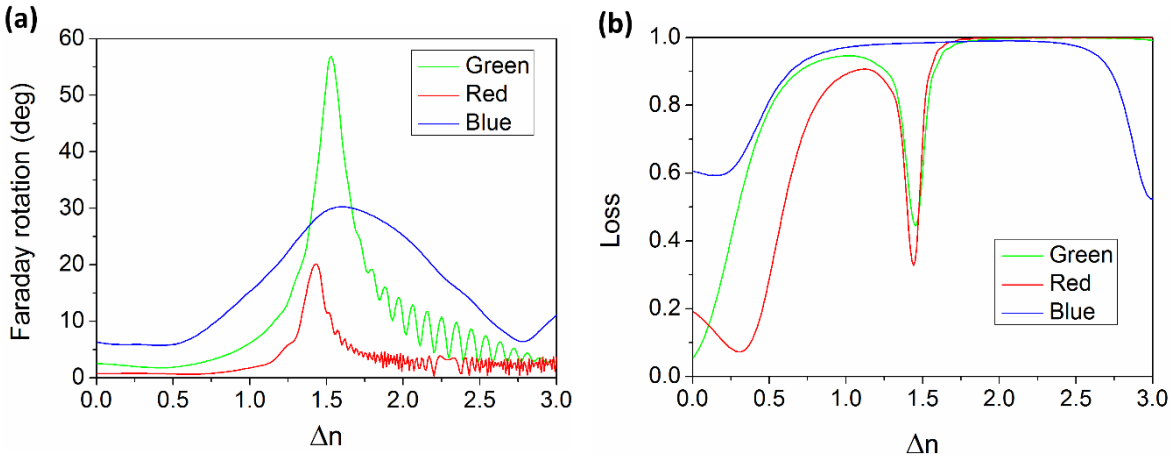

Figure 4. 9. (a) Faraday rotation and (b) loss of the three-defect MPC as a function of the refractive index contrast between high- and low-index dielectric layers. Blue, green, and red curves represent λ=494, 541, and 630 nm, respectively.

The effect of changing layer thicknesses on the resulting Faraday rotation of the three-defect MPC is demonstrated in Figure 4.10. High FR occurs when the phase-matching conditions are met and strong localization exists in MO defects. Comparing the results for blue (Figure 4.10a,b), green (Figure 4.10c,d), and red (Figure 4.10e,f) wavelengths indicates that the highest FR is achievable at the green wavelength, while the off-diagonal element permittivity tensor for Bi:YIG decreases with increasing wavelength and consequently, the material has the highest specific FR at blue wavelength. This fact implies that the structure provides better localization in the green and red bands. Since Bi:YIG has a higher specific FR and lower localization in the blue band, even in the thickness combinations that are not

yielding efficient localization, FR is comparable to the maximum value whereas, at the green and red wavelengths, there is a large difference in the FR for the regions representing high localization and the unlocalized regions. Furthermore, the high-FR sections in the graphs for the red and green wavelengths are much narrower in comparison to blue, which indicates that the sensitivity of the structure to layer thicknesses is higher at those wavelengths. Another point that that can be deduced from Figure 4.10 is that the thickness combination designated for the optimized three-defect MPC in this study, represented by the point (0,0) in the color maps, is situated in high-FR regions at all three wavelengths. This guarantees an MOSLM capable of simultaneous modulation at RGB. There is few nanometer thickness tolerance for the layers in the optimized structure to retain high FR at each wavelength.

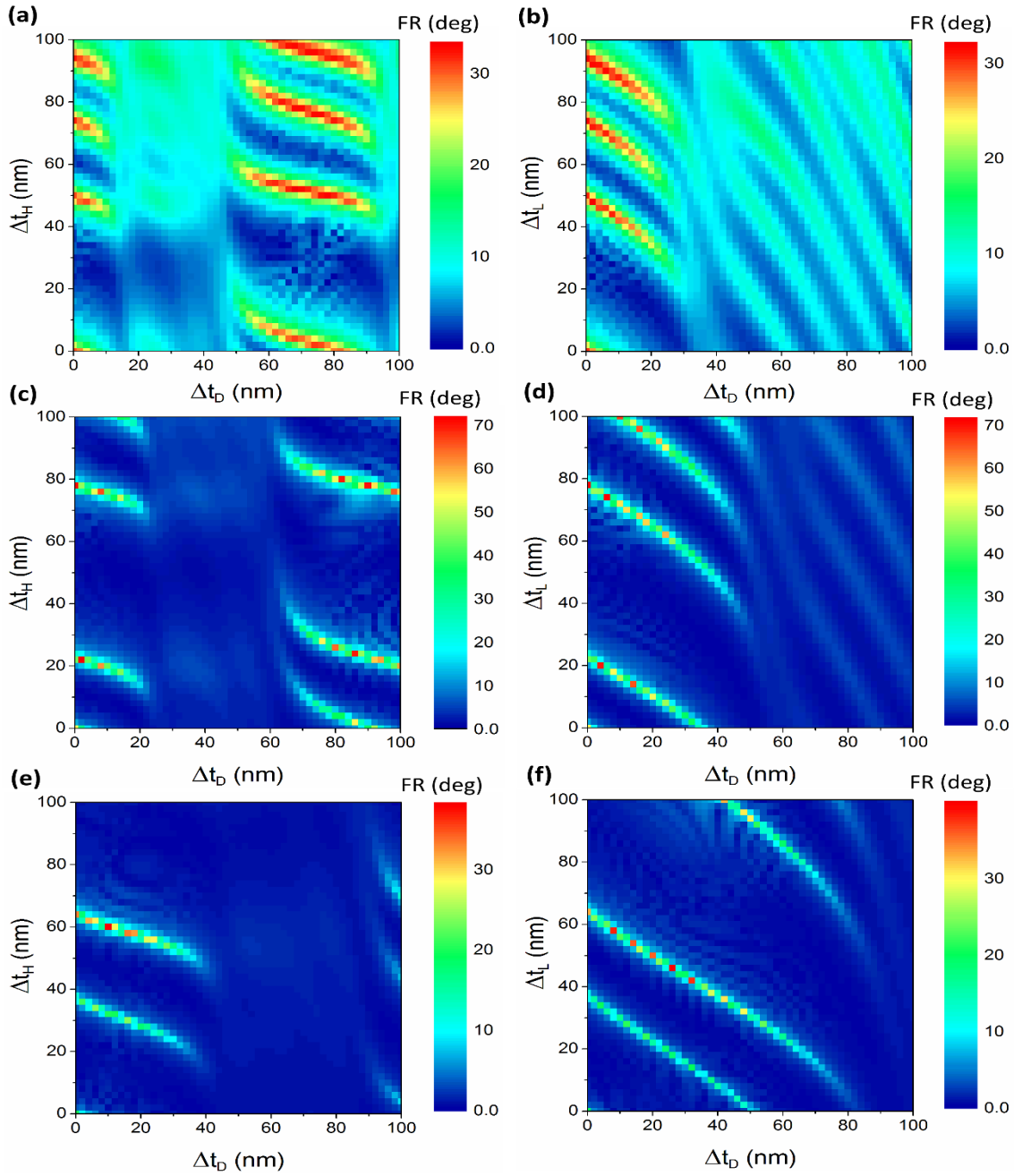

Figure 4. 10. Faraday rotation as a function of variation in layer thicknesses at wavelength of (a,b) 494, (c,d) 541, and (e,f) 630 nm. Δt_H, Δt_L, and Δt_D respectively denote the changes in thicknesses of the high-index, low-index, and defect layers from the primarily designed thicknesses for the three-defect MPC.

Figure 4.11 signifies the influence of MO material FoM affects on the device FoM. The color maps show FoM of the three-defect MPC as a function of specific Faraday rotation and loss of the MO material at blue (Figure 4.11a), green (Figure 4.11b), and red (Figure 4.11c) wavelength. The results indicate that FoM of MPC is more sensitive to loss of the material than its specific FR. In other words, increasing FR of material imposes a gradual enhancement in the FoM of the MPC whereas, increasing the material loss from its minimum value (i.e. considering zero absorption and the loss caused only by reflection) drastically reduces the device FoM. The maximum FoM that can be achieved by the proposed MPC, assuming an MO material with about 10 $^{o}.\mu m^{-1}$ specific FR and almost zero absorption is lower for blue (Figure 4.11a) compared to the other wavelengths. This is due to the weaker localization happening at this wavelength as discussed before. The maximum FoM values at green (Figure 4.11b) and red (Figure 4.11c) wavelength are in the same order while it is notable that reflection loss for red (about 1.5 dB) is lower than that for green (3 dB). Thus, one can conclude that the MPC has better functionality, i.e field localization and FR enhancement, in the green band compared to the other two colors.

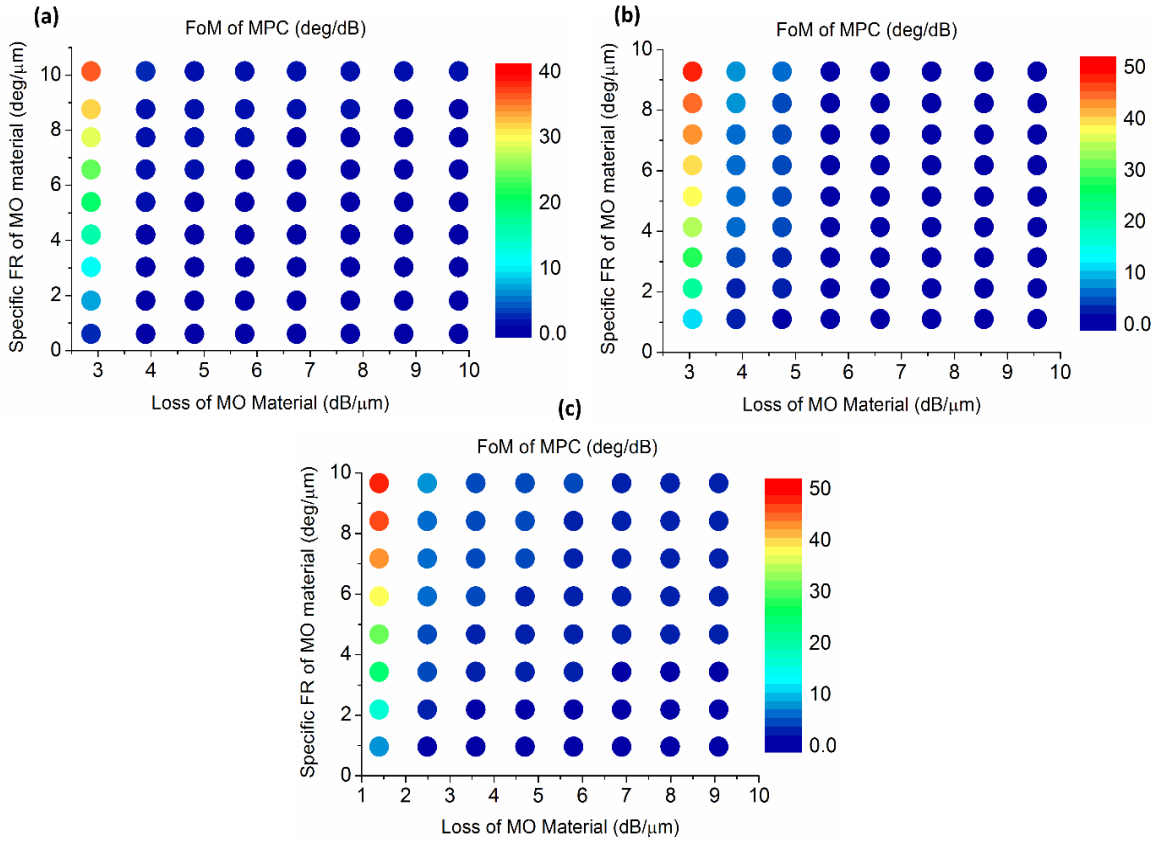

Figure 4. 11. The figure of merit for the three-defect MPC as a function of specific Faraday rotation and loss of the MO material, at the resonance peaks around (a) λ = 494, (b) λ = 541, and (c) λ = 630 nm.

4.3 Summary

MOSLMs are functional optical memory devices that enable ultrafast spatial modulation of light. Besides, novel methods for current- or voltage-based control of magnetization, which provide a low-power electrical switching system, allow researchers to revisit MOSLMs as programmable components for a variety of photonic devices. In this chapter, a three-defect MPC-MOSLM was proposed, which allows for simultaneous enhancement of Faraday rotation and consequently, high-contrast modulation at three fundamental wavelengths of RGB, within the same pixel. An MPC structure with an overall thickness of 1.5 μm was

demonstrated through optimization of the configuration and layer thicknesses, which enables Faraday rotation angles of 20°, 55°, and 30° along with the acceptable loss levels of 2, 3, and 18 dB at RGB wavelengths, respectively. The rotation value at each wavelength becomes double by using magnetization reversal, enabling modulation with $2\theta_F$ = 40°, 110°, and 60° at RGB wavelength, respectively. However, for simultaneous modulation at RGB, we proposed a range of 0-θ_F instead of -θ_F to θ_F, in order to have a common baseline and maximum contrast ratio for all three wavelengths and benefit from a simple operation scheme. Using thin MO films in this design keeps the volume of the MO material small and requires lower switching energy per pixel. Some of the key design rules for MPC-MOSLM with high FoM include:

1. The MPC structure must be comprised of materials with small absorption and the mirror dielectrics must have large enough refractive index contrast (e.g. SiO_2 and TiO_2).
2. For a high-performance MOSLM, MO materials with high FoM, at least a few degrees of Faraday rotation per dB optical loss, are required. The absolute loss value for the MO material must be low enough (less than 2-3 $dB \cdot \mu m^{-1}$) to minimize the absorptive optical losses and heating of the device. For an acceptable signal-to-noise ratio at the output signal, having more than 20° overall rotation is advised.
3. The mirrors layer counts need to be optimized such that optical losses can be kept below 10 or at most 20 dB while ensuring sufficient enhancement of Faraday rotation.
4. Faraday rotation is maximized when index and phase matching conditions are satisfied for the cavity structure with a given index contrast Δn for the mirror dielectrics.
5. The multi-defect configurations need numerical optimization to attain resonance peaks at the desired wavelengths, as photonic modes hybridize in these systems and cause complexities. Examples of such optimizations are provided in Figures 4.4-4.7.
6. The layer thickness tolerances must be taken into consideration in the design of MPCs. As observed in Figure 4.10, in the blue wavelength, the Faraday rotation is not significantly affected as long as the layer thicknesses are within ±5% of the designed thicknesses; nonetheless, the tolerance is mostly limited by the green and red wavelengths, where an

acceptable deviation from the optimum layer thicknesses is below ±2%. Thus, a sensitive control on the deposition process and substantial precision on the thickness measurement is essential.

7. The MOSLM device packaging demands two polarizers (one at the input and the other at the output) in perfectly perpendicular orientations to achieve extinction condition. This allows the contrast ratio to be arbitrarily scalable according to $CR = \tan(\theta_F)/\tan(\theta_p) = \tan(\theta_F)/\tan(0.086) = \tan(\theta_F) \cdot 666.23$. Improved accuracy over the control of polarizer orientations relaxes the Faraday rotation requirements on the MO defect materials.

Following the mentioned criteria, magnetophotonic crystals can significantly enhance Faraday rotation in the visible range, realizing MOSLMs capable of efficient modulation in fundamental red, green, and blue bands, suitable for full-color display systems. MPCs with $(H/L)^p/(D/L)^q/(H/L)^p$ structure, composed of bismuth-substituted yttrium iron garnet as a promising MO material, and TiO_2 and SiO_2 as high- and low-index dielectric for mirror layers, were characterized. I was demonstrated that in addition to RGB modulation, the three-defect MPC provides better performance in terms of achieved FR and FoM. Faraday rotations higher than 20º and figures of merit up to 20 $^{o} \cdot dB^{-1}$ were achieved. Parametric evaluations were performed to investigate the effect of structural variations and material properties on the functionality of such the MPC. The results indicate that material absorption and layer thicknesses must be well controlled to obtain high device figures of merit. Development of novel MO materials with high structural stability, high Faraday rotation, and low optical loss would help in establishing new high-performance MOSLM devices.

Chapter 5

BROADBAND MAGNETOPLASMONIC METASURFACE

Magnetooptical (MO) Faraday effect denotes the rotation in the the polarization plane of light when it passes through a magnetized matter. Faraday effect is proportional to the light path length in the magnetized material and the proportionality coefficient is called specific Faraday rotation:

$$\alpha_F = \frac{\chi}{n} \vec{M}.\vec{k} \tag{5.1}$$

where α_F, χ, n, $\vec{M}$, and $\vec{k}$ respectively show Faraday rotation per unit path length, magnetic susceptibility, refractive index, magnetization vector, and the wavevector [1], [235]. MO Faraday effect enables ultrafast manipulation of light, promising for advancement in a variety of optical components including isolators [27]–[29], circulators [30]–[32], and spatial light modulators [33]–[35], as well as data storage [337]–[339], sensing/imaging systems [18]–[20], and growing field of spintronics [238], [340]. However, the specific Faraday rotation is generally small, which causes limitation in the practical applications and development of miniaturized MO devices [306]. Therefore, enhancing Faraday effect has become a research interest and different approaches have been reported for this purpose, which include use of plasmonic particles in suspension [96], [341], magnetoplasmonic nanoparticles in core-shell arrangement [6], [123], magnetophotonic [23], [71], [177] and magnetoplasmonic crystals [342]–[344], graphene infiltration [176], and the optical analog of electromagnetically induced absorption [181].

A novel approach in enhancement of MO effects, mainly in the visible and near-infrared band, is offered by metasurfaces, which are generally composed of two-dimensional arrays of nanoantennas on a surface, which have subwavelength intervals [345], [346]. In the case

of metallic antennas that enable excitation of surface plasmon polaritons (SPPs), the structure is called a plasmonic metasurface [347]–[349] and different phenomena can be involved in the enhancement mechanism. SPPs are coherent fields generated by oscillations of conduction electrons in the metal-dielectric interface and have a mixed nature of both electromagnetic (EM) waves and surface charges. SPPs propagate along the metal-dielectric interface, being damped by Joule heating and radiative emission, and showing evanescent decay in the perpendicular direction. Such a phenomenon confines the EM waves around the metal-dielectric interface, in the length scales as small as the diffraction limit ($\sim\lambda_0/2n$).

A plasmonic metasurface with MO dielectric, named as magnetoplasmonic metasurface, enables localization and confinement of EM wave inside the MO medium, which increases the light-matter interactions and results in remarkable enhancement of MO effects. However, the resonant character of plasmonic phenomena generally leads to a narrowband enhancement, limiting the applications [183], [350]–[354]. Recently, Kalish et al. [355] used quasiperiodic plasmonic structures to demonstrate multiband enhancement of transverse magnetooptical Kerr effect (TMOKE) using. Pappas et al. [356] embedded gold nanoparticles into the Bi-substituted yttrium iron garnet (Bi:YIG) and accomplished enhancement of the longitudinal magnetooptical Kerr effect (LMOKE) in a relatively wide spectral band, 600-750 nm. Nonetheless, enhancing the Faraday effect that has the highest application potential in practical devices, in a broad wavelength range has not been reported yet.

In this chapter, a magnetoplasmonic metasurface composed of an array of Au nanoantennas on a Bi:YIG film is demonstrated, which significantly enhances the Faraday effect in a broad near-IR range. The proposed structure provides for the incident light to experience different periodic distances. As a result, multiple overlapping resonances appear, leading to a broadband response. First, a comparison of the transmission (T) and Faraday rotation (FR) spectra for the proposed metasurface, a bare Bi:YIG film, and the Bi:YIG film with a plain gold film on top is presented. Next, the mode distribution at the wavelengths related to the peaks and dips of the spectra is studied and the physical cause of the

enhancement in FR is discussed. It is also investigated how different parameters, including the width and thickness of the plasmonic nanoantennas, array periodicity, and polarization of the incident light affect the T and FR spectra. The viability of active reconfiguration is discussed and finally, magnetoplasmonic design guidelines are presented.

5.1 Structure

The magnetoplasmonic metasurface proposed here is composed of a 10-nm thick Bi:YIG film on a glass substrate, which has a 2D array of Au nanoantennas on top, as illustrated in Figure 5.1. Au is a noble metal with low optical absorption and Ohmic losses, offering efficient plasmonic properties [357] and Bi:YIG is an MO material that provides large MO effects in relatively small magnetic fields [316].

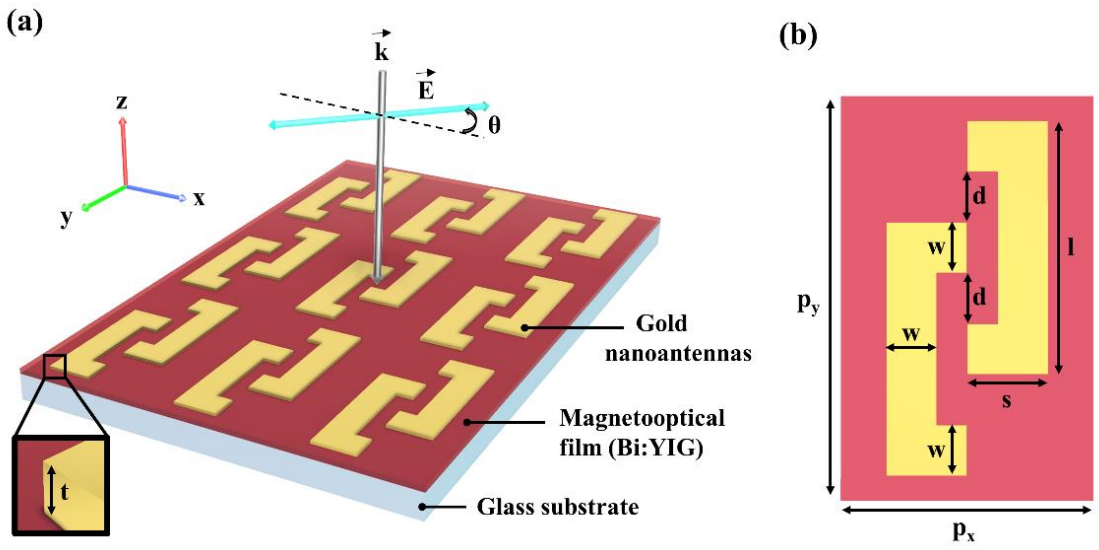

Figure 5. 1. (a) Schematic layout of the proposed magnetoplasmonic metasurface which is composed of a 2D periodic array of gold nanoantennas on 10-nm thick Bi:YIG film deposited on a glass substrate. (b) Top view of a unit cell in the periodic structure. The geometric parameters **l** = 250, **s** = 80, and **d** = 50 nm have fixed values all over the study. The widths (**w**) and thickness (**t**) of the nanoantennas, and the unit cell period in x and y directions ($\mathbf{p_x}$ and $\mathbf{p_y}$) are initially considered to be 50, 5, 250, and 450 nm, respectively, however, the effect of changing these geometrical variables on the

performance of the metasurface is studied. The incident light is primarily assumed to be x-polarized (**θ** = 0), but polarization variation is also investigated as a mechanism for tuning the response of the magnetoplasmonic metasurface.

5.2 Theory

The interaction of light with plasmonic structures involves oscillations of conduction electron density, which are denoted as surface plasmons (SPs). Considering a plain metallic film in contact with a dielectric, the SPs propagate on the interface with a wave vector of magnitude k_{SP}:

$$k_{SP} = k_0 + \sqrt{\frac{\varepsilon_M \varepsilon_D}{\varepsilon_M + \varepsilon_D}} \tag{5.2}$$

where k_0 is the magnitude of the wavevector in free space, and ε_M and ε_D are the relative permittivities of the metal and the dielectric, respectively. According to equation 5.2, k_{SP} has a value greater than k_0, and since the momentum is proportional to the wavevector (de Broglie relation: $\vec{p} = \hbar\vec{k}$), SPs have higher momenta than the free space photons at a given energy. Hence, for efficient excitation and coupling light to SPs leading to the formation of surface plasmon polaritons (SPPs), a system like a prism, gratings, or isolated holes must be used to match the momenta [354], [358].

In a periodic plasmonic structure, when SPPs are excited, several complex scenarios may arise based on the conditions of the structure in the boundaries of the unit cell. In 1D and 2D plasmonic gratings, where the metal-dielectric interfaces are continuous at boundaries of the unit cell, a collective radiative effect known as SPP-Bloch wave (SPP-Bw) mode is probable. Bragg coupling condition states that SPP-Bw mode is excited when:

$$\vec{k} = \vec{k}_{\parallel} + \vec{G} \tag{5.3}$$

where $\vec{k}_{\parallel}$ and $\vec{G}$ are the in-plane wavevector of the incident light and the reciprocal lattice vector, respectively.

In a plasmonic metasurface consisted of periodically arranged discrete nanoantennas that have large dielectric intervals, a collective lattice plasmon mode is formed due to the scattering from the nanoantennas array, where the diffractive coupling between SPPs has a mediating role. In such a configuration, the neighboring antennas collect the optical energy scattered by an individual antenna, which results in a collective lattice plasmon rather than a free-space decay of light. The lattice plasmon mode could indeed be recognized as a sort of surface Bloch mode that is consisted of many Bloch harmonics arisen by the array. Bloch's theorem defines the in-plane wavevector of a diffraction order {m,n} in a rectangular 2D array as:

$$\vec{k}_{m,n} = \vec{k}_0 \sin\varphi + m\frac{2\pi}{p_1}\vec{u}_1 + n\frac{2\pi}{p_2}\vec{u}_2 \tag{5.4}$$

where $\vec{k}_0$ is the wavevector in free-space, φ is the angle of incidence, and p_1 and p_2 are the array pitches in the unit vector directions of the array, $\vec{u}_1$ and $\vec{u}_2$, respectively. Rayleigh's anomaly (RA) happens when the scattered radiation has all its momentum parallel to the array plane, i.e. $|\vec{k}_{m,n}| = k_0$, and no normal component remains for the wavevector. By such a phenomenon, the scattered fields are converted to grazing waves that which could associate with the SPPs and create SPP-RA modes. Although no resonant behavior is entailed in RA, the SPP-RA coupling could result in sharp resonances that enable an enhancement mechanism for SPP modes. Such hybridized resonant features are named surface lattice resonances (SLRs).

Hybridizing plasmonics with the guided modes offers another mechanism to enhance the SPP modes, which necessitates proximity plasmonic nanoantennas with waveguiding structures. In other words, if the dielectric layer in a plasmonic metasurface supports waveguiding modes, the antenna array can couple the light into guiding modes in addition to the plasmonic modes. These couplers can also couple the light out of the waveguide to the free space, which causes them to be called as leaky or quasi-guided modes. SLRs are favored with large plasmonic structures and when the surrounding environment is a homogeneous

dielectric, whereas the quasi-guided modes involve a waveguide element with a refractive index larger than the surrounding [350], [357], [359], [360].

In summary, when the plasmonic and photonic modes overlap spectrally and spatially, strong hybridized modes are created that combine deep subwavelength localization and pronounced light-matter interactions with long-range characteristic of the wave guiding and extend of modal volume over the film plane. Such plasmo-photonic modes allow for strong resonances that are tunable by geometry, lattice parameters, and excitation conditions, and can be used for improving the optical and magnetooptical performance of magnetoplasmonic metasurfaces.

5.3 Modeling and optimization

In this section, the results on the broadband enhancement of Faraday rotation using the magnetoplasmonic metasurfaces and a systematic investigation of the origin of such enhancement are presented. 3D FDTD simulations are used for calculation of the optical and MO response of the magnetoplasmonic metasurface. The optical constants for gold and glass (SiO_2) are adapted from Johnson and Christy [361] and Palik [362], respectively. Bi:YIG is defined by its permittivity tensor elements that generally show spectral dispersion. The average values of $\varepsilon_{xx}= 5.5 + 0.0025i$ and $\varepsilon_{xy}= (1 - 0.15i) \times 10^{-2}$ [352], [353], [363]–[365] are used in this study.

In Figure 5.2 the T and FR spectra for a bare Bi:YIG film, the Bi:YIG film covered by a plain gold layer, and the proposed magnetoplasmonic metasurface, all on glass substrates and respectively shown by black, blue, and red lines, are compared. The thickness of the gold layer is considered to be equal to the thickness of the nanoantennas, $\mathbf{t}$ = 5 nm. Other geometric variables are $\mathbf{w}$ = 50 nm, $\mathbf{p_x}$ = 250 nm, and $\mathbf{p_y}$ = 400 nm, and x-polarized ($\boldsymbol{\theta}$ = 0º) incident light is applied for the calculations reported in this figure. No significant changes are observed in the transmission of the Bi:YIG film in the wavelength range of 600-1600 nm, while transmission of the Bi:YIG film covered by a gold layer shows an almost linear reduction with wavelength and the magnetoplasmonic metasurface displays prominent

resonant features in this range (Figure 5.2a). Comparison of the FR spectra (Figure 5.2b) indicates that FR of the bare Bi:YIG film is negligible in comparison to the magnetoplasmonic metasurface, and addition of a plain Au layer to the Bi:YIG film shows only slight improvement of FR for $\lambda < 1400$ nm, as magnified in Figure 5.2c. FR of the Bi:YIG film is smaller than 0.02º in the range of interest, hwever, rotation values up to 6.5º are attainable by the proposed metasurface.

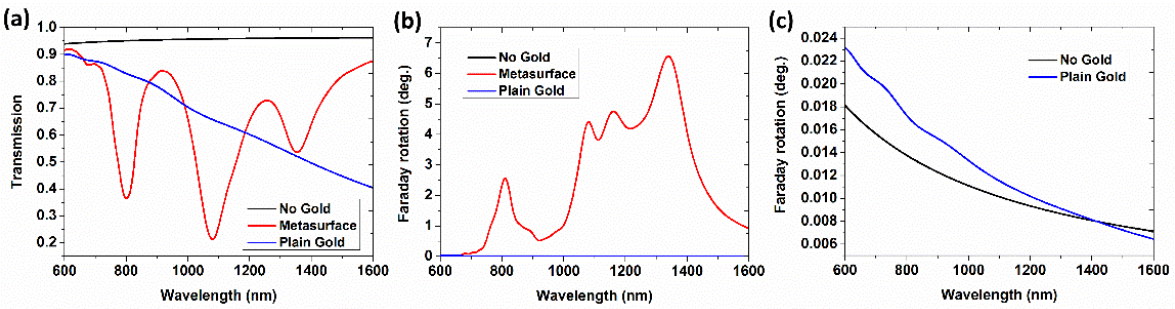

Figure 5. 2. (a) Transmission and (b) Faraday rotation spectra for a 10-nm thick Bi:YIG film (black), the magnetoplasmonic metasurface comprised of 10-nm thick Bi:YIG film and 5-nm thick plasmonic structures with geometric parameters of $\mathbf{w} = 50$, $\mathbf{p_x} = 250$, and $\mathbf{p_y} = 400$ (red), and a 10-nm thick Bi:YIG film covered with a 5-nm thick gold film on top (blue), all on glass substrates. (c) Magnification of part (b) for small rotation angles. The polarization of the light source is considered to be in the x direction ($\boldsymbol{\theta} = 0^{o}$) for these calculations.

Since the proposed metasurface has dissimilar periodic distances in its structure, it leads to multiple resonant peaks that overlap and allow for enhancement of FR in a wide wavelength range. The FR peaks around $\lambda = 800$, 1080, and 1355 nm are correlated with the respective dips in the T spectrum of the magnetoplasmonic metasurface. For the FR peak at $\lambda = 1160$ nm, the associated T dip is enclosed by the stronger adjacent dip at 1080 nm, as can be recognized from the asymmetric shape of this resonance in the transmission spectrum (Figure 5.2a). The proposed magnetoplasmonic metasurface enables few degrees of Faraday rotation in a wide spectral range with a maximum over 6.5º in an overall thickness of 15 nm

(10 nm Bi:YIG film / 5 nm Au antennas), which implies up to three orders of magnitude enhancement in Faraday effect.

For interpreting the resonant features observed for the magnetoplasmonic metasurface, the mode profiles in the main peaks and dips of its spectra are investigated. Figure 5.3 shows the field distribution at the interface of the MO film with the plasmonic structures, for different wavelengths. The electric fields shown in the mode profiles are normalized with respect to the incident field, $|E/E_0|$. At $\lambda = 680$ nm, a minor T dip correlated with a minute FR peak are observed in the spectra, and the unit cell profile shows propagating modes, most pronouncedly along the shorter edges of the gold antennas, and the field enhancement factor ($|E/E_0|$) is mostly below 10 (Figure 5.3a). At $\lambda = 800$ nm, SPPs mainly propagate along the longer edges of the plasmonic structures (Figure 5.3b), besides the localization below the gold antennas. At $\lambda = 915$ nm, the intensity of propagating surface plasmon resonance (PSPR) mode weakens (Figure 5.3c). The maximum field enhancement in Figure 5.3c is similar to that in Figure 5.3b (about 28) but the large field is distributed in a vaster area at $\lambda = 800$ nm, which brings about a superior net enhancement at this wavelength represented by a peak in FR spectrum, whereas $\lambda = 915$ is situated in a dip position. At $\lambda = 1080$ and 1255 nm, the surface plasmons are mainly confined in the structure corners (Figure 5.3d,e). These localized surface plasmon resonances (LSPRs) induce strong light-matter interactions that enforce significant enhancement of FR. Higher field enhancement observed in Figure 5.3d compared to Figure 5.3e leads to a peak position at 1080 nm and a relative decline at 1255 nm, still with a high rotation angle. Coexistence of PSPR and LSPR modes at $\lambda = 1355$ nm (Figure 5.3f) leads to the maximum FR at this wavelength although the maximum enhancement of E field is not related to this wavelength.

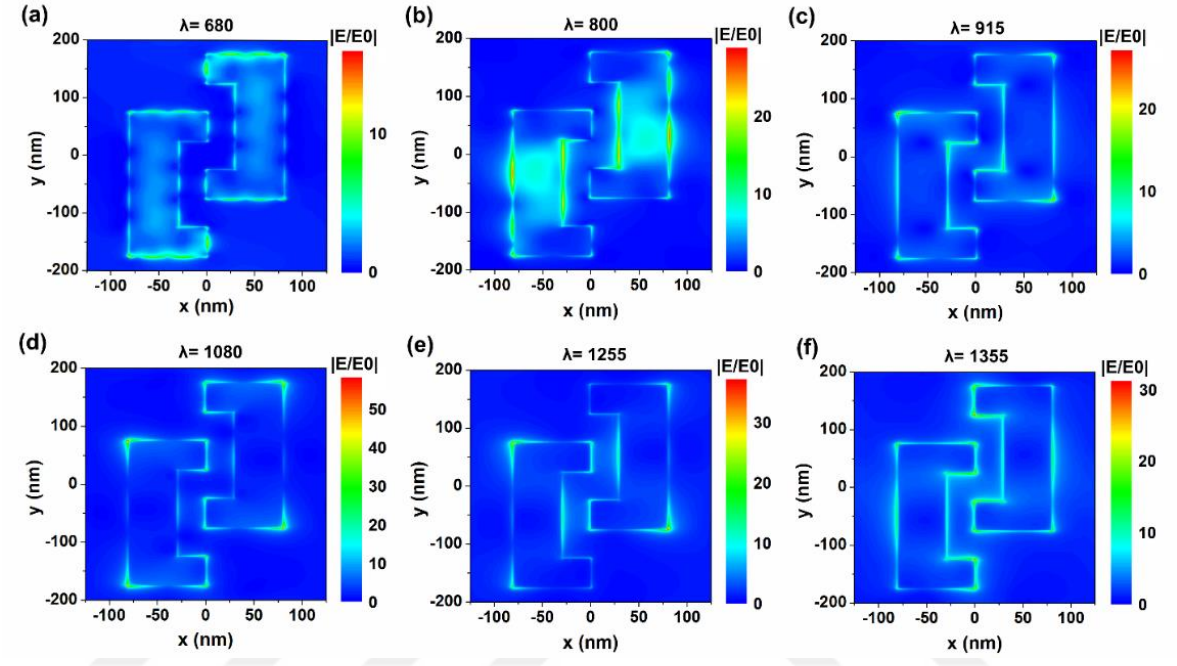

Figure 5. 3. The mode profile in a structural unit cell, at different wavelengths of (a) λ= 680 nm, (b) λ= 800 nm, (c) λ= 915 nm, (d) λ= 1080 nm, (e) λ= 1255 nm, and (f) λ= 1355 nm. The field distribution is calculated in the xy plane at the interface of the gold nanoantennas and the Bi:YIG film. The color bars represent the electric field normalized by the incident field, $|E/E_0|$.

The effect of antennas' geometry on the optical and MO response of the proposed metasurface is explored in Figure 5.4. Nanoantennas having larger width (**w**) show a lower transmission and improved FR, in addition to a redshift in the spectra (Figure 5.4a,b). Giant rotation angles reaching over 20º are achieved by the metasurface with **w** = 70 nm. As depicted in Figure 5.4c,d, nanoantennas with larger thickness (**t**) considerably blueshift the spectra while similarly reducing the transmission and increasing the FR. Thicknesses smaller than 5 nm show no prominent FR peak in the studied band. Sharper peaks and narrow enhancement range are observed by increasing **t**. Both **w** and **t** could be utilized as means of adjusting the operational wavelengths, however, the positions of peaks are more sensitive to the variation of **t**. Considering the role of each geometric parameter, the magnetoplasmonic metasurface can be optimized in accordance with application-based requirements and

limitations for T and FR. According to the results presented in Figure 5.4, for applications demanding broadband operational range, plasmonic structures with large **w** and small **t** are recommended.

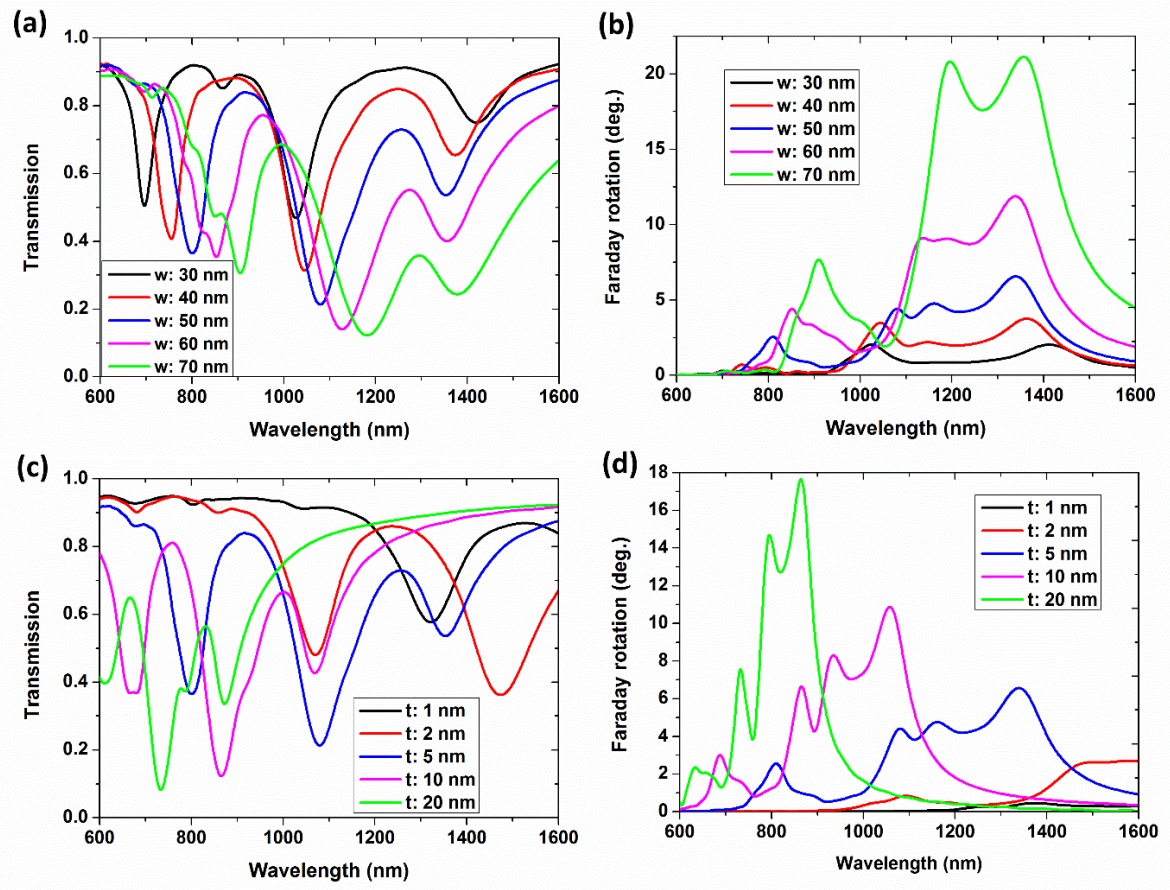

Figure 5. 4. Effect of the (a,b) width and (c,d) thickness of the gold nanoantennas on the optical and magnetooptical responses of the magnetoplasmonic metasurface. The thickness of the nanoantennas is considered to be 5 nm in parts (a,b) and the width is considered to be 50 nm in parts (c,d).

For the metasurface with **w** = 70 nm, three distinctive peaks are recognized in Figure 5.4b. The resonances around λ = 900 and 1200 nm that shift towards smaller wavelengths by

decreasing the size of plasmonic structures can be related to the SPP modes. The resonance around $\lambda = 1350$ nm does not show a meaningful spectral shift by the change of antenna size and can be assigned to the photonic modes. Here, for nanoantennas of 5 nm thickness, a strong coupling between the plasmonic and photonic modes is not observed. Similar behavior is observed for thicknesses smaller than 5 nm in Figure 5.4d, however, for higher thicknesses, a pronounced coupling between the modes is present and all the resonances shift considerably with the change in the antenna sizes. Such a strong coupling leads to sharp resonances and enables up to 18º FR for antennas with $\mathbf{w} = 50$ nm.

In Figure 5.5, the influence of structure periodicity on the performance of the magnetoplasmonic metasurface is investigated. Increasing the period of the plasmonic structures in the x direction ($\mathbf{p_x}$) results in better transmission but smaller FR (Figure 5.5a,b). Increasing the period in the y direction ($\mathbf{p_y}$) has a similar consequence with smaller effect (Figure 5.5c,d). In contrast to the antenna geometry that provides a tool to manipulate the wavelength and intensity of the resonances, periodicity does not impose a noticeable modification in the spectrum shape or peak positions. Thus, to enhance the FR with no changes in the operation wavelengths, the best option to reconfigure the plasmonic metasurface would be reduction the array period.

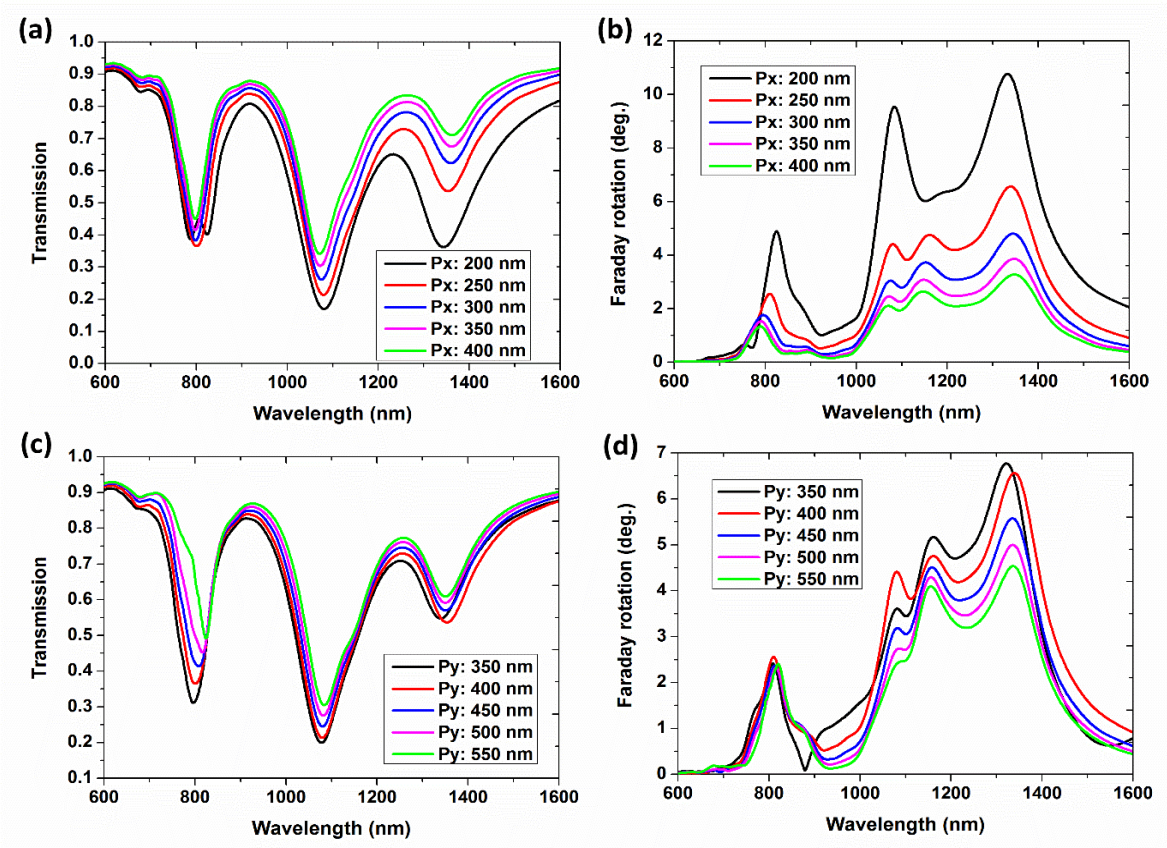

Figure 5. 5. Effect of the periodicity of the structural unit cell in the (a,b) x direction and (c,d) y direction on the optical and magnetooptical responses of the magnetoplasmonic metasurface. The width and thickness of nanoantennas are 50 and 5 nm, respectively. In parts (a,b), $\mathbf{p_y}$ is considered to be 400 nm and in parts (c,d), $\mathbf{p_x}$ is considered to be 250 nm.

Besides the structural parameters, which have to be deliberated before design and fabrication, other parameters exist that can be used for dynamic tuning of the metasurface performance, such as the polarization of the incident light. Figure 5.6 shows how the light polarization affects the metasurface response. By changing the polarization of the incident light from the x direction towards y (increasing $\boldsymbol{\theta}$ from 0º to 90º), a notable improvement in transmission with slight modification in the shape of T spectrum is experienced (Figure 5.6a). According to Figure 5.6b, the magnetoplasmonic metasurface offers broadband enhancement

only for right-angle polarizations (**θ** = 0º and 90º) and at oblique polarization angles, sharp but narrow resonances are observed. In the spectra related to the incident light with oblique polarization, the sign change of the FR with an asymmetric Fano-type line shape is manifested. In such configurations, the structural asymmetries facilitate coupling of discrete non-radiative (dark) modes resulted from SLRs that have finite spectral linewidths, with the normal transmittance through the film (bright mode) that can be considered as a continuum. The interference of dark and bright modes leads to sharp Fano resonances that read to more efficient confinement of light and enable great enhancement of optical fields and FR [350], [353], [359], [360]. Incident light with the polarization of **θ** = 30º empowers rotation angles up to about 20º, retaining the transmission over 40%. Comparing the spectra related to **θ** = 0º and 90º, it is noted that light with y polarization gives rise to somewhat smaller FR with considerably better transmission than x-polarized light. Hence, for the applications with higher transmission demand, y polarization is preferable for the light source to be used with the proposed metasurface.

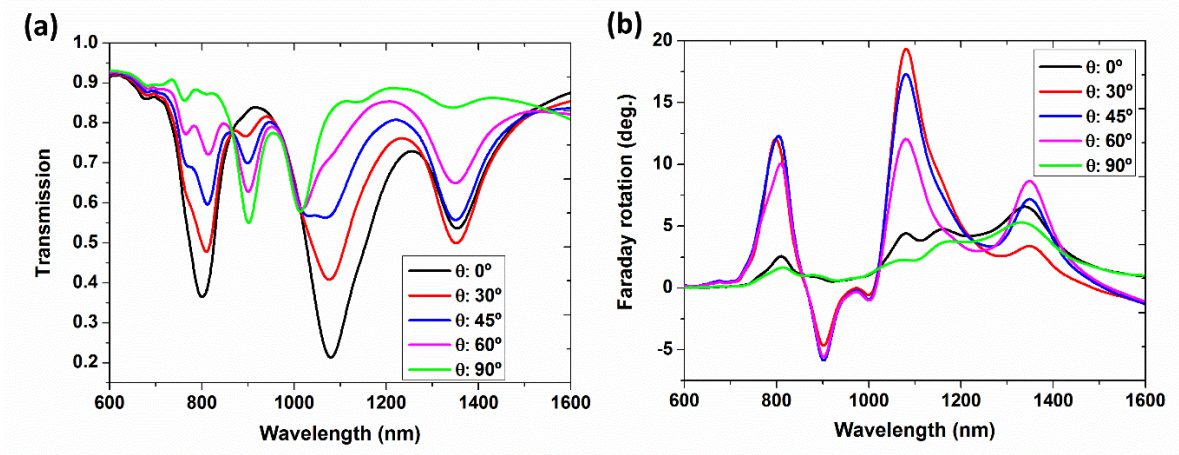

Figure 5. 6. Effect of the polarization of light on (a) transmission and (b) Faraday rotation of the magnetoplasmonic metasurface. **θ** is the angle between the polarization plane of the incident light and the x axis.

Alteration of the external magnetic field provides another means for modification of the MO response of the magnetoplasmonic metasurface. At a given configuration, by changing the external magnetic field, the magnetization of the MO material and hence the off-diagonal element of the permittivity tensor (ε_{xy}) can be controlled, which in turn, governs the magnitude of MO Faraday effect. Switching the direction of magnetization changes the sign of FR, leading to a rotation in opposite angular orientation [366], [367].

5.4 Design guidelines

In this section, guidelines for designing magnetoplasmonic metasurfaces with desired properties are presented, based on the results shown in Figures 5.2-5.6:

1) Operation wavelengths: the operation wavelengths are determined based on the application requirements. An MO material with nonzero and adequately large off-diagonal elements in the permittivity tensor at the operation wavelengths must be chosen. The plasma frequency and the corresponding plasmonic materials are determined by the operation band of plasmons, e.g. gold and doped graphene for THz band [368], [369]. The size of plasmonic antennas has a prominent role in governing the wavelengths of resonance. Increasing the width of antennas causes a shift of the peaks towards bigger λ, whereas the thickness has a contrary effect. To achieve multi- or broadband performance, the antennas' geometry has to comprise different periodic distances. The span of operational band is governed by the geometrical arrangements and particularly the thickness of the antennas.

2) Simultaneous maximization of transmission and MO effect: an efficient magnetoplasmonic metasurface for nonreciprocal photonic devices necessitates materials that have large MO properties but small optical losses. Simultaneous enhancement of Faraday rotation and transmission is essential in acquiring an acceptable signal-to-noise ratio for applications such as sensing, signal processing, and telecommunications. Exploiting both localized and propagating plasmonic modes and also coupling between plasmonic and photonic modes can be exploited for maximum enhancement of FR while restraining the losses. Overlap of multiple resonant features promotes multi/broadband enhancement of MO

effects. The configurational parameters could serve for tailoring and optimization of optical and MO responses of the metasurface. The studied results indicate that optimizing the antennas' thickness and periodicity in the direction parallel to the polarization of the incident light (e.g. $\mathbf{p}_x$ for x-polarized light) makes it possible to notably enhance the FR without a significant reduction of transmission. Furthermore, y-polarized light incident on the proposed metasurface yields significantly better transmission compared to the x-polarized light, although the resultant FR is only slightly smaller.

3) Polarization dependence/independence: for the polarization or angular orientation selectivity/insensitivity of the magnetoplasmonic metasurface, nanoantennas without/with n-fold rotational and mirror symmetries must be designed. Namely, mirror plane or circular symmetries in the nanoantennas' geometry allow for polarization-independent response, while asymmetric structures yield diverse responses depending the polarization of the incident light and could bring about a new class of optical devices that can be regulated by the polarization of light [370].

5.5 Plasmonic metasurfaces for surface-enhance Raman spectroscopy

Enabling strong optical enhancement, plasmonic metasurfaces have attracted significant attention in sensing applications as introduced in section 1.2.3. Particularly, surface-enhanced Raman spectroscopy (SERS) empowers a highly sensitive spectroscopy method by exploiting plasmonic metasurfaces. Raman spectroscopy is a detection technique with advantages such as simplicity of the setup and sample preparation, no vacuum requirement, and provision of more specific information in comparison to the other spectroscopic methods. However, the extremely low intensity of the Raman scattering signal limits the practicality of normal Raman spectroscopy. SERS allows for enhanced sensitivity and selectivity by plasmonic enhancement of the EM field and adsorption of the analyte to the metallic surface which can also lead to signal enhancement through a charge transfer mechanism [371], [372]. In this section, we report on the design, fabrication, and test of different plasmonic structures for SERS purposes.

Figure 5.7 shows the schematics of the unit cells for different designs with a minimum feature size of 1 μm and the resultant E-field enhancement for each design, modeled by 3D FDTD simulations as described in Chapter 2. The plasmonic metasurfaces studied here consist of silver structures on silicon substrates. Optical properties used for Ag and Si are adapted from Johnson and Christy [361] and Palik [362], respectively. The mode profiles (Figure 5.7d-f) in the form of the local electric field normalized with respect to the incident field are calculated in the interface of the metallic structure with the Si substrate, at $\lambda = 633$ nm which is the laser wavelength used for Raman spectroscopy in this study.

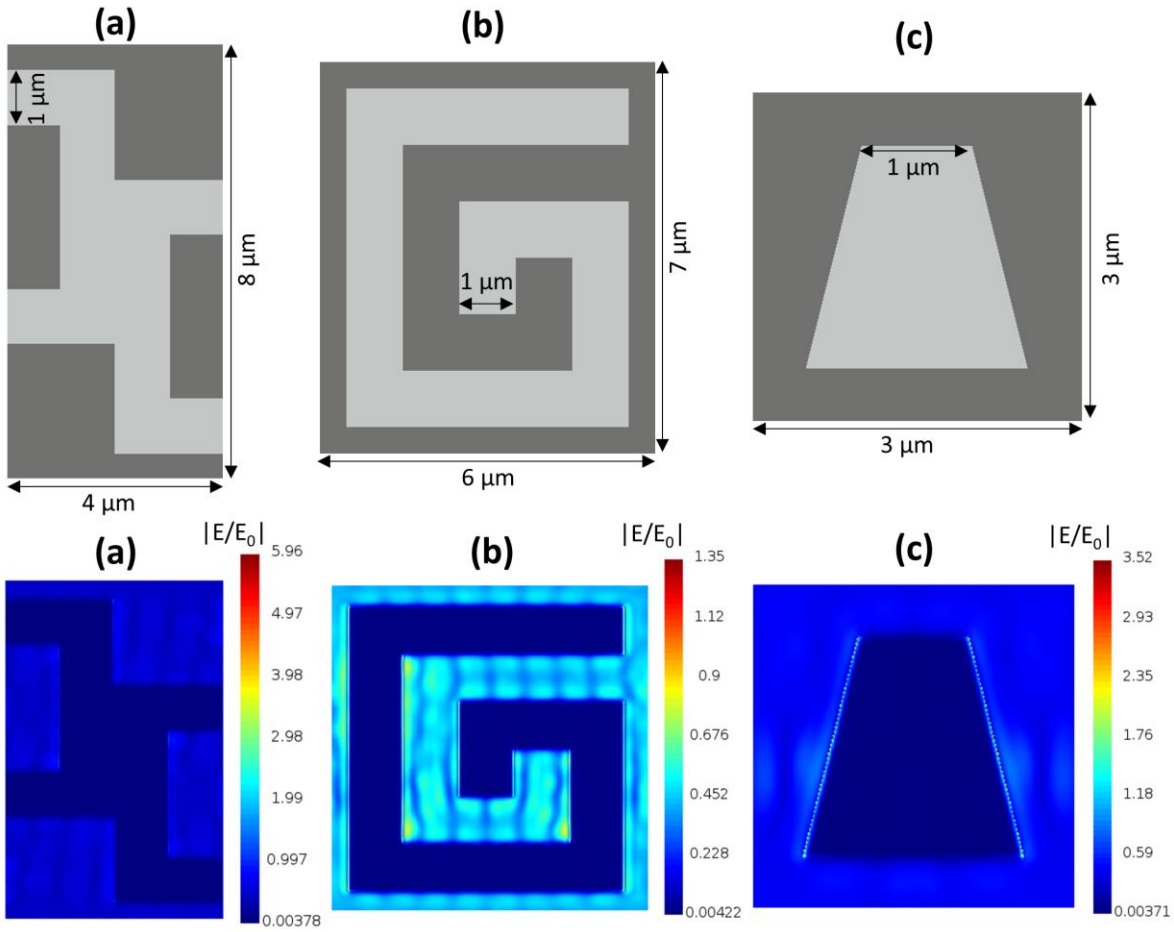

Figure 5. 7. (a-c) Schematic unit cells and (d-f) mode profiles of different plasmonic metasurfaces designed for surface-enhanced Raman spectroscopy.

The designed structures were fabricated using a maskless lithography process explained in detail in Chapter 2. Optical microscope images of the fabricated SERS chips are shown in Figure 5.8. Among the studied plasmonic designs, the double-dent structure (Figure 5.8a) yields the maximum field enhancement at the hotspots as shown in Figure 5.7d. Since the Raman scattering signal enhances in proportion to $|E/E_0|^4$, a signal enhancement with a factor of approximately 800 is expected for this structure. The trapeze shape (Figure 5.8c) shows higher field enhancement in comparison to the maze structure (Figure 5.8b) as observed in Figure 5.7e,f, promising for a greater Raman enhancement.

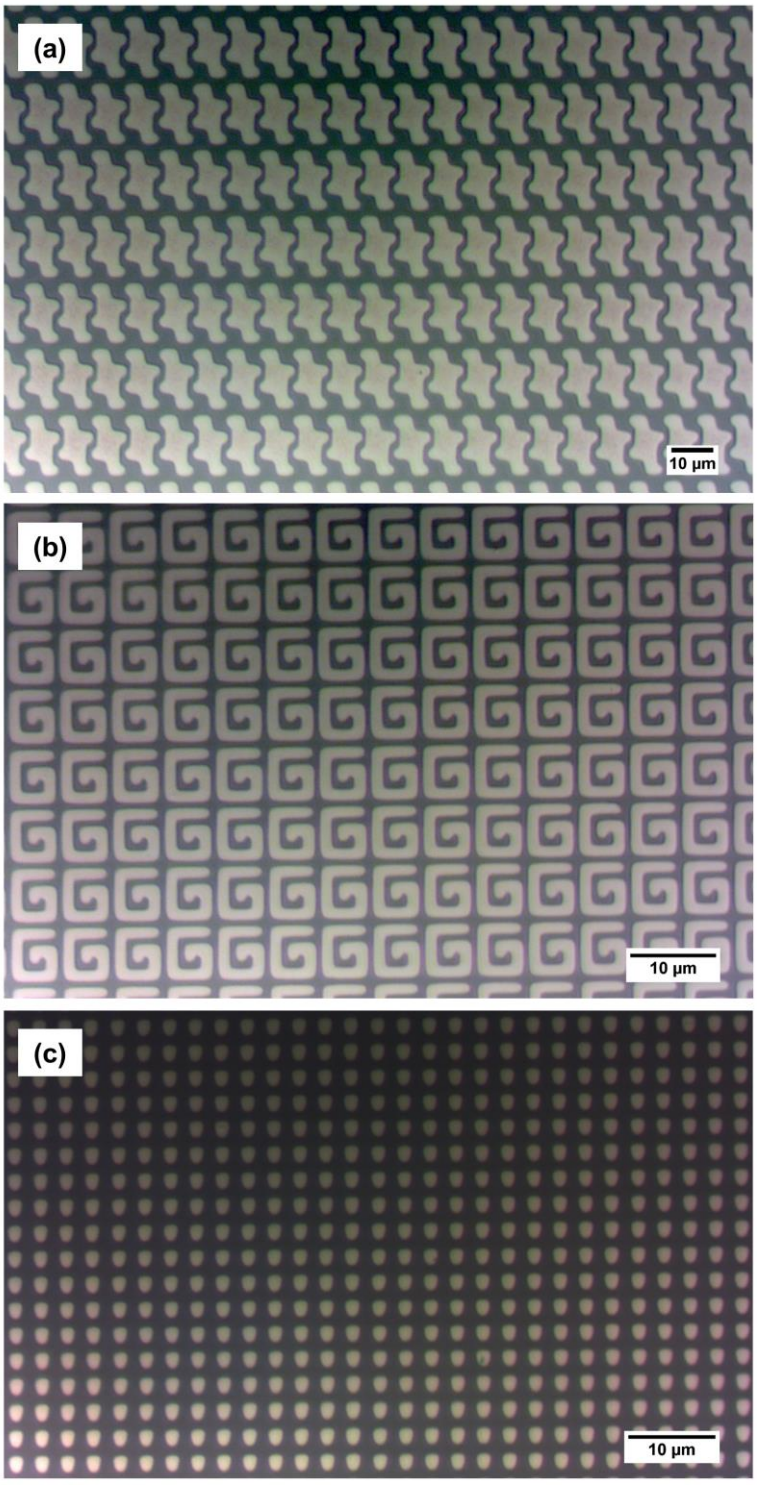

Figure 5. 8. Optical microscope images of the SERS chips.

The performance of the SERS chips is evaluated using an aqueous solution of methylene blue (MB) as the Raman probe. MB is a dye with small fluorescence which has a strong absorption band around 675 nm [373]. Figure 5.9 compares the Raman spectra of MB acquired on the SERS chips with those obtained on a bare Si substrate and the Si substrate coated by a plain silver film.

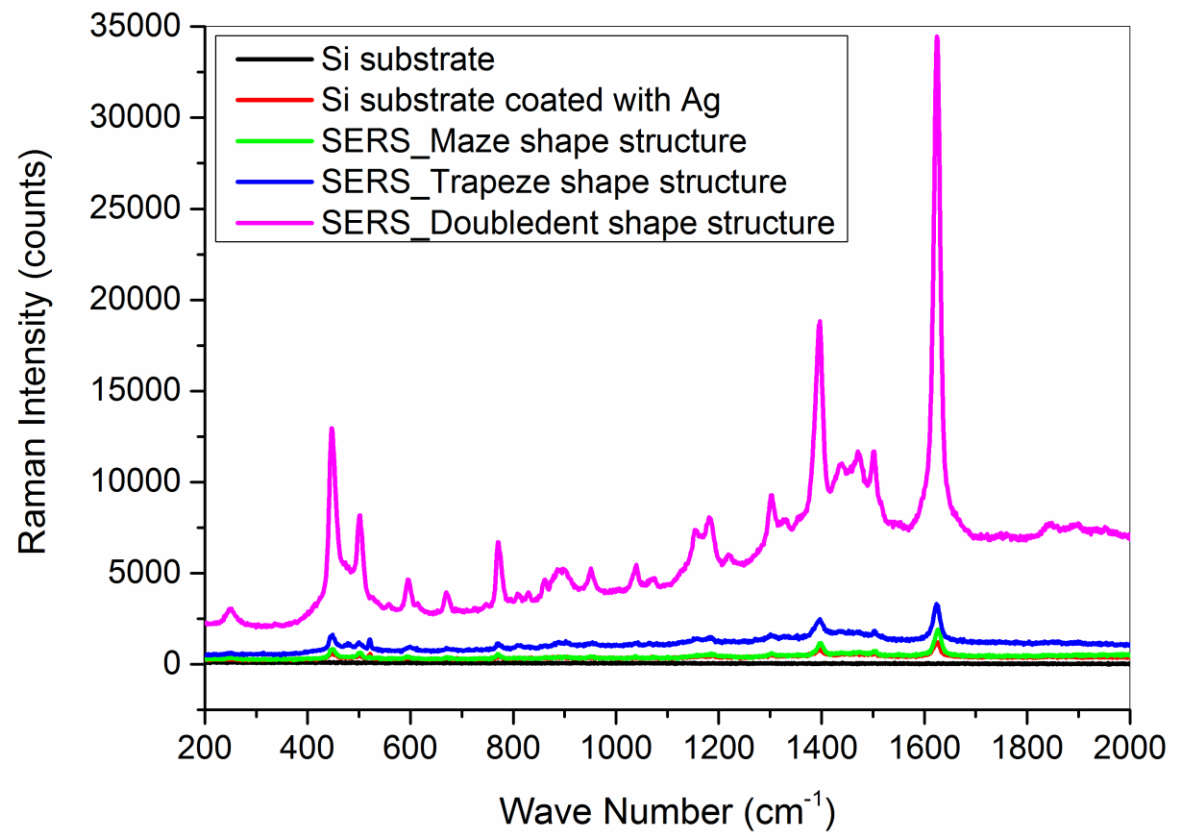

Figure 5. 9. Raman spectra for an aqueous solution of methylene blue acquired on different substrates.

While no spectral features could be detected for MB using Raman spectroscopy on a Si substrate, coating the substrate with a plain Ag film is leads to the appearance of different MB bands. The results are further improved using the SERS chips with different designs.

The SERS chip with the doubledent structure has a remarkably superior performance leading to more than three orders of magnitude enhancement in the intensity of the Raman band at 1624 cm^{-1}, which is related to the ring stretching of the C – C bond. The results can be further improved by the fabrication of features with sharper corners.

5.6 Summary

A magnetoplasmonic metasurface was demonstrated composed of a two-dimensional array of gold nanoantennas on a magnetooptical Bi:YIG film, which remarkably enhances the Faraday effect in a wide near-infrared band. While Faraday rotation in the bare Bi:YIG film is below 0.02º within the studied spectral range of 600-1600 nm, the proposed metasurface enables few degrees of rotation in a broad band, 1000-1400 nm. A maximum Faraday rotation exceeding 6.5º was achieved, indicating about three orders of magnitude enhancement, in a total thickness of 15 nm (comprised of 10 nm thick Bi:YIG film and 5 nm thick gold nanoantennas). The results were further improved by tailoring the geometric parameters and periodicity of the plasmonic structure, leading to rotation angles higher than 20º. Besides the structural parameters that determine the operation wavelengths, the polarization of the incident light and magnetization state of the magnetooptical material were suggested as tools for active tuning of the metasurface response. These tunable magnetoplasmonic metasurfaces could be used for wavelength-selective sensing surfaces, isolators, filters, and other free-space optical signal processing applications. Finally, guidelines based on the investigated results were presented for designing desired magnetoplasmonic metasurfaces and improve the efficiency.

The application of the plasmonic metasurfaces in sensing systems was also discussed in this chapter. Different plasmonic metasurfaces were modeled, fabricated, and tested for surface-enhanced Raman spectroscopy. Remarkable improvement of Raman signal, enabling over three orders of magnitude enhancement in the Raman intensity, was demonstrated.

Chapter 6

CONCLUSIONS AND FUTURE WORK

Magnetooptical spatial light modulators (MOSLMs) were assessed as promising devices for ultrafast and high-resolution modulation of light. The challenges associated with MOSLMs were discussed and novel solutions in terms of materials engineering and device design were presented for achieving functional high-performance MOSLMs.

A thorough comparison of MOSLM prototypes with other types of developed SLM products was performed. Liquid crystal-based products typically have power consumption over 10 W for 60 Hz frame rate and resolutions greater than 1024×1024 (1K×1K) pixels, which are essential requirements in most applications. The working principle of these devices is based on the voltage control of the orientation of liquid crystals in a micron-scale thickness. The thickness of liquid crystal (LC) cannot be reduced due to the number of molecules needed for a π phase shift in modulation. As a result, the power consumption of LC-based devices cannot be reduced significantly without a major change in the switching mechanism or materials. On the other hand, digital micromirror devices (DMDs) with comparable specifications offer lower power consumption by almost an order of magnitude but suffer from disadvantages such as binary modulation (lack of grayscale) and complex fabrication processes. The presence of mechanically moving parts in DMDs may cause reliability issues during the operational lifetime.

Early MOSLM demonstrations show only binary modulation by current/voltage-based magnetization reversal, which might necessitate contribution from an external magnetic field. No mechanical movement is involved in MOSLMs and frame rates exceeding 1 kHz have been demonstrated, overtaking other SLM products. The power requirement for switching pixels in MOSLMs is reported to be mostly below 1 W, however, the device driving

electronics and optics are not included in these reports. The current densities required in MOSLMs need to be further reduced to reach a commercial standard and the external magnetic field needs to be eliminated for avoiding pixel crosstalk. Spin torque switching methods have current demands (10^5 to 10^7 $A.cm^{-2}$) orders of magnitude lower than the magnetic-field-based control, without a need for an external magnetic field. Multiferroics reduce the energy dissipation per unit area per switch to 1-500 $\mu J.cm^{-2}$ by eliminating resistive losses, which is a noteworthy improvement in comparison to that of the current-driven switching (1-10 $mJ.cm^{-2}$). For commercially viable device applications, MOSLMs with a greater number of pixels ($\geq$ 1K×1K) and smaller pixel pitches are required, which can be fulfilled by the latest advances in the micro/nanofabrication techniques. Development of materials with high MO figures of merit at visible and near-infrared bands, the wavelengths and operation bandwidth of the MOSLMs can significantly extend. Implementation of the breakthroughs in materials processing techniques and magnetization switching methods to the MOSLMs motivates further research on this field with the aim of accomplishing nonvolatile, ultrafast, high-resolution, and low-power light modulation.

The major focus of this thesis was on the main issue hindering MOSLMs from industrialization development, i.e. the inherent weakness of the MO effects which limits the pixel contrast and modulation depth. In terms of materials engineering, MO films grown with exclusively different experimental parameters were studied for optimizing the growth conditions. In terms of device design, magnetophotonic crystal (MPC) structures were investigated to be applied in MOSLMs. Furthermore, broadband optical and MO enhancement using magnetoplasmonic metasurfaces were explored for MOSLM and sensing applications.

$Bi_1Y_2Fe_5O_{12}$ (Bi:YIG) thin films were grown by pulsed laser deposition on GGG, SGGG, and quartz substrates, at different temperatures (300-650 °C), oxygen pressures (0.001-0.1 mbar), and pulse repetition rates (10-100 Hz). Epitaxial films were realized on GGG, with the highest crystalline quality being related to the growth parameters of 550-600 °C, 0.05-0.1 mbar, and 50 Hz. Similar experimental conditions including 550-600 °C, 0.1 mbar, and

50 Hz yielded the best epitaxial growth on SGGG substrate. No impurity phases were crystallized in the films grown on GGG and SGGG. Growth on the quartz substrate mostly resulted in polycrystalline Bi:YIG films. For the film grown at 650 °C, a secondary phase (hexagonal $YFeO_3$) with a short-range order was formed in addition to Bi:YIG. Recommended experimental parameters to obtain single-phase and high-quality garnet on quartz substrate include growth temperature of 550-600 °C, 0.05-0.1 mbar O_2 pressure, and pulse rate of 20-50 Hz. All the films grown under different experimental parameters had perfect adhesion and smooth surface, and RMS surface roughness was below 1 nm for the films grown on different substrates. Transmission measurements showed typical garnet spectra for all the films with a band edge around $\lambda = 200$ nm and a band tail extending towards visible and IR range.

MPC structures comprised of alternating high-index (H) and low-index (L) dielectrics and MO defect layers (D) in the format of $(H/L)^p/(D/L)^q/(H/L)^p$ were studied for high-performance MOSLMs. The performance of the MPCs was investigated as a function of mirror bilayer count (p) and the number of defect layers (q). After optimization of the structure and layer thicknesses, a three-defect MPC was proposed, which allows for simultaneous enhancement of Faraday rotation and consequently, high-contrast modulation at three fundamental wavelengths of red, green, and blue (RGB) within a pixel. This MPC enables Faraday rotation angles of 20°, 55°, and 30° with acceptable loss levels of 2, 3, and 18 dB at RGB wavelengths, respectively, leading to figures of merit as high as 20 $^o \cdot dB^{-1}$. Such an RGB MPC-MOSLM is suitable for full-color display systems with an overall thickness of 1.5 μm. The use of MO films with submicron thicknesses in this design keeps the volume of the MO material small and demands lower switching energy per pixel. Parametric evaluation of structural variations and material properties on the MPC performance indicated that material absorption and layer thicknesses must be well controlled to obtain high device figures of merit.

A magnetoplasmonic metasurface composed of a two-dimensional array of gold nanoantennas on a Bi:YIG film was demonstrated capable of remarkable enhancement of

Faraday effect in a wide near-infrared band. The proposed metasurface enables few degrees of Faraday rotation in the wavelength range of 1000-1400 nm, with a maximum exceeding 6.5º while the bare Bi:YIG film shows rotation values smaller than 0.02º within the studied range of 600-1600 nm. Further improvement of the performance was shown by tailoring the geometric parameters and periodicity of the plasmonic structure, leading to rotation angles higher than 20º. Besides the structural parameters that determine the operation wavelengths, the polarization of the incident light and magnetization state of the magnetooptical material were suggested as means of active response tuning. Design guidelines for realizing desired magnetoplasmonic metasurfaces were presented and the applications of plasmonic metasurfaces in sensing systems were discussed. Different plasmonic metasurfaces were modeled, fabricated, and tested for surface-enhanced Raman spectroscopy. Remarkable improvement of Raman signal, enabling over three orders of magnitude enhancement in the Raman intensity, was experimentally demonstrated.

Major progress has been made in the field of magnetooptics, however, there is still plenty of room for implementing the achieved advancements in a device production level and further improvements to obtain functional high-contrast and power-efficient MOSLMs for widespread use. An ideal SLM needs to be capable of a complete amplitude modulation between zero and input light intensity, which necessitates 90º of polarization rotation in the case of MOSLMs. The energy required for switching the pixels in MOSLMs has to be acceptable such that competitive industrialization standards could be met. Any unnecessary power consumption like optical losses and Joule heating from pixel drive electronics should be minimized to provide low-power operation and prevent the problems related to thermal drift. Integration of a 2D array of pixels and addressing electronics must be devised in a way the required spatial resolution for a specific application is provided while avoiding crosstalk between pixels. For holographic imaging and 3D displays, pixel pitches below 1 μm are preferred for compact devices. Although binary modulation meets the needs of simple displays used in calculators, e-readers, electronic labels, etc., more complicated applications including imaging and holography, require analog or multilevel modulation with sufficient

modulation depth (8 bit or more). Amplitude modulation is generally not satisfactory in these applications and full complex modulation is required.

In order to fulfill the above-mentioned requirements and develop the MOSLM as an advanced product for emerging applications, research in the following direction is suggested:

(i) Direct investigation of the microscopic origin of MO effects and explicit understanding of the underlying physics, which allows for the discovery and synthesis of new MO materials in addition to novel approaches for MO enhancement. Such advancements support proceeding towards the achievement of 90º polarization rotation and efficient modulation in a broad spectral range.

(ii) Integration of fast and low-power driving optics and electronics to MOSLMs is another challenge to be addressed. Among the present switching systems, the voltage-driving scheme is more promising due to the elimination of massive Joule heating and power loss associated with current-driving in small structures, in addition to the simplicity of configuration. The exploration of multiferroic materials and structures with strong magnetoelectric coupling becomes an open research area for voltage driving.

(iii) Using the advanced micro/nanofabrication techniques, forming pixels smaller than 1 μm is not a major obstacle on the way of developing high-resolution MOSLMs. However, the scaling of driving electronics to small sizes involves considerable challenges that need to be targeted in future work.

(iv) In terms of modulation type, binary modulation can be performed in principle and has been experimentally demonstrated in MOSLMs but analog or multilevel modulation remains a challenge due to the hysteresis behavior in MO materials. We suggest implementing analog modulation in MOSLMs using minor hysteresis loops or return paths to different remanent states as shown in Figure 6.1. In this approach, different levels of MO signal intensities are achievable by magnetizing the pixels up to different points using the minor loops, instead of full magnetic saturation.

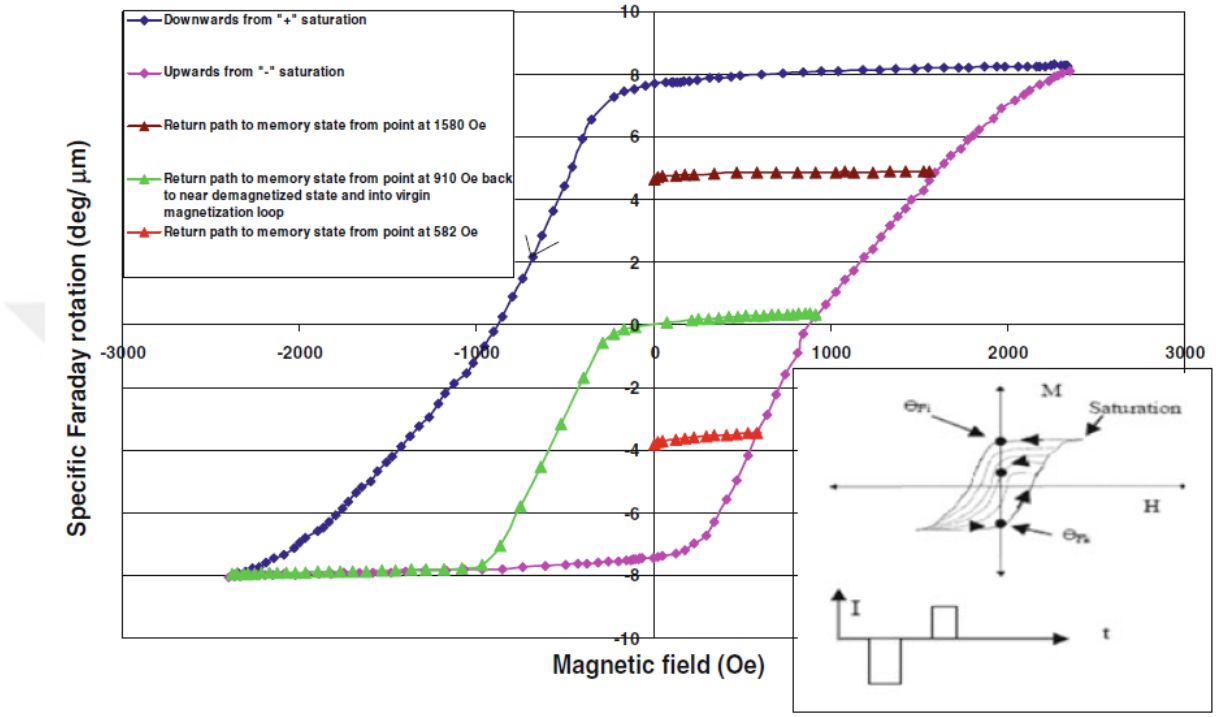

Figure 6. 1. Major and minor Faraday rotation hysteresis loops in a 0.85 µm-thick garnet film grown on a Corning® 1737 glass substrate measured using 532 nm light. The minor loops show the return paths from several different magnetization states. The inset shows a schematic diagram of a magnetic hysteresis loop including some minor loops that allow for control over the remnant states of magnetization using a current pulse modulation scheme [374].

Another approach for this purpose is saturating all the pixels along the hard magnetic axis and then, turning the driving signal (e.g. voltage) off and letting the pixels relax towards the easy axis over time, and stabilize the B-field using pulse width modulation schemes as illustrated in Figure 6.2. Since the MO effects are proportional to magnetization, pixels with different magnetization levels lead to different rotation angles and as a result, different pixel intensities will be obtained. For each pixel, when the magnetization relaxes to a level that corresponds to the desired pixel output intensity, applying pulses of the driving signal can prevent further pixel decay and stabilize its magnetization level. For instance, the MOSLM is first saturated at t = 0 and then, the driving signal is shut off and all pixels start relaxing to

their easy axis orientation. To maintain the magnetization level of a pixel, e.g. pixel A, at a desired value that is proportional to the aimed pixel intensity in a frame, a large enough pulse is applied at $t = \tau_{A1}$ while other pixels which are desired to have lower intensities are left for the decay of magnetization. A similar magnetization control procedure is applied to the rest of the pixels. By further magnetic relaxation, when the pixels reach the desired magnetization states yielding certain output intensities (e.g. pixel B at $t = \tau_{B1}$ and pixel C at $t = \tau_{C1}$), driving signal pulses are applied to maintain their magnetic moments. When the aimed pixels magnetization distribution is completed for the first frame, the optical output is read out (at $t = \tau_{readout1}$). After readout, the whole MOSLM chip is refreshed and pixels are prepared for the next frame. In the second frame, each pixel can adopt an intensity different from the previous frame, and accordingly, time delays for stabilizing magnetization after the start of relaxation (i.e. τ_{A2}, τ_{B2}, and τ_{C2}) would be different from those in the first frame. As a result, analog control of pixel intensities is possible by this method.

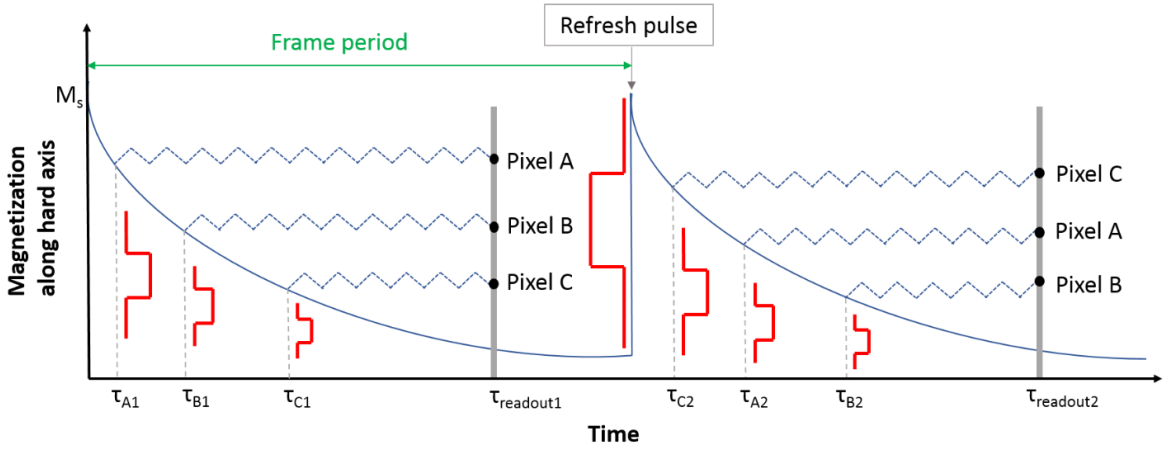

Figure 6. 2. The mechanism suggested for a multilevel modulation in MOSLMs. First, all pixels are magnetically saturated at t = 0 and then, the driving signal (e.g. voltage) is turned off to allow for time-dependent magnetic relaxation of the pixels. For each pixel such as pixel A, when the magnetization reaches the level which corresponds to the desired output optical intensity (at $t = \tau_{A1}$), pulses of the driving signal can be applied to prevent further decay of magnetization and stabilize it at the intended level.

The rest of the pixels are left for further magnetization decay until reaching the levels that yield the desired output intensities (e.g. $t = \tau_{B1}$ for pixel B and $t = \tau_{C1}$ for pixel C), where exposure to pulses of the driving signal maintains their magnetic moments. When the pixel magnetization distribution is completed for the first frame, the optical output is read out (at $t = \tau_{readout1}$) and the procedure continues for the next frames.

(v) Phase or complex modulation using MO materials has not been proven yet. The difference of the refractive indices experienced by left- and right-handed circularly polarized (LHCP and RHCP) light in a magnetized MO material provides a platform to investigate the possibility of phase control and full complex modulation using MOSLMs.

BIBLIOGRAPHY

[1] A. K. Zvezdin and V. A. Kotov, *Modern Magnetooptics and Magnetooptical Materials*. New York: Taylor & Francis Group, 1997.

[2] G. F. Dionne, G. A. Allen, P. R. Haddad, C. A. Ross, and B. Lax, "Circular Polarization and Nonreciprocal Propagation in Magnetic Media," *Lincoln Lab. J.*, vol. 15, no. 2, pp. 323–340, 2005.

[3] D. Chen, "Magneto-Optic Principles, Materials And Applications," *Proc. SPIE*, vol. 0038, pp. 9–15, 1973.

[4] T. Goto, R. Isogai, and M. Inoue, "Para-magneto- and electro-optic microcavities for blue wavelength modulation," *Opt. Express*, vol. 21, no. 17, p. 19648, 2013.

[5] V. I. Belotelov *et al.*, "Enhanced magneto-optical effects in magnetoplasmonic crystals.," *Nat. Nanotechnol.*, vol. 6, pp. 370–376, 2011.

[6] P. K. Jain, Y. Xiao, R. Walsworth, and A. E. Cohen, "Surface Plasmon Resonance Enhanced Magneto-Optics (SuPREMO): Faraday Rotation Enhancement in Gold-Coated Iron Oxide Nanocrystals," *Nano Lett.*, vol. 9, no. 4, pp. 1644–1650, 2009.

[7] P. M. Oppeneer, "Magneto-optical spectroscopy in the valence-band energy regime: relationship to the magnetocrystalline anisotropy," *J. Magn. Magn. Mater.*, vol. 188, no. 3, pp. 275–285, 1998.

[8] W. Reim and J. Schoenes, "Magneto-optical Spectroscopy of f-electron Systems," in *Handbook of Ferromagnetic Materials*, K. H. J. Buschow and E. P. Wohlfarth, Eds. Amsterdam: Elsevier Science Publishers B.V., 1990, pp. 133–236.

[9] V. N. Antonov, L. Uba, S. Uba, A. N. Yaresko, A. Y. Perlov, and V. V. Nemoshkalenko, "Magnetooptical spectroscopy of magnetic multilayers: Theory and experiment (A review)," *Low Temp. Phys.*, vol. 27, no. 6, pp. 425–462, 2001.

[10] G. van der Laan and A. I. Figueroa, "X-ray magnetic circular dichroism - A versatile tool to study magnetism," *Coord. Chem. Rev.*, vol. 277, pp. 95–129, 2014.

[11] A. Rogalev, F. Wilhelm, N. Jaouen, J. Goulon, and J.-P. Kappler, "X-ray Magnetic Circular Dichroism: Historical Perspective and Recent Highlights," in *Magnetism: A Synchrotron Radiation Approach*, E. Beaurepaire, H. Bulou, F. Scheurer, and J. P. Kappler, Eds. Berlin: Springer, 2006, pp. 71–93.

[12] M. L. Baker *et al.*, "X-ray Magnetic Circular Dichroism Investigation of the Electron Transfer Phenomena Responsible for Magnetic Switching in a Cyanide-Bridged [CoFe] Chain," *Inorg. Chem.*, vol. 52, no. 24, pp. 13956–13962, 2013.

[13] F. Fohr, A. A. Serga, T. Schneider, J. Hamrle, and B. Hillebrands, "Phase sensitive Brillouin scattering measurements with a novel magneto-optic modulator," *Rev. Sci. Instrum.*, vol. 80, p. 043903, 2009.

[14] M. H. Kryder, "Magneto-optic recording technology (invited)," *J. Appl. Phys.*, vol. 57, pp. 3913–3918, 1985.

[15] R. Carey, D. M. Newman, and B. W. J. Thomas, "Magneto-optic recording," *J. Phys. D: Appl. Phys.*, vol. 28, pp. 2207–2227, 1995.

[16] T. McDaniel, "Magneto-Optical Data Storage," *Commun. ACM*, vol. 43, no. 11, pp. 57–63, 2000.

[17] D. Jenkins *et al.*, "Advanced optical and magneto-optical recording techniques: A review," *Microsyst. Technol.*, vol. 10, pp. 66–75, 2003.

[18] J. E. Lenz, "A review of magnetic sensors," *Proc. IEEE*, vol. 78, no. 6, pp. 973–989, 1990.

[19] S. Arakelyan *et al.*, "Direct current imaging using a magneto-optical sensor," *Sensors Actuators A*, vol. 238, pp. 397–401, 2016.

[20] G. Zhang, Z. Zhang, Y. Xu, and J. Wang, "High speed magneto-optical imaging system to investigate motion characteristics of arc plasma in enclosed chamber," *Opt. Express*, vol. 26, no. 18, pp. 23156–23166, 2018.

[21] W.-H. Yeh, J. Carriere, and M. Mansuripur, "Polarization microscopy of magnetic domains for magneto-optical disks," *Appl. Opt.*, vol. 38, no. 17, pp. 3749–3758, 1999.

[22] J. McCord, "Progress in magnetic domain observation by advanced magneto-optical

microscopy," *J. Phys. D: Appl. Phys.*, vol. 48, p. 333001, 2015.

[23] T. Yoshimoto *et al.*, "Magnetophotonic crystal with cerium substituted yttrium iron garnet and enhanced Faraday rotation angle," *Opt. Express*, vol. 24, no. 8, pp. 8746–8753, 2016.

[24] Y. K. Kato, R. C. Myers, A. C. Gossard, and D. D. Awschalom, "Observation of the Spin Hall Effect," *Science*, vol. 306, pp. 1910–1913, 2004.

[25] M. Montazeri *et al.*, "Magneto-optical investigation of spin-orbit torques in metallic and insulating magnetic heterostructures," *Nat. Commun.*, vol. 6, p. 8958, 2015.

[26] W. Jiang *et al.*, "Direct observation of the skyrmion Hall effect," *Nat. Phys.*, vol. 13, pp. 162–169, 2017.

[27] H. Takeda and S. John, "Compact optical one-way waveguide isolators for photonic-band-gap microchips," *Phys. Rev. A*, vol. 78, no. 2, p. 023804, 2008.

[28] L. Bi *et al.*, "On-chip optical isolation in monolithically integrated non-reciprocal optical resonators," *Nat. Photonics*, vol. 5, pp. 758–762, 2011.

[29] Y. Zhang *et al.*, "Monolithic integration of broadband optical isolators for polarization-diverse silicon photonics," *Optica*, vol. 6, no. 4, pp. 473–478, 2019.

[30] Z. Wang and S. Fan, "Optical circulators in two-dimensional Magneto-Optical Photonic Crystals," *Opt. Lett.*, vol. 30, no. 15, pp. 1989–1991, 2005.

[31] W. Śmigaj, J. Romero-Vivas, B. Gralak, L. Magdenko, B. Dagens, and M. Vanwolleghem, "Magneto-optical circulator designed for operation in a uniform external magnetic field," *Opt. Lett.*, vol. 35, no. 4, p. 568, 2010.

[32] V. Dmitriev, M. N. Kawakatsu, and F. J. M. de Souza, "Compact three-port optical two-dimensional photonic crystal-based circulator of W-format," *Opt. Lett.*, vol. 37, no. 15, pp. 3192–3194, 2012.

[33] W. E. Ross, D. Psaltis, and R. H. Anderson, "Two-dimensional magneto-optic spatial light modulator for signal processing," *Opt. Eng.*, vol. 22, no. 4, pp. 485–490, 1983.

[34] J. Park, M. Inoue, J. Cho, K. Nishimura, and H. Uchida, "An optical micro-magnetic device: magnetic-spatial light modulator," *Journal of Magnetics*, vol. 8, no. 1. pp. 50–

59, 2003.

[35] K. Takahashi, H. Takagi, K. H. Shin, H. Uchida, P. B. Lim, and M. Inoue, “Figures of merit of magneto-optic spatial light modulators with magnetophotonic crystals,” *Phys. Stat. Sol. (C)*, vol. 4, no. 12, pp. 4536–4539, 2007.

[36] J. P. Huignard, “Spatial Light Modulators and Applications,” *J. Opt.*, vol. 18, no. 4, pp. 181–186, 1987.

[37] J. H. Park *et al.*, “Magnetooptic spatial light modulator array fabricated by IR annealing,” *Jpn. J. Appl. Phys.*, vol. 42, no. 4 B, pp. 2332–2334, 2003.

[38] J. Park, K. Cho, K. Nishimura, H. Uchida, and M. Inoue, “Flat-surface magneto-optic spatial light modulator by using thermal infrared ray annealing,” *Proc. SPIE*, vol. 5174, pp. 218–226, 2003.

[39] M. Banno, K. Onda, and H. Yui, “Improvement of Spatial Resolution for Nonlinear Raman Microscopy by Spatial Light Modulation,” *Anal. Sci.*, vol. 33, no. 1, pp. 69–74, 2017.

[40] J. C. Chau, C. Morales, and T. D. C. Little, “Using Spatial Light Modulators in MIMO Visible Light Communication Receivers to Dynamically Control the Optical Channel,” in *International Conference on Embedded Wireless Systems and Networks (EWSN)*, 2016, pp. 347–352.

[41] J. H. Park, J. H. Kim, J. K. Cho, K. Nishimura, H. Uchida, and M. Inoue, “An optical micro-magnetic display,” *J. Magn. Magn. Mater.*, vol. 272–276, no. III, pp. 2260–2262, 2004.

[42] Y. Igasaki *et al.*, “Hlgh Efficiency Electrlcally-Addressable Phase-Only Spatial Light,” *Opt. Rev.*, vol. 6, no. 4, pp. 339–344, 1999.

[43] Z. Zhang, Z. You, and D. Chu, “Fundamentals of phase-only liquid crystal on silicon (LCOS) devices,” *Light Sci. Appl.*, vol. 3, p. e213, 2014.

[44] M. Choi and J. Choi, “Universal phase-only spatial light modulators,” *Opt. Express*, vol. 25, no. 19, pp. 22253–22267, 2017.

[45] S.-Q. Li, X. Xu, R. M. Veetil, V. Valuckas, R. Paniagua-Domínguez, and A. I.

Kuznetsov, “Phase-only transmissive spatial light modulator based on tunable dielectric metasurface,” *Science*, vol. 364, pp. 1087–1090, 2019.

[46] L. J. Hornbeck, “128×128 deformable mirror devices,” *IEEE Trans. Electron Devices*, vol. ED-30, no. 5, pp. 539–545, 1983.

[47] J. Liang, R. N. Kohn, Jr., M. F. Becker, and D. J. Heinzen, “High-precision laser beam shaping using a binary-amplitude spatial light modulator,” *Appl. Opt.*, vol. 49, no. 8, pp. 1323–1330, 2010.

[48] K. A. Bauchert, S. A. Serati, G. D. Sharp, and D. J. McKnight, “Complex phase/amplitude spatial light modulator advances and use in a multispectral optical correlator,” *Proc. SPIE*, vol. 3073, pp. 170–177, 1997.

[49] E. Ulusoy, L. Onural, and H. M. Ozaktas, “Full-complex amplitude modulation with binary spatial light modulators,” *J. Opt. Soc. Am. A*, vol. 28, no. 11, pp. 2310–2321, 2011.

[50] “LC 2012 SPATIAL LIGHT MODULATOR (TRANSMISSIVE),” *HOLOEYE Photonics AG*. [Online]. Available: https://holoeye.com/spatial-light-modulators/lc-2012-spatial-light-modulator/. [Accessed: 09-May-2019].

[51] “GAEA-2 10 MEGAPIXEL PHASE ONLY LCOS-SLM (REFLECTIVE),” *HOLOEYE Photonics AG*. [Online]. Available: https://holoeye.com/gaea-4k-phase-only-spatial-light-modulator/. [Accessed: 09-May-2019].

[52] “SLM Research Kit 4K (SRK4K) – JD7714,” *Jasper Display Corp.* [Online]. Available: https://www.jasperdisplay.com/products/srk/jd7714/. [Accessed: 09-May-2019].

[53] “LCOS-SLM (Liquid Crystal on Silicon -Spatial Light Modulator),” *HAMAMATSU*. [Online]. Available: https://www.hamamatsu.com/eu/en/product/type/X13138-01/index.html. [Accessed: 09-May-2019].

[54] “Spatial Light Modulator – 512 x 512,” *Meadowlark Optics*. [Online]. Available: https://www.meadowlark.com/store/data_sheet/SLM-Small_512x512.pdf. [Accessed: 09-May-2019].

[55] "ForthDD spatial light modulators," *Forth Dimension Displays*. [Online]. Available: https://www.forthdd.com/products/spatial-light-modulators/. [Accessed: 09-May-2019].

[56] "DLP4710 0.47 1080p DMD," *TEXAS INSTRUMENTS*, 2018. [Online]. Available: http://www.ti.com/product/DLP4710. [Accessed: 09-May-2019].

[57] G. Li *et al.*, "Space bandwidth product enhancement of holographic display using high-order diffraction guided by holographic optical element," *Opt. Express*, vol. 23, no. 26, pp. 33170–33183, 2015.

[58] K. Iwasaki, H. Kawai, Y. Suzuki, H. Umezawa, and M. Inoue, "Fabrication and properties of spatial light modulator with magneto-optical Faraday effect," *Proc. SPIE*, vol. 6311, p. 631116, 2006.

[59] K. Aoshima *et al.*, "Submicron Magneto-Optical Spatial Light Modulation Device for Holographic Displays Driven by Spin-Polarized Electrons," *J. Disp. Technol.*, vol. 6, no. 9, pp. 374–380, 2010.

[60] T. Mishina, M. Okui, and F. Okano, "Viewing-zone enlargement method for sampled hologram that uses high-order diffraction," *Appl. Opt.*, vol. 41, no. 8, pp. 1489–1499, 2002.

[61] H. Butt *et al.*, "Carbon Nanotube Based High Resolution Holograms," *Adv. Mater.*, vol. 24, no. 44, pp. OP331–OP336, 2012.

[62] R. Stahl *et al.*, "Modular sub-wavelength diffractive light modulator for high-definition holographic displays," *J. Phys.: Conf. Ser.*, vol. 415, p. 012057, 2013.

[63] P. Hosseini, C. D. Wright, and H. Bhaskaran, "An optoelectronic framework enabled by low-dimensional phase-change films," *Nature*, vol. 511, no. 7508, pp. 206–211, 2014.

[64] Y. Montelongo, J. O. Tenorio-Pearl, C. Williams, S. Zhang, and W. I. Milne, "Plasmonic nanoparticle scattering for color holograms," *Proc. Natl. Acad. Sci.*, vol. 111, no. 35, pp. 12679–12683, 2014.

[65] X. Li *et al.*, "Athermally photoreduced graphene oxides for three-dimensional

holographic images," *Nat. Commun.*, vol. 6, p. 6984, 2015.

[66] S.-Y. Lee *et al.*, "Holographic image generation with a thin-film resonance caused by chalcogenide phase-change material," *Sci. Rep.*, vol. 7, p. 41152, 2017.

[67] K. A. Bauchert and S. A. Serati, "High-speed multilevel 512x512 spatial light modulator," *Proc. SPIE*, vol. 4043, no. 31 March 2000, pp. 59–65, 2000.

[68] F. Peng, H. Chen, S. Tripathi, R. J. Twieg, and S.-T. Wu, "Fast-response IR spatial light modulators with a polymer network liquid crystal," *Proc. SPIE*, vol. 9384, no. 11 March 2015, p. 93840N, 2015.

[69] S. Rout and S. R. Sonkusale, "A low-voltage high-speed terahertz spatial light modulator using active metamaterial," *APL Photonics*, vol. 1, p. 086102, 2016.

[70] Y. Horie, A. Arbabi, E. Arbabi, S. M. Kamali, and A. Faraon, "High-Speed, Phase-Dominant Spatial Light Modulation with Silicon-Based Active Resonant Antennas," *ACS Photonics*, vol. 5, pp. 1711–1717, 2018.

[71] S. Kharratian, H. Urey, and M. C. Onbaşlı, "RGB Magnetophotonic Crystals for High-contrast Magnetooptical Spatial Light Modulators," *Sci. Rep.*, vol. 9, p. 644, 2019.

[72] J. Cho *et al.*, "Design, fabrication, switching, and optical characteristics of new magneto-optic spatial light modulator," *J. Appl. Phys.*, vol. 76, no. 3, pp. 1910–1919, 1994.

[73] H. Takagi, J. Kim, K. H. Chung, S. Mito, H. Umezawa, and M. Inoue, "Magneto-Optic Spatial Light Modulators with Magnetophotonic Crystals Driven by PZT Films," *J. Magn. Soc. Japan*, vol. 33, no. 6–2, pp. 525–527, 2009.

[74] S. I. Khartsev and A. M. Grishin, "High performance [Bi3Fe5O12/Sm3Ga5O12]m magneto-optical photonic crystals," *J. Appl. Phys.*, vol. 101, p. 053906, 2007.

[75] J. O. Johansson, J.-W. Kim, E. Allwright, D. M. Rogers, N. Robertson, and J.-Y. Bigot, "Directly probing spin dynamics in a molecular magnet with femtosecond time-resolution," *Chem. Sci.*, vol. 7, no. 12, pp. 7061–7067, 2016.

[76] F. Siegrist *et al.*, "Petahertz Spintronics," *Prepr. https//arxiv.org/abs/1812.07420*, 2018.

[77] S. Fusil, V. Garcia, A. Barthélémy, and M. Bibes, "Magnetoelectric Devices for Spintronics," *Annu. Rev. Mater. Res.*, vol. 44, no. 1, pp. 91–116, 2014.

[78] C. O. Avci *et al.*, "Current-induced switching in a magnetic insulator," *Nat. Mater.*, vol. 16, no. 3, pp. 309–314, 2017.

[79] R. Ramesh and N. A. Spaldin, "Multiferroics: Progress and prospects in thin films," *Nat. Mater.*, vol. 6, no. 1, pp. 21–29, 2007.

[80] T. Imura, H. Koga, P. B. Lim, H. Umezawa, H. Horimai, and M. Inoue, "Collinear holography with magneto-optic spatial light modulator," *Proc. SPIE*, vol. 6311, p. 631115, 2006.

[81] K. Aoshima *et al.*, "An ultra-high definition spatial light modulation device driven by spin-polarized electrons," in *2009 IEEE Industry Applications Society Annual Meeting*, 2009, no. 48, pp. 1–7.

[82] K. V. Chellappan, E. Erden, and H. Urey, "Laser-based displays : a review," *Appl. Opt.*, vol. 49, no. 25, pp. F79–F98, 2010.

[83] S. C. Ellwood, "Hybrid Magneto-Photonic Crystal (MPC) Nanotechnology Display Technology for 3D Auto-Stereo Projection and Flexible Fiber Composite Display Systems," *Proc. SPIE*, vol. 8042, p. 804209, 2011.

[84] S. T. S. Holmström, U. Baran, and H. Urey, "MEMS laser scanners: A review," *J. Microelectromechanical Syst.*, vol. 23, no. 2, pp. 259–275, 2014.

[85] X. Y. Sun *et al.*, "Single-Step Deposition of Cerium-Substituted Yttrium Iron Garnet for Monolithic On-Chip Optical Isolation," *ACS Photonics*, vol. 2, pp. 856–863, 2015.

[86] S.-M. Kim and S.-M. Kim, "Performance improvement of visible light communications using optical beamforming," in *Fifth International Conference on Ubiquitous and Future Networks (ICUFN)*, 2013, pp. 362–365.

[87] A. B. Khanikaev and M. J. Steel, "Low-symmetry magnetic photonic crystals for nonreciprocal and unidirectional devices," *Opt. Express*, vol. 17, no. 7, pp. 5265–5272, 2009.

[88] R. Higashida, N. Funabashi, K. Aoshima, M. Miura, and K. Machida, "Diffraction of

light using high-density magneto-optical light modulator array," *Opt. Eng.*, vol. 59, no. 6, p. 064104, 2020.

[89] J. P. Krumme, H. Heitmann, D. Mateika, and K. Witter, "MOPS, a magneto-optic-photoconductor sandwich for optical information storage," *J. Appl. Phys.*, vol. 48, no. 1, pp. 366–368, 1977.

[90] J.-H. Park *et al.*, "Magneto-optic spatial light modulators driven by an electric field," *J. Appl. Phys.*, vol. 93, no. 10 3, pp. 8525–8527, 2003.

[91] J.-H. Park, J.-K. Cho, K. Nishimura, H. Uchida, and M. Inoue, "Magneto-optic spatial light modulator with one-step pattern formation," *Proc. SPIE*, vol. 5363, pp. 131–136, 2004.

[92] W. Feng, G.-Y. Guo, J. Zhou, Y. Yao, and Q. Niu, "Large magneto-optical Kerr effect in noncollinear antiferromagnets Mn3X (X=Rh, Ir, Pt)," *Phys. Rev. B*, vol. 92, p. 144426, 2015.

[93] N. Sivadas, S. Okamoto, and D. Xiao, "Gate-Controllable Magneto-optic Kerr Effect in Layered Collinear Antiferromagnets," *Phys. Rev. Lett.*, vol. 117, p. 267203, 2016.

[94] T. Higo *et al.*, "Large magneto-optical Kerr effect and imaging of magnetic octupole domains in an antiferromagnetic metal," *Nat. Photonics*, vol. 12, pp. 73–78, 2018.

[95] T. V Mikhailova, V. N. Berzhansky, A. V Karavainikov, A. N. Shaposhnikov, A. R. Prokopov, and S. D. Lyashko, "One-dimensional photonic crystals with highly Bi-substituted iron garnet defect in reflection polar geometry," *J. Phys.: Conf. Ser.*, vol. 741, p. 012121, 2016.

[96] P. M. Hui and D. Stroud, "Theory of Faraday Rotation by Dilute Suspensions of Small Particles," *Appl. Phys. Lett.*, vol. 50, no. 15, pp. 950–952, 1987.

[97] E. Jesenska *et al.*, "Optical and Magneto-Optical Properties of Gd22Fe78 Thin Films in the Photon Energy Range From 1.5 to 5.5 eV," *Materials*, vol. 9, p. 23, 2016.

[98] S. Wittekoek, T. J. A. Popma, J. M. Robertson, and P. F. Bongers, "Magneto-optic spectra and the dielectric tensor elements of bismuth-substituted iron garnets at photon energies between 2.2-5.2 eV," *Phys. Rev. B*, vol. 12, no. 7, pp. 2777–2788, 1975.

[99] A. R. Davoyan and N. Engheta, "Nanoscale plasmonic circulator," *New J. Phys.*, vol. 15, p. 083054, 2013.

[100] F. Hansteen, L. E. Helseth, T. H. Johansen, O. Hunderi, A. Kirilyuk, and T. Rasing, "Optical and magnetooptical properties of bismuth and gallium substituted iron garnet films," *Thin Solid Films*, vol. 455–456, pp. 429–432, 2004.

[101] P. S. Pershan, "Magneto-optical effects," *J. Appl. Phys.*, vol. 38, pp. 1482–1490, 1967.

[102] D. K. Misemer, "The effect of spin-orbit interaction and exchange splitting on magneto-optic coefficients," *J. Magn. Magn. Mater.*, vol. 72, pp. 267–274, 1988.

[103] T. Aichele, A. Lorenz, R. Hergt, and P. Görnert, "Garnet layers prepared by liquid phase epitaxy for microwave and magneto-optical applications – a review," *Cryst. Res. Technol.*, vol. 38, no. 7–8, pp. 575–587, 2003.

[104] T. Mizumoto, R. Baets, and J. E. Bowers, "Optical nonreciprocal devices for silicon photonics using wafer-bonded magneto-optical garnet materials," *MRS Bull.*, vol. 43, no. 6, pp. 419–424, 2018.

[105] W. Tolksdorf and F. Wels, "The Effect of Local Cooling and Accelerated Crucible Rotation on the Quality of Garnet Crystals," *J. Cryst. Growth*, vol. 13, no. 14, pp. 566–570, 1972.

[106] W. Wettling, B. Andlauer, P. Koidl, J. Schneider, and W. Tolksdorf, "Optical absorption and Faraday rotation in yttrium iron garnet," *Phys. Stat. Sol. (B)*, vol. 59, pp. 63–70, 1973.

[107] B. Andlauer, J. Schneider, and W. Wettling, "Optical and Magneto-Optical Properties of YIG and FeBO3," *Appl. Phys.*, vol. 10, pp. 189–201, 1976.

[108] D. E. Lacklison, G. B. Scott, H. I. Ralph, and J. L. Page, "Garnets with High Magnetooptic Figures of Merit in the Visible Region," *IEEE Trans. Magn.*, vol. MAG-9, no. 3, pp. 457–460, 1973.

[109] W. Jantzt, J. R. Sandercock, and W. Wettlingt, "Determination of magnetic and elastic properties of FeBO, by light scattering," *J. Phys. C: Solid State Phys.*, vol. 9, pp. 2229–2240, 1976.

[110] G. S. Krinchik, K. M. Mukimov, S. M. Sharipov, A. P. Khrebtov, and E. M. Speranskaya, "The permittivity tensor and increase in the transmittance of the spinel ferrites upon their conversion into single- sublattice structures," *Sov. Physics—JETP*, vol. 49, no. 6, pp. 1074–1079, 1979.

[111] V. Doormann, J.-P. Krumme, and H. Lenz, "Optical and magneto-optical tensor spectra of bismuth-substituted yttrium-iron-garnet films," *J. Appl. Phys.*, vol. 68, no. 7, pp. 3544–3553, 1990.

[112] H. Fu, Z. Yan, S. K. Lee, and M. Mansuripur, "Dielectric tensor characterization and evaluation of several magneto-optical recording media," *J. Appl. Phys.*, vol. 78, no. 6, pp. 4076–4090, 1995.

[113] L. Halagačka *et al.*, "Mueller matrix optical and magneto-optical characterization of Bi-substituted gadolinium iron garnet for application in magnetoplasmonic structures," *Opt. Mater. Express*, vol. 4, no. 9, pp. 1903–1919, 2014.

[114] M. C. Onbasli *et al.*, "Optical and magneto-optical behavior of Cerium Yttrium Iron Garnet thin films at wavelengths of 200–1770 nm," *Sci. Rep.*, vol. 6, p. 23640, 2016.

[115] E. Jesenska *et al.*, "Optical and magneto-optical properties of Bi substituted yttrium iron garnets prepared by metal organic decomposition," *Opt. Mater. Express*, vol. 6, no. 6, pp. 1986–1997, 2016.

[116] A. J. Kurtzig, "Faraday rotation in birefringent crystals," *J. Appl. Phys.*, vol. 42, pp. 3494–3498, 1971.

[117] B. Sepúlveda, J. B. González-Díaz, A. García-Martín, L. M. Lechuga, and G. Armelles, "Plasmon-induced magneto-optical activity in nanosized gold disks," *Phys. Rev. Lett.*, vol. 104, p. 147401, 2010.

[118] Y. Shiota, T. Maruyama, T. Nozaki, T. Shinjo, M. Shiraishi, and Y. Suzuki, "Voltage-assisted magnetization switching in ultrathin Fe80Co20alloy layers," *Appl. Phys. Express*, vol. 2, p. 063001, 2009.

[119] D. A. Allwood, G. Xiong, M. D. Cooke, and R. P. Cowburn, "Magneto-optical Kerr effect analysis of magnetic nanostructures," *J. Phys. D: Appl. Phys.*, vol. 36, pp. 2175–

2182, 2003.

[120] J. P. Jamet *et al.*, “Giant enhancement of the domain wall velocity in irradiated ultrathin magnetic nanowires,” *IEEE Trans. Magn.*, vol. 37, no. 4 I, pp. 2120–2122, 2001.

[121] M. R. Freeman and W. K. Hiebert, *Stroboscopic Microscopy of Magnetic Dynamics*. Berlin: Springer, 2002.

[122] H. R. Hulme, “The Faraday Effect in Ferromagnetics,” *Proc. Royal Soc. A*, vol. 135, no. 826, pp. 237–257, 1932.

[123] L. Wang *et al.*, “Plasmonics and Enhanced Magneto-Optics in Core−Shell Co−Ag Nanoparticles,” *Nano Lett.*, vol. 11, pp. 1237–1240, 2011.

[124] X. Zhou, F. Li, Y. Xing, and W. Feng, “Multifield-tunable magneto-optical effects in electron- and hole-doped nitrogen-graphene crystals,” *J. Mater. Chem. C*, vol. 7, no. 11, pp. 3360–3368, 2019.

[125] I. V. Fialkovsky and D. V. Vassilevich, “Parity-odd effects and polarization rotation in graphene,” *J. Phys. A: Math. Theor.*, vol. 42, p. 442001, 2009.

[126] T. Morimoto, Y. Hatsugai, and H. Aoki, “Optical Hall conductivity in ordinary and graphene quantum Hall systems,” *Phys. Rev. Lett.*, vol. 103, p. 116803, 2009.

[127] I. Crassee *et al.*, “Giant Faraday rotation in single- and multilayer graphene,” *Nat. Phys.*, vol. 7, pp. 48–51, 2011.

[128] N. Ubrig *et al.*, “Fabry-Perot enhanced Faraday rotation in graphene,” *Opt. Express*, vol. 21, no. 21, pp. 24736–24741, 2013.

[129] R. Shimano *et al.*, “Quantum faraday and kerr rotations in graphene,” *Nat. Commun.*, vol. 4, p. 1841, 2013.

[130] L. Falkovsky, “Quantum Magneto-Optics in Graphene,” *Photonics*, vol. 2, pp. 13–20, 2015.

[131] M. Oliva-Leyva and C. Wang, “Magneto-optical conductivity of anisotropic two-dimensional Dirac–Weyl materials,” *Ann. Phys. (N. Y).*, vol. 384, pp. 61–70, 2017.

[132] V. Hung Nguyen, A. Lherbier, and J.-C. Charlier, “Optical hall effect in strained

graphene," *2D Mater.*, vol. 4, p. 025041, 2017.

[133] J. M. Poumirol *et al.*, "Electrically controlled terahertz magneto-optical phenomena in continuous and patterned graphene," *Nat. Commun.*, vol. 8, p. 14626, 2017.

[134] M. Shah and M. S. Anwar, "Magneto-optical effects in the Landau level manifold of 2D lattices with spin-orbit interaction," *Prepr. https//arxiv.org/abs/1902.05359v1*, 2019.

[135] M. Tahir, P. Vasilopoulos, and F. M. Peeters, "Magneto-optical transport properties of monolayer phosphorene," *Phys. Rev. B*, vol. 92, p. 045420, 2015.

[136] R. L. Chu *et al.*, "Valley-splitting and valley-dependent inter-Landau-level optical transitions in monolayer MoS2 quantum Hall systems," *Phys. Rev. B*, vol. 90, p. 045427, 2014.

[137] M. Tahir and P. Vasilopoulos, "Magneto-optical transport properties of monolayer WSe2," *Phys. Rev. B*, vol. 94, p. 045415, 2016.

[138] B. Huang *et al.*, "Layer-dependent ferromagnetism in a van der Waals crystal down to the monolayer limit.," *Nature*, vol. 546, no. 7657, pp. 270–273, 2017.

[139] B. Huang *et al.*, "Electrical control of 2D magnetism in bilayer CrI3," *Nat. Nanotechnol.*, vol. 13, no. 7, pp. 544–548, 2018.

[140] G. Guo, G. Bi, C. Cai, and H. Wu, "Effects of external magnetic field and out-of-plane strain on magneto-optical Kerr spectra in CrI3 monolayer," *J. Phys.: Condens. Matter*, vol. 30, p. 285303, 2018.

[141] C. Gong *et al.*, "Discovery of intrinsic ferromagnetism in two-dimensional van der Waals crystals," *Nature*, vol. 546, no. 7657, pp. 265–269, 2017.

[142] Z. Wang *et al.*, "Electric-field control of magnetism in a few-layered van der Waals ferromagnetic semiconductor," *Nat. Nanotechnol.*, vol. 13, pp. 554–559, 2018.

[143] P. E. C. Ashby and J. P. Carbotte, "Magneto-optical conductivity of Weyl semimetals," *Phys. Rev. B*, vol. 87, p. 245131, 2013.

[144] M. Kargarian, M. Randeria, and N. Trivedi, "Theory of Kerr and Faraday rotations and linear dichroism in Topological Weyl Semimetals," *Sci. Rep.*, vol. 5, p. 12683,

2015.

[145] P. Hosur and X.-L. Qi, “Tunable circular dichroism due to the chiral anomaly in Weyl semimetals,” *Phys. Rev. B*, vol. 91, p. 081106(R), 2015.

[146] B. Xu *et al.*, “Optical Signatures of Weyl Points in TaAs,” *Phys. Rev. B*, vol. 93, p. 121110(R), 2016.

[147] S. C. Wu, Y. Sun, C. Felser, and B. Yan, “Hidden type-II Weyl points in the Weyl semimetal NbP,” *Phys. Rev. B*, vol. 96, p. 165113, 2017.

[148] C. Zhang *et al.*, “Room-temperature chiral charge pumping in Dirac semimetals,” *Nat. Commun.*, vol. 8, p. 13741, 2017.

[149] J. H. Park, J. K. Cho, K. Nishimura, H. Uchida, and M. Inoue, “Growth of epitaxial garnet film by LPE for application to integrated magneto-optic light switch arrays,” *Phys. Stat. Sol. (A)*, vol. 201, no. 8, pp. 1976–1979, 2004.

[150] M. Veis *et al.*, “Complete permittivity tensor in sputtered CuFe2O4thin films at photon energies between 2 and 5 eV,” *Materials*, vol. 6, pp. 4096–4108, 2013.

[151] S. Kahl and A. M. Grishin, “Evolution of properties of epitaxial bismuth iron garnet films with increasing thickness,” *J. Magn. Magn. Mater.*, vol. 278, no. 1–2, pp. 244–255, 2004.

[152] T. Boudiar *et al.*, “Magneto-optical properties of yttrium iron garnet (YIG) thin films elaborated by radio frequency sputtering,” *Proc. SPIE*, vol. 5250, pp. 263–270, 2004.

[153] B. A. Gizhevskii *et al.*, “Optical and Magneto Optical Properties of Nanostructured Yttrium Iron Garnet,” *Phys. Solid State*, vol. 51, no. 9, pp. 1836–1842, 2009.

[154] S. Kahl, “Bismuth iron garnet films for magneto-optical photonic crystals,” Royal Institute of Technology, 2004.

[155] T. Ishibashi, T. Kosaka, M. Naganuma, and T. Nomura, “Magneto-optical properties of Bi-substituted yttrium iron garnet films by metal-organic decomposition method,” *J. Phys.: Conf. Ser.*, vol. 200, p. 112002, 2010.

[156] M. Nur-E-Alam, M. Vasiliev, K. Alameh, and V. Kotov, “Physical properties and behaviour of highly Bi-substituted magneto-optic garnets for applications in integrated

optics and photonics," *Adv. Opt. Technol.*, vol. 2011, p. 971267, 2011.

[157] P. Dulal *et al.*, "Optimized Magneto-optical Isolator Designs Inspired by Seedlayer-Free Terbium Iron Garnets with Opposite Chirality," *ACS Photonics*, vol. 3, no. 10, pp. 1818–1825, 2016.

[158] S. Mino, A. Tate, T. Uno, T. Shintaku, and A. Shibukawa, "Structure and lattice deformation of Ce-substituted yttrium iron garnet film prepared by RF sputtering," *Jpn. J. Appl. Phys.*, vol. 32, no. 7, pp. 3154–3159, 1993.

[159] T. Goto, M. C. Onbaşlı, and C. A. Ross, "Magneto-optical properties of cerium substituted yttrium iron garnet films with reduced thermal budget for monolithic photonic integrated circuits," *Opt. Express*, vol. 20, no. 27, pp. 28508–28517, 2012.

[160] A. Kehlberger *et al.*, "Enhanced magneto-optic Kerr effect and magnetic properties of CeY2Fe5O12 epitaxial thin films," *Phys. Rev. Appl.*, vol. 4, p. 014008, 2015.

[161] P. Dulal, T. E. Gage, A. D. Block, E. Cofell, D. C. Hutchings, and B. J. H. Stadler, "Sputter-deposited seedlayer-free cerium-doped terbium iron garnets for SOI waveguide isolators," in *IEEE Photonics Conference (IPC)*, 2016, pp. 773–774.

[162] F. Zhang, Y. Xu, J. Yang, and M. Guillot, "A theoretical study of the magnetic and magneto-optical properties of Nd-substituted yttrium iron garnets," *J. Phys.: Condens. Matter*, vol. 12, no. 32, pp. 7287–7294, 2000.

[163] P. Hansen, K. Witter, and W. Tolksdorf, "Magnetic and magneto-optic properties of bismuth- and aluminum-substituted iron garnet films," *J. Appl. Phys.*, vol. 55, no. 4, pp. 1052–1061, 1984.

[164] P. Hansen, C. P. Klages, J. Schuldt, and K. Witter, "Magnetic and magneto-optical properties of bismuth-substituted lutetium iron garnet films," *Phys. Rev. B*, vol. 31, no. 9, pp. 5858–5864, 1985.

[165] K. Srinivasan and B. J. H. Stadler, "Magneto-optical materials and designs for integrated TE- and TM-mode planar waveguide isolators: a review [Invited]," *Opt. Mater. Express*, vol. 8, no. 11, pp. 3307–3318, 2018.

[166] S.-Y. Sung, X. Qi, and B. J. H. Stadler, "Integrating yttrium iron garnet onto nongarnet

substrates with faster deposition rates and high reliability," *Appl. Phys. Lett.*, vol. 87, p. 121111, 2005.

[167] A. Furuya *et al.*, "Magneto-optical properties of a sputtered Bi-substituted Dy – Fe garnet-ferrite/hematite bilayer," *J. Appl. Phys.*, vol. 85, no. 8, pp. 5106–5108, 1999.

[168] A. D. Block, P. Dulal, B. J. H. Stadler, and N. C. A. Seaton, "Growth Parameters of Fully Crystallized YIG , Bi:YIG , and Ce:YIG Films With High Faraday Rotations," *IEEE Photonics J.*, vol. 6, no. 1, p. 0600308, 2014.

[169] X. Sun, M. C. Onbasli, and C. A. Ross, "Method for forming magneto-optical films for integrated photonic devices," 9829728, 2017.

[170] M. Nur-E-Alam, M. Vasiliev, V. Kotov, and K. Alameh, "Recent developments in magneto-optic garnet-type thin-film materials synthesis," *Procedia Eng.*, vol. 76, pp. 61–73, 2014.

[171] G. J. Chen, H. M. Lee, Y. S. Chang, Y. J. Lin, and Y. L. Chai, "Preparation and properties of yttrium iron garnet microcrystal in P2O5–MgO glass," *J. Alloys Compd.*, vol. 388, pp. 297–302, 2005.

[172] M. Sadatgol, M. Rahman, E. Forati, M. Levy, and D. O. Guney, "Enhanced Faraday rotation in hybrid magneto-optical metamaterial structure of bismuth-substituted-iron-garnet with," *J. Appl. Phys.*, vol. 119, p. 103105, 2016.

[173] B. Gu, S. Takahashi, and S. Maekawa, "Enhanced magneto-optical Kerr effect at Fe/insulator interfaces," *Phys. Rev. B*, vol. 96, p. 214423, 2017.

[174] M. Inoue, K. Arai, T. Fujii, and M. Abe, "Magneto-optical properties of one-dimensional photonic crystals composed of magnetic and dielectric layers," *J. Appl. Phys.*, vol. 83, no. 11, pp. 6768–6770, 1998.

[175] H. Kato, T. Matsushita, A. Takayama, M. Egawa, K. Nishimura, and M. Inoue, "Theoretical analysis of optical and magneto-optical properties of one-dimensional magnetophotonic crystals," *J. Appl. Phys.*, vol. 93, no. 7, pp. 3906–3911, 2003.

[176] H. Da and G. Liang, "Enhanced Faraday rotation in magnetophotonic crystal infiltrated with graphene," *Appl. Phys. Lett.*, vol. 98, p. 261915, 2011.

[177] M. J. Steel, M. Levy, and R. M. Osgood, "High Transmission Enhanced Faraday Rotation in One-Dimensional Photonic Crystals with Defects," *IEEE Photonics Technol. Lett.*, vol. 12, no. 9, pp. 1171–1173, 2000.

[178] M. Inoue *et al.*, "Magnetophotonic crystals," *J. Phys. D: Appl. Phys.*, vol. 39, pp. R151–R161, 2006.

[179] B. Aktaş, L. Tagirov, and F. Mikailov, *Magnetic Nanostructures*. Berlin: Springer-Verlag, 2007.

[180] M. Inoue, H. Uchida, P. B. Lim, A. V. Baryshev, and A. V. Khanikaev, "Magnetophotonic crystals : now and future," *Adv. Sci. Technol.*, vol. 45, pp. 2588–2597, 2006.

[181] D. Floess *et al.*, "Plasmonic Analog of Electromagnetically Induced Absorption Leads to Giant Thin Film Faraday Rotation of 14°," *Phys. Rev. X*, vol. 7, p. 021048, 2017.

[182] A. R. Davoyan and N. Engheta, "Nonreciprocal rotating power flow within plasmonic nanostructures," *Phys. Rev. Lett.*, vol. 111, p. 047401, 2013.

[183] J. Y. Chin *et al.*, "Nonreciprocal plasmonics enables giant enhancement of thin-film Faraday rotation," *Nat. Commun.*, vol. 4, p. 1599, 2013.

[184] D. Floess *et al.*, "Tunable and switchable polarization rotation with non-reciprocal plasmonic thin films at designated wavelengths," *Light Sci. Appl.*, vol. 4, p. e284, 2015.

[185] N. Maccaferri *et al.*, "Nanoscale magnetophotonics," *Prepr. https//arxiv.org/abs/1904.11846v1*, 2019.

[186] S. A. Maier, *Plasmonics: Fundamentals and Applications*. New York: Springer, 2007.

[187] I. D. Mayergoyz, *Plasmonic Resonances in Nanoparticles*. Singapore: World Scientific, 2012.

[188] B. Sepúlveda, A. Calle, L. M. Lechuga, and G. Armelles, "Highly sensitive detection of biomolecules with the magneto-optic surface-plasmon-resonance sensor," *Opt. Lett.*, vol. 31, no. 8, pp. 1085–1087, 2006.

[189] G. Armelles, A. Cebollada, A. García-Martín, and M. U. González,

"Magnetoplasmonics: Combining Magnetic and Plasmonic Functionalities," *Adv. Opt. Mater.*, vol. 1, no. 1, pp. 10–35, 2013.

[190] J. Qin *et al.*, "Ultrahigh Figure-of-Merit in Metal-Insulator-Metal Magnetoplasmonic Sensors Using Low Loss Magneto-optical Oxide Thin Films," *ACS Photonics*, vol. 4, no. 6, pp. 1403–1412, 2017.

[191] T. Wu, X. Zhang, R. Wang, and X. Zhang, "Strongly enhanced Raman optical activity in molecules by magnetic response of nanoparticles," *J. Phys. Chem. C*, vol. 120, pp. 14795–14804, 2016.

[192] S. Abdali and E. W. Blanch, "Surface-Enhanced Raman Optical Activity (SEROA)," *Chem. Soc. Rev.*, vol. 37, no. 5, pp. 980–992, 2008.

[193] A. Campion and P. Kambhampati, "Surface-enhanced Raman scattering," *Chem. Soc. Rev.*, vol. 27, pp. 241–250, 1998.

[194] S. Schlücker, "Surface-Enhanced Raman Spectroscopy : Concepts and Chemical Applications," *Angew. Chemie Int. Ed.*, vol. 53, pp. 4756–4795, 2014.

[195] D. Cialla-May, X.-S. Zheng, K. Weber, and J. Popp, "Recent progress in surface-enhanced Raman spectroscopy for biological and biomedical applications: from cells to clinics," *Chem. Soc. Rev.*, vol. 46, no. 13, pp. 3945–3961, 2017.

[196] J. Cailletaud *et al.*, "Critical review of surface-enhanced Raman spectroscopy applications in the pharmaceutical field," *J. Pharm. Biomed. Anal.*, vol. 147, pp. 458–472, 2018.

[197] V. Parchaňský, J. Kapitán, and P. Bouř, "Inspecting chiral molecules by Raman optical activity spectroscopy," *RSC Adv.*, vol. 4, pp. 57125–57136, 2014.

[198] L. D. Barron, "The development of biomolecular Raman optical activity spectroscopy," *Biomed. Spectrosc. Imaging*, vol. 4, pp. 223–253, 2015.

[199] M. A. Fikiet *et al.*, "Surface enhanced Raman spectroscopy : A review of recent applications in forensic science," *Spectrochim. Acta Part A Mol. Biomol. Spectrosc.*, vol. 197, pp. 255–260, 2018.

[200] H. Wei, S. M. Hossein Abtahi, and P. J. Vikesland, "Plasmonic colorimetric and SERS

sensors for environmental analysis," *Environ. Sci. Nano,* vol. 2, no. 2, pp. 120–135, 2015.

[201] H. Kneipp, J. Kneipp, and K. Kneipp, "Surface-enhanced Raman optical activity on adenine in silver colloidal solution," *Anal. Chem.*, vol. 78, no. 4, pp. 1363–1366, 2006.

[202] A. R. Bizzarri and S. Cannistraro, "Surface-enhanced resonance Raman spectroscopy signals from single myoglobin molecules," *Appl. Spectrosc.*, vol. 56, no. 12, pp. 1531–1537, 2002.

[203] S. Abdali, "Observation of SERS effect in Raman optical activity, a new tool for chiral vibrational spectroscopy," *J. Raman Spectrosc.*, vol. 37, pp. 1341–1345, 2006.

[204] C. Johannessen, P. C. White, and S. Abdali, "Resonance Raman optical activity and surface enhanced resonance Raman optical activity analysis of cytochrome c," *J. Phys. Chem. A*, vol. 111, no. 32, pp. 7771–7776, 2007.

[205] C. Johannessen and S. Abdali, "Surface enhanced Raman optical activity as an ultra sensitive tool for ligand binding analysis," *Spectroscopy*, vol. 21, pp. 143–149, 2007.

[206] S. Abdali, C. Johannessen, J. Nygaard, and T. Nørbygaard, "Resonance surface enhanced Raman optical activity of myoglobin as a result of optimized resonance surface enhanced Raman scattering conditions," *J. Phys.: Condens. Matter*, vol. 19, p. 285205, 2007.

[207] D. Drescher, T. Büchner, D. McNaughton, and J. Kneipp, "SERS reveals the specific interaction of silver and gold nanoparticles with hemoglobin and red blood cell components," *Phys. Chem. Chem. Phys.*, vol. 15, no. 15, pp. 5364–5373, 2013.

[208] J. Jiang, C. Auchinvole, K. Fisher, and C. J. Campbell, "Quantitative measurement of redox potential in hypoxic cells using SERS nanosensors," *Nanoscale*, vol. 6, pp. 12104–12110, 2014.

[209] Y. Han *et al.*, "Potential use of SERS-assisted theranostic strategy based on Fe3O4/Au cluster/shell nanocomposites for bio-detection, MRI, and magnetic hyperthermia," *Mater. Sci. Eng. C*, vol. 64, pp. 199–207, 2016.

[210] Z. A. Nima *et al.*, "Circulating tumor cell identification by functionalized silver-gold

nanorods with multicolor, super-enhanced SERS and photothermal resonances," *Sci. Rep.*, vol. 4, p. 4752, 2014.

[211] J. K. Register *et al.*, "In vivo detection of SERS-encoded plasmonic nanostars in human skin grafts and live animal models," *Anal. Bioanal. Chem.*, vol. 407, pp. 8215–8224, 2015.

[212] W. Song, L. Ding, Y. Chen, and H. Ju, "Plasmonic coupling of dual gold nanoprobes for SERS imaging of sialic acids on living cells," *Chem. Commun.*, vol. 52, no. 70, pp. 10640–10643, 2016.

[213] X. S. Zheng *et al.*, "BSA-coated nanoparticles for improved SERS-based intracellular pH sensing," *Anal. Chem.*, vol. 86, no. 24, pp. 12250–12257, 2014.

[214] Y. Cao, D. W. Li, L. J. Zhao, X. Y. Liu, X. M. Cao, and Y. T. Long, "Highly Selective Detection of Carbon Monoxide in Living Cells by Palladacycle Carbonylation-Based Surface Enhanced Raman Spectroscopy Nanosensors," *Anal. Chem.*, vol. 87, no. 19, pp. 9696–9701, 2015.

[215] J. Cui, K. Hu, J. J. Sun, L. L. Qu, and D. W. Li, "SERS nanoprobes for the monitoring of endogenous nitric oxide in living cells," *Biosens. Bioelectron.*, vol. 85, pp. 324–330, 2016.

[216] L.-L. Qu, Y.-Y. Liu, S.-H. He, J.-Q. Chen, Y. Liang, and H.-T. Li, "Highly selective and sensitive surface enhanced Raman scattering nanosensors for detection of hydrogen peroxide in living cells," *Biosens. Bioelectron.*, vol. 77, pp. 292–298, 2016.

[217] X. Gu, H. Wang, Z. D. Schultz, and J. P. Camden, "Sensing Glucose in Urine and Serum and Hydrogen Peroxide in Living Cells by Use of a Novel Boronate Nanoprobe Based on Surface-Enhanced Raman Spectroscopy," *Anal. Chem.*, vol. 88, no. 14, pp. 7191–7197, 2016.

[218] M. K. Hossain, H. Y. Cho, K. J. Kim, and J. W. Choi, "In situ monitoring of doxorubicin release from biohybrid nanoparticles modified with antibody and cell-penetrating peptides in breast cancer cells using surface-enhanced Raman spectroscopy," *Biosens. Bioelectron.*, vol. 71, pp. 300–305, 2015.

[219] A. Pallaoro, M. R. Hoonejani, G. B. Braun, C. D. Meinhart, and M. Moskovits, "Rapid identification by surface-enhanced raman spectroscopy of cancer cells at low concentrations flowing in a microfluidic channel," *ACS Nano*, vol. 9, no. 4, pp. 4328–4336, 2015.

[220] P. Mosier-Boss, "Review of SERS Substrates for Chemical Sensing," *Nanomaterials*, vol. 7, p. 142, 2017.

[221] S. Uskoković-Marković, V. Kuntić, D. Bajuk-Bogdanović, and I. Holclajtner-Antunović, "Surface-Enhanced Raman Scattering (SERS) Biochemical Applications," in *Encyclopedia of Spectroscopy and Spectrometry*, Third., J. C. Lindon, G. E. Tranter, and D. W. Koppenaal, Eds. Amsterdam: Elsevier Ltd, 2017, pp. 383–388.

[222] W. A. El-Said and J. W. Choi, "In-situ detection of neurotransmitter release from PC12 cells using Surface Enhanced Raman Spectroscopy," *Biotechnol. Bioprocess Eng.*, vol. 19, no. 6, pp. 1069–1076, 2014.

[223] C. M. Girish *et al.*, "Rapid detection of oral cancer using Ag-TiO2 nanostructured surface-enhanced Raman spectroscopic substrates," *J. Mater. Chem. B*, vol. 2, no. 8, pp. 989–998, 2014.

[224] L. Wu *et al.*, "Highly sensitive, reproducible and uniform SERS substrates with a high density of three-dimensionally distributed hotspots: gyroid-structured Au periodic metallic materials," *NPG Asia Mater.*, vol. 10, p. e462, 2018.

[225] J. Deng, J. Dong, and P. Cohen, "Rapid Fabrication and Characterization of SERS Substrates," *Procedia Manuf.*, vol. 26, pp. 580–586, 2018.

[226] L. Mayer, "Curie-point writing on magnetic films," *J. Appl. Phys.*, vol. 29, no. 6, p. 1003, 1958.

[227] L. Mayer, "Magnetic writing with an electron beam," *J. Appl. Phys.*, vol. 29, no. 10, pp. 1454–1456, 1958.

[228] G. Y. Fan and J. H. Greiner, "Low-temperature beam-addressable memory," *J. Appl. Phys.*, vol. 39, no. 2, pp. 1216–1218, 1968.

[229] G. Fan, K. Pennington, and J. H. Greiner, “Magneto-optic hologram,” *J. Appl. Phys.*, vol. 40, no. 3, pp. 974–975, 1969.

[230] J. P. Krumme, P. Hansen, and K. Witter, “Thermomagnetic switching of ferrimagnetic garnet films at their compensation temperature,” *J. Appl. Phys.*, vol. 47, no. 8, pp. 3681–3689, 1976.

[231] C. D. Stanciu *et al.*, “All-optical magnetic recording with circularly polarized light,” *Phys. Rev. Lett.*, vol. 99, p. 047601, 2007.

[232] K. Vahaplar *et al.*, “Ultrafast Path for Optical Magnetization Reversal via a Strongly Nonequilibrium State,” *Phys. Rev. Lett.*, vol. 103, p. 117201, 2009.

[233] H. Takagi, K. Nakamura, T. Goto, P. B. Lim, and M. Inoue, “Magneto-optic spatial light modulator with submicron-size magnetic pixels for wide-viewing-angle holographic displays.,” *Opt. Lett.*, vol. 39, no. 11, pp. 3344–3347, 2014.

[234] K. Nakamura *et al.*, “Improvement of diffraction efficiency of three-dimensional magneto-optic spatial light modulator with magnetophotonic crystal,” *Appl. Phys. Lett.*, vol. 108, p. 022404, 2016.

[235] A. V. Kimel, A. Kirilyuk, F. Hansteen, R. V. Pisarev, and T. Rasing, “Nonthermal optical control of magnetism and ultrafast laser-induced spin dynamics in solids,” *J. Phys.: Condens. Matter*, vol. 19, p. 043201, 2007.

[236] A. Kirilyuk, A. V. Kimel, and T. Rasing, “Ultrafast optical manipulation of magnetic order,” *Rev. Mod. Phys.*, vol. 82, pp. 2731–2784, 2010.

[237] A. V. Kimel, A. Kirilyuk, P. A. Usachev, R. V. Pisarev, A. M. Balbashov, and T. Rasing, “Ultrafast non-thermal control of magnetization by instantaneous photomagnetic pulses,” *Nature*, vol. 435, pp. 655–657, 2005.

[238] M. A. Kozhaev *et al.*, “Giant peak of the Inverse Faraday effect in the band gap of magnetophotonic microcavity,” *Sci. Rep.*, vol. 8, p. 11435, 2018.

[239] F. Hansteen, A. Kimel, A. Kirilyuk, and T. Rasing, “Femtosecond photomagnetic switching of spins in ferrimagnetic garnet films,” *Phys. Rev. Lett.*, vol. 95, p. 047402, 2005.

[240] A. Stupakiewicz, K. Szerenos, D. Afanasiev, A. Kirilyuk, and A. V. Kimel, "Ultrafast nonthermal photo-magnetic recording in a transparent medium," *Nature*, vol. 542, pp. 71–74, 2017.

[241] F. T. S. Yu, X. Lu, and M. Cao, "Application of a magnetooptic spatial light modulator to white-light optical processing," *Appl. Opt.*, vol. 23, no. 22, pp. 4100–4104, 1984.

[242] K. Iwasaki, H. Mochizuki, H. Umezawa, and M. Inoue, "Practical magneto-optic spatial light modulator with single magnetic domain pixels," *IEEE Trans. Magn.*, vol. 44, no. 11, pp. 3296–3299, 2008.

[243] L. Liu, C.-F. Pai, Y. Li, H. W. Tseng, D. C. Ralph, and R. A. Buhrman, "Spin-Torque Switching with the Giant Spin Hall Effect of Tantalum," *Science*, vol. 336, pp. 555–558, 2012.

[244] V. Sverdlov, A. Makarov, and S. Selberherr, "Reliable Sub-Nanosecond Switching of a Perpendicular SOT-MRAM Cell without External Magnetic Field," *Syst. Cybern. Informatics*, vol. 16, no. 2, pp. 55–59, 2018.

[245] L. Relm, V. Sluka, G. E. Rowlands, M.-H. Nguyen, T. A. Ohki, and A. D. Kent, "Sub-nanosecond switching in a cryogenic spin-torque spin-valve memory element with a dilute permalloy free layer," *Appl. Phys. Lett.*, vol. 114, p. 212402, 2019.

[246] W. P. Pratt, J. S. F. Lee, J. M. Slaughter, R. Loloee, P. A. Schroeder, and J. Bass, "Perpendicular Giant Magnetoresistances of Ag/Co Multilayers," *Phys. Rev. Lett.*, vol. 66, no. 23, pp. 3060–3063, 1991.

[247] J. C. Slonczewski, "Current-driven excitation of magnetic multilayers," *J. Magn. Magn. Mater.*, vol. 159, pp. L1–L7, 1996.

[248] E. B. Myers, D. C. Ralph, J. A. Katine, R. N. Louie, and R. A. Buhrman, "Current-Induced Switching of Domains in MagneticMultilayer Devices," *Science*, vol. 285, no. 5429, pp. 867–870, 1999.

[249] J. A. Katine, F. J. Albert, R. A. Buhrman, E. B. Myers, and D. C. Ralph, "Current-driven magnetization reversal and spin-wave excitations in Co/Cu/Co pillars," *Phys. Rev. Lett.*, vol. 84, no. 14, pp. 3149–3152, 2000.

[250] K. Yagami, A. A. Tulapurkar, A. Fukushima, and Y. Suzuki, "Low-current spin-transfer switching and its thermal durability in a low-saturation-magnetization nanomagnet," *Appl. Phys. Lett.*, vol. 85, no. 23, pp. 5634–5636, 2004.

[251] Z. Diao *et al.*, "Spin-transfer torque switching in magnetic tunnel junctions and spin-transfer torque random access memory," *J. Phys.: Condens. Matter*, vol. 19, p. 165209, 2007.

[252] K. Aoshima *et al.*, "Spin transfer switching in current-perpendicular-to-plane spin valve observed by magneto-optical Kerr effect using visible light," *Appl. Phys. Lett.*, vol. 91, p. 052507, 2007.

[253] K. Aoshima *et al.*, "A Magneto-Optical Spatial Light Modulator Driven by Spin Transfer Switching for 3D Holography Applications," *J. Disp. Technol.*, vol. 11, no. 2, pp. 129–135, 2015.

[254] P. Gambardella and I. M. Miron, "Current-induced spin-orbit torques," *Philos. Trans. R. Soc. A*, vol. 369, pp. 3175–3197, 2011.

[255] U. H. Pi *et al.*, "Tilting of the spin orientation induced by Rashba effect in ferromagnetic metal layer," *Appl. Phys. Lett.*, vol. 97, p. 162507, 2010.

[256] L. Meier, G. Salis, I. Shorubalko, E. Gini, S. Schön, and K. Ensslin, "Measurement of Rashba and Dresselhaus spin-orbit magnetic fields," *Nat. Phys.*, vol. 3, pp. 650–654, 2007.

[257] A. Manchon, H. C. Koo, J. Nitta, S. M. Frolov, and R. A. Duine, "New perspectives for Rashba spin-orbit coupling," *Nat. Mater.*, vol. 14, no. 9, pp. 871–882, 2015.

[258] J. E. Hirsch, "Spin Hall Effect," *Phys. Rev. Lett.*, vol. 83, no. 9, pp. 1834–1837, 1999.

[259] I. M. Miron *et al.*, "Current-driven spin torque induced by the Rashba effect in a ferromagnetic metal layer," *Nat. Mater.*, vol. 9, pp. 230–234, 2010.

[260] A. Manchon and S. Zhang, "Theory of nonequilibrium intrinsic spin torque in a single nanomagnet," *Phys. Rev. B*, vol. 78, p. 212405, 2008.

[261] K. Garello *et al.*, "Symmetry and magnitude of spin-orbit torques in ferromagnetic heterostructures," *Nat. Nanotechnol.*, vol. 8, no. 8, pp. 587–593, 2013.

[262] G. Yu *et al.*, “Switching of perpendicular magnetization by spin-orbit torques in the absence of external magnetic fields,” *Nat. Nanotechnol.*, vol. 9, no. 7, pp. 548–554, 2014.

[263] V. M. Edelstein, “Spin polarization of conduction electrons induced by electric current in two-dimensional asymmetric electron systems,” *Solid State Commun.*, vol. 73, no. 3, pp. 233–235, 1990.

[264] Y. Kato, R. C. Myers, A. C. Gossard, and D. D. Awschalom, “Coherent spin manipulation without magnetic fields in strained semiconductors,” *Nature*, vol. 427, no. 6969, pp. 50–53, 2004.

[265] A. Chernyshov, M. Overby, X. Liu, J. K. Furdyna, Y. Lyanda-Geller, and L. P. Rokhinson, “Evidence for reversible control of magnetization in a ferromagnetic material by means of spin-orbit magnetic field,” *Nat. Phys.*, vol. 5, no. 9, pp. 656–659, 2009.

[266] C. O. Avci *et al.*, “Magnetization switching of an MgO/Co/Pt layer by in-plane current injection,” *Appl. Phys. Lett.*, vol. 100, p. 212404, 2012.

[267] I. M. Miron *et al.*, “Perpendicular switching of a single ferromagnetic layer induced by in-plane current injection,” *Nature*, vol. 476, pp. 189–193, 2011.

[268] K. Garello *et al.*, “Ultrafast magnetization switching by spin-orbit torques,” *Appl. Phys. Lett.*, vol. 105, no. 21, p. 212402, 2014.

[269] M. Cubukcu *et al.*, “Spin-orbit torque magnetization switching of a three-terminal perpendicular magnetic tunnel junction,” *Appl. Phys. Lett.*, vol. 104, p. 042406, 2014.

[270] J. Cao *et al.*, “Spin-orbit torque induced magnetization switching in Ta/Co20Fe60B20/MgO structures under small in-plane magnetic fields,” *Appl. Phys. Lett.*, vol. 108, p. 172404, 2016.

[271] S. Fukami, C. Zhang, S. Duttagupta, A. Kurenkov, and H. Ohno, “Magnetization switching by spin-orbit torque in an antiferromagnet-ferromagnet bilayer system,” *Nat. Mater.*, vol. 15, no. 5, pp. 535–541, 2016.

[272] Z. A. Bekele *et al.*, “Spin-orbit torque induced magnetization switching in heavy

metal/ferromagnet multilayers with bilayer of heavy metals," *Solid State Commun.*, vol. 262, no. June, pp. 44–49, 2017.

[273] W. Y. Kwak, J. H. Kwon, P. Grünberg, S. H. Han, and B. K. Cho, "Current-induced magnetic switching with spin-orbit torque in an interlayer-coupled junction with a Ta spacer layer," *Sci. Rep.*, vol. 8, p. 3826, 2018.

[274] Y. Sheng, Y. C. Li, X. Q. Ma, and K. Y. Wang, "Current-induced four-state magnetization switching by spin-orbit torques in perpendicular ferromagnetic trilayers," *Appl. Phys. Lett.*, vol. 113, p. 112406, 2018.

[275] M. Dc *et al.*, "Room-temperature high spin–orbit torque due to quantum confinement in sputtered BixSe(1–x) films," *Nat. Mater.*, vol. 17, pp. 800–807, 2018.

[276] S. Pathak, C. Youm, and J. Hong, "Impact of Spin-Orbit Torque on Spin-Transfer Torque Switching in Magnetic Tunnel Junctions," *Sci. Rep.*, vol. 10, p. 2799, 2020.

[277] P. B. Meisenheimer, S. Novakov, N. M. Vu, and J. T. Heron, "Perspective: Magnetoelectric switching in thin film multiferroic heterostructures," *J. Appl. Phys.*, vol. 123, p. 240901, 2018.

[278] M. Weiler *et al.*, "Voltage controlled inversion of magnetic anisotropy in a ferromagnetic thin film at room temperature," *New J. Phys.*, vol. 11, p. 013021, 2009.

[279] C. G. Duan, J. P. Velev, R. F. Sabirianov, W. N. Mei, S. S. Jaswal, and E. Y. Tsymbal, "Tailoring magnetic anisotropy at the ferromagnetic/ferroelectric interface," *Appl. Phys. Lett.*, vol. 92, p. 122905, 2008.

[280] M. Y. Zhuravlev, A. V. Vedyayev, and E. Y. Tsymbal, "Interlayer exchange coupling across a ferroelectric barrier," *J. Phys.: Condens. Matter*, vol. 22, p. 352203, 2010.

[281] F. Matsukura, Y. Tokura, and H. Ohno, "Control of magnetism by electric fields," *Nat. Nanotechnol.*, vol. 10, pp. 209–220, 2015.

[282] N. A. Pertsev, "Giant magnetoelectric effect via strain-induced spin reorientation transitions in ferromagnetic films," *Phys. Rev. B*, vol. 78, p. 212102, 2008.

[283] J. M. Hu, C. W. Nan, and L. Q. Chen, "Size-dependent electric voltage controlled magnetic anisotropy in multiferroic heterostructures: Interface-charge and strain

comediated magnetoelectric coupling," *Phys. Rev. B*, vol. 83, p. 134408, 2011.

[284] D. Chien *et al.*, "Enhanced voltage-controlled magnetic anisotropy in magnetic tunnel junctions with an MgO/PZT/MgO tunnel barrier," *Appl. Phys. Lett.*, vol. 108, p. 112402, 2016.

[285] X. Li, "Voltage-Controlled Magnetic Anisotropy in Heavy Metal|Ferromagnet|Insulator-Based Structures," University of California, 2016.

[286] H. Ohno *et al.*, "Electric-fi eld control of ferromagnetism," *Nature*, vol. 408, pp. 944–946, 2000.

[287] H. Lu *et al.*, "Electric modulation of magnetization at the BaTiO3/La0.67Sr0.33MnO3 interfaces," *Appl. Phys. Lett.*, vol. 100, p. 232904, 2012.

[288] D. Chiba and T. Ono, "Control of magnetism in Co by an electric field," *J. Phys. D: Appl. Phys.*, vol. 46, p. 213001, 2013.

[289] T. Zhao *et al.*, "Electrical control of antiferromagnetic domains in multiferroic BiFeO3 films at room temperature," *Nat. Mater.*, vol. 5, no. 10, pp. 823–829, 2006.

[290] T. H. E. Lahtinen, K. J. A. Franke, and S. van Dijken, "Electric-field control of magnetic domain wall motion and local magnetization reversal," *Sci. Rep.*, vol. 2, p. 258, 2012.

[291] M. C. Onbaşlı, "Magneto-Optical and Multiferroic Oxide Thin Films, Integrated Nonreciprocal Photonic Devices and Multiferroic Memory Devices," Massachusetts Instıtute of Technology, 2015.

[292] D. B. Chrisey and G. K. Hubler, *Pulsed laser deposition of thin films*. New York, 1994.

[293] R. Menon, "Diffractive Optics for Maskless Lithography and Imaging," Massachusetts Institute of Technology, 2003.

[294] R. Menon, A. Patel, D. Gil, and H. I. Smith, "Maskless lithography," *Mater. Today*, vol. 8, no. 2, pp. 26–33, 2005.

[295] J. P. Patel and P. H. Parsania, "Characterization, testing, and reinforcing materials of biodegradable composites," in *Biodegradable and Biocompatible Polymer Composites: Processing, Properties and Applications*, Elsevier Ltd, 2018, pp. 55–79.

[296] V. Saxena, I. Shukla, and L. M. Pandey, “Hydroxyapatite: an inorganic ceramic for biomedical applications,” in *Materials for Biomedical Engineering: Nanobiomaterials in Tissue Engineering*, Elsevier Inc., 2019, pp. 205–249.

[297] D. K. Unruh and T. Z. Forbes, “X-ray Diffraction Techniques,” in *Analytical Geomicrobiology: A Handbook of Instrumental Techniques*, J. P. L. Kenney, H. Veeramani, and D. S. Alessi, Eds. Cambridge: Cambridge University Press, 2019, pp. 215–237.

[298] C. Argyropoulos, “FDTD Modelling of Electromagnetic Transformation Based Devices,” University of London, 2010.

[299] J. Olkkonen, “Finite difference time domain studies on sub-wavelength aperture structures,” 2010.

[300] K. S. Yee, “Numerical Solution of Initial Boundary Value Problems Involving Maxwell’s Equations in Isotropic Media,” *IEEE Trans. Antennas Propag.*, vol. 14, no. 3, pp. 302–307, 1966.

[301] S. Benkler, “Robust conformal subcell modeling for electromagnetic simulations in time domain,” ETH Zürich, 2007.

[302] A. C. Lesina, “Parallel FDTD Electromagnetic Simulation of Dispersive Plasmonic Nanostructures and Opal Photonic Crystals in the Optical Frequency Range,” University of Trento, 2013.

[303] W. Whittow, “Specific Absorption Rate Perturbations in the Eyes and Head by Metallic Spectacles at Personal Radio Communication Frequencies,” University of Sheffield, 2004.

[304] K. M. Wilson, “Dynamic structural colour in thin film stacks and patterned nanoparticle arrays,” Trinity College Dublin, 2018.

[305] T. Fakhrul, S. Tazlaru, L. Beran, Y. Zhang, M. Veis, and C. A. Ross, “Magneto-Optical Bi:YIG Films with High Figure of Merit for Nonreciprocal Photonics,” *Adv. Opt. Mater.*, vol. 7, p. 1900056, 2019.

[306] S. Kharratian, H. Urey, and M. C. Onbaşlı, “Advanced Materials and Device

Architectures for Magnetooptical Spatial Light Modulators," *Adv. Opt. Mater.*, vol. 8, p. 1901381, 2020.

[307] N. I. Mezin, N. Y. Starostyuk, and S. V. Yampolskii, "Growth and properties of yttrium-iron garnet films with a higher iron content," *J. Magn. Magn. Mater.*, vol. 442, pp. 189–195, 2017.

[308] V. N. Moorthy, S. Dhara, A. C. Rastogi, B. K. Das, and D. V. S. Jain, "Structure and growth of yttrium iron garnet thin films with enhanced magnetic properties by metalorganic chemical vapor deposition," *J. Mater. Res.*, vol. 14, no. 5, pp. 1865–1875, 1999.

[309] T. E. Gage, P. Dulal, P. A. Solheid, D. J. Flannigan, and B. J. H. Stadler, "Si-integrated ultrathin films of phase-pure Y3Fe5O12 (YIG) via novel two-step rapid thermal anneal," *Mater. Res. Lett.*, vol. 5, no. 6, pp. 379–385, 2017.

[310] A. W. Danish, "Study on Preparation and Characterization of Bismuth Substituted Gadolinium Iron Garnet Thin Films by Metal Organic Decomposition Method," Tokyo University of Agriculture and Technolog, 2017.

[311] O. Ciubotariu, A. Semisalova, K. Lenz, and M. Albrecht, "Strain-induced perpendicular magnetic anisotropy and Gilbert damping of Tm3Fe5O12 thin films," *Sci. Rep.*, vol. 9, p. 17474, 2019.

[312] L. Soumah *et al.*, "Ultra-low damping insulating magnetic thin films get perpendicular," *Nat. Commun.*, vol. 9, p. 3355, 2018.

[313] M.-Y. Chern and J.-S. Liaw, "Study of BixY3-xFe5O12 Thin Films Grown by Pulsed Laser Deposition," *Jpn. J. Appl. Phys.*, vol. 36, pp. 1049–1053, 1997.

[314] H. Kidoh, A. Morimoto, and T. Shimizu, "Synthesis of ferromagnetic Bi-substituted yttrium iron garnet films by laser ablation," *Appl. Phys. Lett.*, vol. 59, pp. 237–239, 1991.

[315] S. Leitenmeier, T. Körner, J. Griesbauer, M. Herbort, A. Heinrich, and B. Stritzker, "Studies on the growth of epitaxial bismuth-substituted iron garnet on gadolinium gallium garnet single crystals by pulsed laser deposition," *J. Cryst. Growth*, vol. 310,

no. 24, pp. 5392–5401, 2008.

[316] H. Hayashi *et al.*, "Characteristics of Bi:YIG magneto-optic thin films fabricated by pulsed laser deposition method for an optical current transformer," *Jpn. J. Appl. Phys.*, vol. 41, no. 1, pp. 410–411, 2002.

[317] K. H. Chung, T. Kato, S. Mito, H. Takagi, and M. Inoue, "Fabrication and characteristics of one-dimensional magnetophotonic crystals for magneto-optic spatial light phase modulators," *J. Appl. Phys.*, vol. 107, p. 09A930, 2010.

[318] T. Yoshimoto *et al.*, "Thermally stable amorphous tantalum yttrium oxide with low IR absorption for magnetophotonic devices," *Sci. Rep.*, vol. 7, p. 13805, 2017.

[319] S. P. Pavunny, R. Thomas, A. Kumar, E. Fachini, and R. S. Katiyar, "Optical properties of amorphous high-k LaGdO3 films and its band alignment with Si," *J. Appl. Phys.*, vol. 111, p. 044106, 2012.

[320] M. Ismael, E. Elhaddad, D. H. Taffa, and M. Wark, "Synthesis of phase pure hexagonal YFeO3 perovskite as efficient visible light active photocatalyst," *Catalysts*, vol. 7, no. 11, p. 326, 2017.

[321] Y. Guo, N. Zhang, H. Huang, Z. Li, and Z. Zou, "A novel wide-spectrum response hexagonal YFeO3 photoanode for solar water splitting," *RSC Adv.*, vol. 7, no. 30, pp. 18418–18420, 2017.

[322] B. Jiang *et al.*, "Spectral properties and charge transfer luminescence of Yb3+ :Gd3Ga5O12 (Yb:GGG) crystal," *J. Cryst. Growth*, vol. 277, pp. 186–191, 2005.

[323] F. T. S. Yu and X. Yang, *Introduction to Optical Engineering*. Cambridge: Cambridge University Press, 1997.

[324] Z. Yu, Z. Wang, and S. Fan, "One-way total reflection with one-dimensional magneto-optical photonic crystals," *Appl. Phys. Lett.*, vol. 90, p. 121133, 2007.

[325] Z. Wang *et al.*, "Gyrotropic response in the absence of a bias field," *Proc. Natl. Acad. Sci. U. S. A.*, vol. 109, no. 33, pp. 13194–13197, 2012.

[326] M. Moccia, G. Castaldi, V. Galdi, A. Alu, and N. Engheta, "Enhanced Faraday rotation

via resonant tunnelling in tri-layers containing magneto-optical metals," *J. Phys. D: Appl. Phys.*, vol. 47, p. 025002, 2014.

[327] K. Takada, K. Chida, and J. Noda, "Precise method for angular alignment of birefringent fibers based on an interferometric technique with a broadband source," *Appl. Opt.*, vol. 26, no. 15, pp. 2979–2987, 1987.

[328] X. Wang, M. Fujimaki, and K. Awazu, "Photonic crystal structures in titanium dioxide (TiO2) and their optimal design," *Opt. Express*, vol. 13, no. 5, pp. 1486–1497, 2005.

[329] R. S. Dubey and V. Ganesan, "Fabrication and characterization of TiO2/SiO2 based Bragg reflectors for light trapping applications," *Results Phys.*, vol. 7, pp. 2271–2276, 2017.

[330] M. Deopura, C. K. Ullal, B. Temelkuran, and Y. Fink, "Dielectric omnidirectional visible reflector," *Opt. Lett.*, vol. 26, no. 15, pp. 1197–1199, 2001.

[331] T. Goto, Y. Eto, K. Kobayashi, Y. Haga, M. Inoue, and C. A. Ross, "Vacuum annealed cerium-substituted yttrium iron garnet films on non-garnet substrates for integrated optical circuits," *J. Appl. Phys.*, vol. 113, p. 17A939, 2013.

[332] T. Goto *et al.*, "Nonreciprocal racetrack resonator based on vacuum-annealed magnetooptical cerium-substituted yttrium iron garnet," *Opt. Express*, vol. 22, no. 16, pp. 19047–19054, 2014.

[333] M. Inoue, K. Arai, T. Fujii, and M. Abe, "One-dimensional magnetophotonic crystals," *J. Appl. Phys.*, vol. 85, no. 8, pp. 5768–5770, 1999.

[334] M. C. Onbasli, T. Goto, X. Sun, N. Huynh, and C. A. Ross, "Integration of bulk-quality thin film magneto-optical cerium-doped yttrium iron garnet on silicon nitride photonic substrates," *Opt. Express*, vol. 22, no. 21, pp. 25183–25192, 2014.

[335] K. S. J. Wilson and V. Revathy, "Investigation of Photonic Band Gap in Si-Based One-Dimensional Photonic Crystal," *Opt. Photonics J.*, vol. 3, pp. 365–368, 2013.

[336] M. Zamani and M. Ghanaatshoar, "Miniaturized magnetophotonic crystals for multifunction applications in infrared region," *Opt. Eng.*, vol. 54(9), p. 097103, 2015.

[337] B. Hill, I. Sander, and G. Much, "Magneto-optic memories," *Opt. Acta (Lond).*, vol.

24, no. 4, pp. 495–504, 1977.

[338] Z. Shirakashi *et al.*, "Reconstruction of non-error magnetic hologram data by magnetic assist recording," *Sci. Rep.*, vol. 7, p. 12835, 2017.

[339] Y. Nakamura, P. B. Lim, T. Goto, H. Uchida, and M. Inoue, "Development of heat dissipation multilayer media for volumetric magnetic hologram memory," *Appl. Sci.*, vol. 9, p. 1738, 2019.

[340] G. M. Choi, A. Schleife, and D. G. Cahill, "Optical-helicity-driven magnetization dynamics in metallic ferromagnets," *Nat. Commun.*, vol. 8, p. 15085, 2017.

[341] Q. Chen, H. Wang, Q. Wang, and Y. Pan, "Plasmon Enhanced Faraday Rotation in Fe3O4/Ag Ferrofluids for Magneto Optical Sensing Applications," *Plasmonics*, vol. 13, no. 1, pp. 353–363, 2018.

[342] F. Sohrabi and S. M. Hamidi, "Fabrication methods of plasmonic and magnetoplasmonic crystals: a review," *Eur. Phys. J. Plus*, vol. 132, p. 15, 2017.

[343] B. Yu *et al.*, "Magneto-optical Studies of Noble Metal-Magnetic Dielectric Systems," *Plasmonics*, vol. 13, pp. 31–38, 2018.

[344] D. Li *et al.*, "Plasmonics Resonance Enhance Magneto-Optical Effects Through Metallic Sub-wavelength Grating with Bismuth Iron Garnet Slab," *Plasmonics*, vol. 13, pp. 55–62, 2018.

[345] X. Wan, M. Q. Qi, T. Y. Chen, and T. J. Cui, "Field-programmable beam reconfiguring based on digitally-controlled coding metasurface," *Sci. Rep.*, vol. 6, p. 20663, 2016.

[346] A. M. Shaltout, V. M. Shalaev, and M. L. Brongersma, "Spatiotemporal light control with active metasurfaces," *Science*, vol. 364, p. eaat3100, 2019.

[347] R. Won, "The rise of plasmonic metasurfaces," *Nat. Photonics*, vol. 11, pp. 462–464, 2017.

[348] J. Zhang, M. ElKabbash, R. Wei, S. C. Singh, B. Lam, and C. Guo, "Plasmonic metasurfaces with 42.3% transmission efficiency in the visible," *Light Sci. Appl.*, vol. 8, p. 53, 2019.

[349] A. De Marcellis, E. Palange, M. Janneh, C. Rizza, A. Ciattoni, and S. Mengali, "Design Optimisation of Plasmonic Metasurfaces for Mid-Infrared High-Sensitivity Chemical Sensing," *Plasmonics*, vol. 12, pp. 293–298, 2017.

[350] V. Giannini, A. I. Fernández-Domínguez, S. C. Heck, and S. A. Maier, "Plasmonic nanoantennas: Fundamentals and their use in controlling the radiative properties of nanoemitters," *Chem. Rev.*, vol. 111, pp. 3888–3912, 2011.

[351] B. Caballero, A. García-Martín, and J. C. Cuevas, "Faraday effect in hybrid magneto-plasmonic photonic crystals," *Opt. Express*, vol. 23, no. 17, pp. 22238–22249, 2015.

[352] C. Lei *et al.*, "Enhancement of magneto-optical Faraday effects and extraordinary optical transmission in a tri-layer structure with rectangular annular arrays," *Opt. Lett.*, vol. 41, no. 4, pp. 729–732, 2016.

[353] S. Sadeghi and S. M. Hamidi, "Enhanced Faraday rotation in one dimensional magneto-plasmonic structure due to Fano resonance," *J. Magn. Magn. Mater.*, vol. 451, pp. 305–310, 2018.

[354] S. Rahimzadeh Kalaleh Rodriguez, "Coupling Light and Matter in Metallic Nanoparticle Arrays," Eindhoven University of Technology, 2012.

[355] A. N. Kalish *et al.*, "Magnetoplasmonic quasicrystals: an approach for multiband magneto-optical response," *Optica*, vol. 5, no. 5, pp. 617–623, 2018.

[356] S. D. Pappas *et al.*, "Broadband enhancement of the magneto-optical activity of hybrid Au loaded Bi:YIG," *Prepr. https//arxiv.org/abs/1905.11941*, 2019.

[357] H. Gao *et al.*, "Rayleigh anomaly-surface plasmon polariton resonances in palladium and gold subwavelength hole arrays," *Opt. Express*, vol. 17, no. 4, pp. 2334–2340, 2009.

[358] G. Wiederrecht, *Handbook of Nanoscale Optics and Electronics*, First. Amsterdam, 2010.

[359] S. A. Safiabadi Tali and W. Zhou, "Multiresonant plasmonics with spatial mode overlap: Overview and outlook," *Nanophotonics*, vol. 8, no. 7, pp. 1199–1225, 2019.

[360] S. Murai, M. A. Verschuuren, G. Lozano, G. Pirruccio, S. R. K. Rodriguez, and J.

Gómez Rivas, "Hybrid plasmonic-photonic modes in diffractive arrays of nanoparticles coupled to light-emitting optical waveguides," *Opt. Express*, vol. 21, no. 4, pp. 4250–4262, 2013.

[361] P. B. Johnson and R. W. Christy, "Optical Constant of the Nobel Metals," *Phys. Rev. B*, vol. 6, no. 12, pp. 4370–4379, 1972.

[362] E. D. Palik, *Handbook of Optical Constants of Solids*. Orlando: Academic Press, 1985.

[363] V. I. Belotelov, L. L. Doskolovich, V. A. Kotov, E. A. Bezus, D. A. Bykov, and A. K. Zvezdin, "Magnetooptical effects in the metal-dielectric gratings," *Opt. Commun.*, vol. 278, pp. 104–109, 2007.

[364] V. I. Belotelov, L. L. Doskolovich, and A. K. Zvezdin, "Extraordinary magneto-optical effects and transmission through metal-dielectric plasmonic systems," *Phys. Rev. Lett.*, vol. 98, p. 077401, 2007.

[365] V. Dmitriev, F. Paixão, and M. Kawakatsu, "Enhancement of Faraday and Kerr rotations in three-layer heterostructure with extraordinary optical transmission effect," *Opt. Lett.*, vol. 38, no. 7, p. 1052, 2013.

[366] S. M. Drezdzon and T. Yoshie, "On-chip waveguide isolator based on bismuth iron garnet operating via nonreciprocal single-mode cutoff.," *Opt. Express*, vol. 17, no. 11, pp. 9276–9281, 2009.

[367] M.-G. Kang, V. Dong Quoc, S. Surabhi, B.-G. Park, and J.-R. Jeong, "Spectrometer based real-time magnetic Faraday rotation spectroscopy of Bi-YIG thin films," *J. Magn. Magn. Mater.*, vol. 482, pp. 61–65, 2019.

[368] E. J. Zeman and G. C. Schatz, "An accurate electromagnetic theory study of surface enhancement factors for Ag, Au, Cu, Li, Na, Al, Ga, In, Zn, and Cd," *J. Phys. Chem.*, vol. 91, no. 3, pp. 634–643, 1987.

[369] D. A. Bandurin *et al.*, "Resonant terahertz detection using graphene plasmons," *Nat. Commun.*, vol. 9, p. 5392, 2018.

[370] J. P. B. Mueller, N. A. Rubin, R. C. Devlin, B. Groever, and F. Capasso, "Metasurface Polarization Optics: Independent Phase Control of Arbitrary Orthogonal States of

Polarization," *Phys. Rev. Lett.*, vol. 118, p. 113901, 2017.

[371] M. del P. Rodríguez-Torres, L. A. Díaz-Torres, and S. Romero-Servin, "Heparin assisted photochemical synthesis of gold nanoparticles and their performance as SERS substrates," *Int. J. Mol. Sci.*, vol. 15, no. 10, pp. 19239–19252, 2014.

[372] E. D. B. Santos, E. C. N. L. Lima, C. S. De Oliveira, F. A. Sigoli, and I. O. Mazali, "Fast detection of paracetamol on a gold nanoparticle-chitosan substrate by SERS," *Anal. Methods*, vol. 6, no. 11, pp. 3564–3568, 2014.

[373] G. Laurent *et al.*, "Evidence of multipolar excitations in surface enhanced Raman scattering," *Phys. Rev. B*, vol. 71, p. 045430, 2005.

[374] M. Nur-E-Alam, M. Vasiliev, and K. Alameh, "Nano-structured magnetic photonic crystals for magneto-optic polarization controllers at the communication-band wavelengths," *Opt. Quant. Electron*, vol. 41, no. 9, pp. 661–669, 2009.